

# Abstract

PUNUGUPATI, SANDHYARANI. Fabrication and Properties of  $\text{Cr}_2\text{O}_3$  and  $\text{La}_{0.7}\text{Sr}_{0.3}\text{MnO}_3$  Thin Film Heterostructures Integrated on Si(001). (Under the guidance of Prof. Jagdish Narayan and Prof. Frank Hunte.)

Spintronics that utilizes both the spin and charge degrees of freedom of an electron is emerged as an alternate memory technology to conventional CMOS electronics. Many proposed spintronic devices require multifunctional properties in a single material. The oxides  $\text{Cr}_2\text{O}_3$  and  $\text{La}_{0.7}\text{Sr}_{0.3}\text{MnO}_3$  are such materials which exhibit unique physical properties at room temperature. The  $\text{Cr}_2\text{O}_3$  is an antiferromagnetic and magnetoelectric material below its Néel temperature 307K. The  $\text{La}_{0.7}\text{Sr}_{0.3}\text{MnO}_3$  is a ferromagnetic half metal with a Curie temperature of 360K and exhibits colossal magnetoresistance. However, the reach of this spintronic technology into more device applications is possible only when these materials in epitaxial thin film form are integrated with Si(001) which is the mainstay substrate in semiconductor industry.

The primary objective of this dissertation was to integrate epitaxial  $\text{Cr}_2\text{O}_3$ ,  $\text{La}_{0.7}\text{Sr}_{0.3}\text{MnO}_3$  and  $\text{Cr}_2\text{O}_3/\text{La}_{0.7}\text{Sr}_{0.3}\text{MnO}_3$  thin film heterostructure on Si(001) and, study their physical properties to investigate structure-processing-property relationship in these heterostructures.

The epitaxial integration of  $\text{Cr}_2\text{O}_3$  thin films on Si(001) was done using epitaxial cubic yttria stabilized zirconia (c-YSZ) buffer layer by pulsed laser deposition. Detailed structural characterizations XRD ( $2\theta$  and  $\Phi$ ) and TEM confirm the epitaxial nature of the films. Though bulk  $\text{Cr}_2\text{O}_3$  is antiferromagnetic along the c-axis, the in-plane magnetization measurements on  $\text{Cr}_2\text{O}_3(0001)$  thin films showed ferromagnetic behavior up to 400K. The

thickness dependent magnetization together with oxygen annealing results suggested that the in-plane ferromagnetism in  $\text{Cr}_2\text{O}_3$  was due to the oxygen related defects whose concentration is controlled by strain in the films. The out-of-plane magnetic measurements on  $\text{Cr}_2\text{O}_3(0001)$  films showed magnetic behavior indicative of antiferromagnetic nature.

To verify whether ferromagnetism can be induced by strain in  $\text{Cr}_2\text{O}_3$  thin films with orientation other than (0001), epitaxial thin films were prepared on r- $\text{Al}_2\text{O}_3$  substrate and their magnetic properties were studied. The XRD ( $2\theta$  and  $\Phi$ ) and TEM confirm that the films were grown epitaxially. The epitaxial relations were given as:  $[01\bar{1}2]\text{Cr}_2\text{O}_3 \parallel [01\bar{1}2]\text{Al}_2\text{O}_3$  and  $[\bar{1}\bar{1}20]\text{Cr}_2\text{O}_3 \parallel [\bar{1}\bar{1}20]\text{Al}_2\text{O}_3$ . The as-deposited films showed ferromagnetic behavior up to 400K but it almost vanished with oxygen annealing. The Raman spectroscopy data together with strain measurements using XRD indicated that ferromagnetism in r- $\text{Cr}_2\text{O}_3$  thin films was due to the strain caused by defects such as oxygen vacancies.

Bi-epitaxial  $\text{La}_{0.7}\text{Sr}_{0.3}\text{MnO}_3(110)$  thin films were integrated on Si(100) with c-YSZ/ $\text{SrTiO}_3(\text{STO})$  buffer layers by pulsed laser deposition. The  $\text{La}_{0.7}\text{Sr}_{0.3}\text{MnO}_3$  and STO thin films had a single [110] out-of-plane orientation but with two in-plane domain variants as confirmed from XRD and TEM study. The growth of STO on c-YSZ was explained by the domain matching epitaxy paradigm. The epitaxial relationship between STO and c-YSZ were written as  $[110](001)\text{c-YSZ} \parallel [\bar{1}\bar{1}\bar{1}](110)\text{STO}$  (or)  $[110](001)\text{c-YSZ} \parallel [\bar{1}\bar{1}\bar{2}](110)\text{STO}$ . The  $\text{La}_{0.7}\text{Sr}_{0.3}\text{MnO}_3$  thin films were ferromagnetic with Curie temperature 324K. They also exhibited hysteresis in magnetoresistance under both in-plane and out-of-plane magnetic fields. The highest magnetoresistance in this study was -32% at 50K and 50 kOe for in-plane configuration.

Lastly, the epitaxial  $\text{La}_{0.7}\text{Sr}_{0.3}\text{MnO}_{3-\delta}$ (LSMO)/ $\text{Cr}_2\text{O}_3$  bilayer structure was integrated with Si(001) using c-YSZ by pulsed laser deposition. The XRD ( $2\theta$  and  $\Phi$ ) and TEM characterizations confirm that the films were grown epitaxially. The epitaxial relations were written as  $[0001]\text{Cr}_2\text{O}_3 \parallel [111]\text{LSMO}$  and  $[11\bar{2}0]\text{Cr}_2\text{O}_3 \parallel [10\bar{1}]\text{LSMO}$ . Interestingly, when the LSMO thickness was increased from 66 to 528 nm ( $\text{Cr}_2\text{O}_3=55\text{nm}$ ), the magnetization increased by 2-fold and the magnetic nature changed from ferromagnetic to super paramagnetic. In addition, LSMO/ $\text{Cr}_2\text{O}_3$  showed in-plane exchange bias. We believe that the change in the magnetic anisotropy as a function of LSMO layer thickness could cause the change in magnetization and magnetic nature. The magnetic phase separation in oxygen deficient LSMO layer could lead to in-plane exchange bias as  $\text{Cr}_2\text{O}_3$  is not expected to show in-plane exchange.

© Copyright 2015 Sandhyarani Punugupati

All Rights Reserved

Fabrication and Properties of  $\text{Cr}_2\text{O}_3$  and  $\text{La}_{0.7}\text{Sr}_{0.3}\text{MnO}_3$  Thin Film Heterostructures  
Integrated on Si(001)

by  
Sandhyarani Punugupati

A dissertation submitted to the Graduate Faculty of  
North Carolina State University  
in partial fulfillment of the  
requirements for the Degree of  
Doctor of Philosophy

Materials Science and Engineering

Raleigh, North Carolina

Nov 2015

APPROVED BY:

---

Prof. Jagdish Narayan  
Co-Chair

---

Prof. Frank Hunte  
Co-Chair

---

Prof. John T. Prater

---

Prof. Daniel Dougherty

## **DEDICATION**

*To my Parents*

*To my husband Ajay*

*To my little Akshara*

## BIOGRAPHY

Sandhyarani Punugupati was born in Veerannapalem, a village in the state of Andhra Pradesh in southern India. She completed her schooling from S.N.B.G.B.P.H. School in her village and later studied up to 12<sup>th</sup> grade in J.M.J. College, Tenali. While doing her Bachelors in Physics and Mathematics from Govt. College for Women in Guntur, she developed a passion towards Physics and got admission into M.Sc. Physics in Andhra University, Visakhapatnam in 2003. Though she had interest towards research and higher education, after completion of her Masters, she had to work for two-and-half-years as a lecturer teaching Physics in T.S.R. & T.B.K. College, Visakhapatnam. Being a person with natural instinct of teaching, she enjoyed her profession and became a favorite lecturer for many of her students. Her fascination for higher studies in Physics *materialized* when she joined the prestigious Indian Institute of Technology, Kanpur, for M.Tech. in Materials Science Programme. Here, she worked under the guidance of Prof. Kamal K Kar for her thesis. After her marriage to Ajay in summer 2011 in India, she joined North Carolina State University in Fall 2011 to pursue her PhD in Materials Science and Engineering. In Oct 2014, the couple was blessed with a baby girl, Akshara.

## ACKNOWLEDGEMENTS

Several people have helped me during the course of my PhD and I am indebted to every one of them. First and foremost, I wish to express sincere gratitude to my advisor Prof. Jagdish (Jay) Narayan for his guidance, motivating words, and kind support. He allowed me enormous freedom in carrying out this work and his generosity and patience allowed me to make mistakes from which I have learned a lot. His discipline and commitment towards research are always inspiring. I am also very grateful to my co-advisor Prof. Frank Hunte for his research guidance and encouragement. His suggestions were of immense help during the course of this research. His expertise in magnetism contributed a lot to this dissertation.

I am extremely thankful to Prof. John Prater for his scientific discussions and invaluable suggestions for my research. I also would like to thank Prof. Daniel Dougherty for serving on my committee and also for collaborative work. I also thank Prof. Lew Reynolds for providing critical comments.

I am thankful to my teachers Prof. M.L.P. Rao and Prof. K.H.R for encouraging me to pursue higher studies.

Thanks to friendly colleagues Yvonne, Raj Kumar, Namik, Pranav, Christer Akouala, Gabrielle, Anagh, Adele, Zhengh, Adedapo, Sumeet, Golsa and Ali for sharing their experiences. Special thanks to our post-docs Dr. Sudhakar Nori and Dr. Srinivasa Rao Singamaneni for their technical discussions and personal advices.

I am very thankful to Raj Kumar for stimulating scientific discussions and help with transport measurements. I hope we can collaborate again in the future to finish years of research we

have planned☺. I also thank Namik for his patience to listen to me, and also for his help on numerous occasions in troubleshooting lab equipment. I wish him good luck for the future.

I need to acknowledge Yvonne for being a special friend to share my technical and non-technical worries and what not! Her suggestions regarding time management during my difficult times were very helpful. I am sure she will succeed in every endeavor she pursues.

Special thanks to Ms. Edna Deas for help with all administrative work. Thanks to Toby Tung for help regarding computer-related problems and software installations.

I should mention my friends Arun, Bharathi-Srinivas and their son Siddhu, Prasen, Boopathy-Viji, Samir-Swasthika, Jayasri-Kasu, Sushi-Lucky, Saranya-Pandian, for their friendship and making my stay in Raleigh a wonderful one.

I owe my success to my parents Venkateswarlu-Venkataratnam for their unconditional love, sacrifice, and support. My father has been a great inspiration to me and no words can thank him enough for teaching me values and positive attitude. My mother has been a great support, especially in the final year of my PhD. My heartfelt thanks to her for being here in Raleigh, allowing me to focus on my studies without having to worry too much about my baby and other household stuff. I also thank my brother Satish for his help.

I should mention my stress reliever for lifetime, my little one-year-angel Akshara, who made my life happier than ever. Finally, I thank my kanna Ajay for his motivation, love, care, and support in every situation and also for giving me the freedom and being there with me throughout this process. I feel proud to have such a wonderful husband.

I acknowledge National Science Foundation and Army research office for providing the necessary funding to carry out my research work.

# TABLE OF CONTENTS

LIST OF FIGURES .....	viii
LIST OF TABLES .....	xiii
<b>Chapter 1 Introduction</b> .....	<b>1</b>
<b>1.1 Spintronics</b> .....	<b>1</b>
<b>1.2 Magnetoelectric Effect and Cr<sub>2</sub>O<sub>3</sub></b> .....	<b>1</b>
<b>1.3 Exchange Bias Effect</b> .....	<b>7</b>
<b>1.4 Magnetoresistance</b> .....	<b>9</b>
<b>1.4.1 Giant Magnetoresistance</b> .....	<b>9</b>
<b>1.4.2 Tunneling Magnetoresistance</b> .....	<b>11</b>
<b>1.5 La<sub>1-x</sub>Sr<sub>x</sub>MnO<sub>3</sub></b> .....	<b>13</b>
<b>1.6 Thin Film Epitaxy</b> .....	<b>18</b>
<b>1.6.1 Lattice Matching Epitaxy</b> .....	<b>18</b>
<b>1.6.1 Domain Matching Epitaxy</b> .....	<b>19</b>
<b>1.9 References</b> .....	<b>21</b>
<b>Chapter 2 Experimental Methods</b> .....	<b>25</b>
<b>2.1 Pulsed Laser Deposition</b> .....	<b>25</b>
<b>2.2 X-ray Diffraction</b> .....	<b>27</b>
<b>2.3 Transmission Electron Microscopy</b> .....	<b>29</b>
<b>2.4 Magnetic Measurements</b> .....	<b>30</b>
<b>2.5 Transport and Magneto-transport Measurements</b> .....	<b>31</b>
<b>2.5 References</b> .....	<b>33</b>
<b>Chapter 3 Strain induced ferromagnetism in epitaxial Cr<sub>2</sub>O<sub>3</sub> thin films integrated on Si(001)</b> .....	<b>34</b>
<b>3.1 Abstract:</b> .....	<b>34</b>
<b>3.2 Introduction:</b> .....	<b>35</b>
<b>3.3 Experimental Details:</b> .....	<b>36</b>
<b>3.4 Results and Discussion:</b> .....	<b>37</b>
<b>3.5 Conclusions:</b> .....	<b>48</b>
<b>3.6 References:</b> .....	<b>49</b>

<b>Chapter 4 Room temperature ferromagnetism in epitaxial Cr<sub>2</sub>O<sub>3</sub> thin films grown on r-sapphire</b> .....	52
<b>4.1 Abstract:</b> .....	52
<b>4.2 Introduction:</b> .....	52
<b>4.3 Experimental Details:</b> .....	54
<b>4.4 Results and Discussion:</b> .....	55
<b>4.5 Conclusions:</b> .....	62
<b>4.6 References:</b> .....	64
<b>Chapter 5 Growth, magnetic and magnetotransport properties of bi-epitaxial La<sub>0.7</sub>Sr<sub>0.3</sub>MnO<sub>3</sub>(110) thin films integrated on Si(001)</b> .....	67
<b>5.1 Abstract:</b> .....	67
<b>5.2 Introduction:</b> .....	68
<b>5.3 Experimental Details:</b> .....	70
<b>5.4 Results and Discussion:</b> .....	71
<b>5.5 Conclusions:</b> .....	86
<b>5.6 References:</b> .....	88
<b>Chapter 6 Interface magnetism in epitaxial La<sub>0.7</sub>Sr<sub>0.3</sub>MnO<sub>3-δ</sub>/Cr<sub>2</sub>O<sub>3</sub> heterostructures integrated on Si (100)</b> .....	92
<b>6.1 Abstract:</b> .....	92
<b>6.2 Introduction:</b> .....	93
<b>6.3 Experimental Details:</b> .....	95
<b>6.4 Results and Discussion:</b> .....	96
<b>6.5 Conclusions:</b> .....	107
<b>6.6 References:</b> .....	109
<b>Chapter 7 Summary and Out look</b> .....	112
<b>7.1 Summary</b> .....	112
<b>7.2 Outlook</b> .....	116

## LIST OF FIGURES

Figure 1.1: The Cr <sub>2</sub> O <sub>3</sub> lattice with rhombohedral unit cell showing the spin direction of Cr <sup>3+</sup> ions in the two antiferromagnetic domains <sup>6</sup> .....	3
Figure 1.2: (a) The electric polarization along the z-direction with magnetic field parallel to z-direction. (b) Magnetic susceptibility variation with temperature <sup>15</sup> .....	5
Figure 1.3: Temperature variation of electric polarization measured at various magnetic fields applied parallel to c-axis <sup>21</sup> .....	6
Figure 1.4: Temperature variation of magnetization measured at various electric fields applied along c-axis <sup>21</sup> .....	7
Figure 1.5: Schematic diagram showing the spin configuration of an FM-AFM bilayer at different stages of an exchange biased hysteresis loop <sup>27</sup> .....	9
Figure 1.6: Magnetoresistance of three Cr/Fe multilayers measured at 4.2 K, in the CIP configuration <sup>28</sup> .....	10
Figure 1.7: TMR effect at room temperature in CoFe/Al <sub>2</sub> O <sub>3</sub> /Co junctions. Arrows indicate the relative orientation of ferromagnetic electrodes <sup>30</sup> .....	12
Figure 1.8: The schematic of the perovskite unit cell of ABO <sub>3</sub> . Yellow: La and/or Sr; Black: Mn; White: O.....	13
Figure 1.9: Five d orbitals of Mn in LaMnO <sub>3</sub> . In the cubic crystal field, this fivefold degeneracy is lifted into two e <sub>g</sub> orbitals ((x <sup>2</sup> - y <sup>2</sup> ) and (3z <sup>2</sup> - r <sup>2</sup> )) and three t <sub>2g</sub> orbitals ((xy), (yz) and (zx)) <sup>41</sup> .....	14
Figure 1.10: Crystal field splitting of the 3d orbitals of Mn <sup>3+</sup> and further degeneracy removal of the e <sub>g</sub> orbital due to Jahn–Teller distortion <sup>43</sup> .....	16
Figure 1.11: Schematic of the double exchange mechanism between Mn <sup>3+</sup> and Mn <sup>4+</sup> ions proposed by Zener <sup>44</sup> .....	17
Figure 1.12: Schematic representation of domain matching epitaxy (DME), in which three lattice planes of film match with four lattice planes of substrate. ....	20
Figure 2.1: Schematic diagram showing the pulsed laser deposition assembly. ....	26

Figure 2.2: Schematic representation of XRD $\theta$ - $2\theta$ scan configuration. ....	28
Figure 2.3: Schematic representation of the Philips X'Pert diffractometer used for $\phi$ -scans. IBO: Incident beam optics, DBO: diffracted beam optics.....	29
Figure 2.4: Schematics of the magnetoresistance measurements. (a) In-plane magnetoresistance. (b) Out-of-plane Magnetoresistance.....	32
Figure 3.1: Typical XRD $\theta$ - $2\theta$ pattern of $\text{Cr}_2\text{O}_3/\text{YSZ}/\text{Si}(001)$ heterostructure. Inset: $\omega$ -scan excited on (0006) peak of $\text{Cr}_2\text{O}_3$ .....	38
Figure 3.2: (a) Typical XRD $\phi$ scan of $\text{Cr}_2\text{O}_3/\text{YSZ}/\text{Si}(001)$ heterostructure. It was excited on (1014), (111) and (111) reflections of $\text{Cr}_2\text{O}_3$ , YSZ, and Si, respectively. (b) Schematic arrangement of the alignment of four different in-plane domain variants of $\text{Cr}_2\text{O}_3$ with YSZ unit cell planes across $\text{Cr}_2\text{O}_3/\text{YSZ}$ interface. ....	39
Figure 3.3: (a) Low magnification cross-sectional TEM image of $\text{Cr}_2\text{O}_3/\text{YSZ}/\text{Si}(001)$ heterostructure. (b) HRTEM image of $\text{Cr}_2\text{O}_3/\text{YSZ}$ interface. Inset of (a) shows the [110] zone axis SAED pattern acquired across the Si/YSZ interface.....	40
Figure 3.4: The SAED pattern acquired on $\text{Cr}_2\text{O}_3$ thin film showing two patterns along $\langle 7250 \rangle$ and $\langle 5270 \rangle$ zone axes corresponding to two domains of $\text{Cr}_2\text{O}_3$ .....	41
Figure 3.5: XPS survey spectrum of $\text{Cr}_2\text{O}_3$ thin film, showing peaks corresponding to chromium, oxygen and some atmospheric carbon.....	42
Figure 3.6: (a) Isothermal field dependent magnetization plots of 40 nm thick $\text{Cr}_2\text{O}_3$ film ranging from 5K to 400K. Lower inset: Enlarged view of the same in the -500 Oe to +500 Oe field range. Upper inset: Plot of $H_C$ vs $T^{1/2}$ showing linear fit in the range 5K to 300K. (b) M-H loops acquired at 5K for $\text{Cr}_2\text{O}_3$ films with thickness ranging from 20 to 160 nm. Inset shows the enlarged version of the same. (c) Thickness dependent saturation magnetization $M_S$ and out-of-plane strain $\epsilon_{zz}$ measured from XRD $2\theta$ scans (d) M-H loops for 40 nm thick $\text{Cr}_2\text{O}_3$ acquired at 5K for pristine and oxygen annealed samples. For all the magnetic measurements field was applied parallel to the (0001) surface of $\text{Cr}_2\text{O}_3$ . ....	43
Figure 3.7: The magnetization versus temperature data measured on a 40nm thick $\text{Cr}_2\text{O}_3$ film. The sample was cooled from 400K to 5K under an applied field of 2000 Oe and the data was collected during warming cycle with the same field. ....	44

Figure 3.8: The XRD data collected around  $\text{Cr}_2\text{O}_3(0006)$  peak on a 40 nm thick  $\text{Cr}_2\text{O}_3$  film before and after oxygen annealing. The out-of-plane strain decreased from -0.55 % to -0.50% with oxygen annealing. .... 46

Figure 3.9: Isothermal field dependent magnetization plots of 40 nm thick  $\text{Cr}_2\text{O}_3$  film at temperatures 5K, 50K and 300K as denoted. The magnetic field was applied along the out-of-plane [0001] direction, which is the easy axis for antiferromagnetic  $\text{Cr}_2\text{O}_3$ . .... 47

Figure 4.1: XRD (a)  $\theta$ -2 $\theta$  scan, (b)  $\omega$  scan of  $\text{Cr}_2\text{O}_3/\text{Al}_2\text{O}_3$  heterostructure when  $\text{Cr}_2\text{O}_3$  was grown at 650°C substrate temperature and  $5 \times 10^{-2}$  Torr oxygen partial pressure. .... 56

Figure 4.2: The  $\phi$ -scans of  $\text{Cr}_2\text{O}_3/\text{Al}_2\text{O}_3$  heterostructure excited on the (006) plane of the film and substrate, which is inclined at  $57.61^\circ$  from (0112). .... 57

Figure 4.3: (a) Indexed [2201] SAED pattern acquired across  $\text{Cr}_2\text{O}_3/\text{Al}_2\text{O}_3$  thin film heterostructure. Inset: low magnification image of the same. (b) HRTEM image of the heterostructure showing clean and sharp interface. .... 58

Figure 4.4: (a) Isothermal magnetic field dependent magnetization loops of 230 nm thick  $\text{Cr}_2\text{O}_3$  film measured at 5K, 300K and 400K. (b) Enlarged view of the same. (c) Saturation magnetization variation with temperature. (d) M vs H loops measured at 300K for the pristine and oxygen annealed samples. The magnetic field is applied in the r-plane of  $\text{Cr}_2\text{O}_3$ . .... 59

Figure 4.5: (a) Raman spectra collected on the pristine and oxygen annealed sample. Inset: Enlarged view of  $A_{1g}$  peak. (b) High resolution XRD 2 $\theta$  scan acquired on the (012) peak of pristine and oxygen annealed sample. .... 60

Figure 5.1: XRD 2 $\theta$  scan of LSMO/STO/YSZ heterostructure grown on Si (001) substrate. 72

Figure 5.2: TEM study of the Si/YSZ/STO/LSMO heterostructure showing (a) low magnification image, (b) SAED pattern near the YSZ/STO interface taken along [110] zone axis of YSZ. .... 74

Figure 5.3: (a) HAADF STEM-Z image acquired at the YSZ/STO interface along the [110] zone of YSZ (or) [111] zone of STO and (b) High resolution TEM image of the YSZ/STO interface along [110] zone of YSZ (or) [112] zone of STO. We can see the domain matching of the planes across the interface indicated by dotted lines. .... 76

Figure 5.4: (a) HAADF STEM-Z image acquired at the STO/LSMO interface [111] zone of STO and (b) High resolution TEM image of the STO/LSMO interface along [112] zone of STO. We can see the growth of LSMO on STO via lattice matching epitaxy. .... 77

Figure 5.5: Resistivity versus temperature measurement of LSMO thin film acquired from 4K to 300K in the absence of magnetic field..... 78

Figure 5.6: Magnetic field dependent magnetization data of the LSMO (110) thin film with field applied (a) in-plane denoted as  $H_{\parallel}$  (b) out-of-plane denoted as  $H_{\perp}$ . Temperature dependent magnetization data of the LSMO thin film with field applied (c) in-plane denoted as  $H_{\parallel}$  (d) out-of-plane denoted as  $H_{\perp}$ . The insets of (a) and (b) shows the enlarged view of the same showing coercivities. .... 79

Figure 5.7: Magnetic field dependent magnetization and magnetoresistance of LSMO (110) thin film measured at 10K with field applied (a) in-plane denoted as  $H_{\parallel}$  (b) out-of-plane denoted as  $H_{\perp}$ . .... 80

Figure 5.8: The magnetoresistance variation with magnetic field up to 1 kOe measured at 10K in  $H_{\parallel}$  configuration. The solid line represent the fit to the data using the equation  $MR = a_1 + a_2H + a_3H^2$ ..... 81

Figure 5.9: Isothermal magnetic field dependent magnetoresistance in the field range 0 - 50 kOe for (a) in-plane denoted as  $H_{\parallel}$  (d) out-of-plane denoted as  $H_{\perp}$ . .... 83

Figure 5.10: The magnetic field dependent magnetoresistance variation in the field range 4 - 50 kOe at 10K for (a)  $H_{\parallel}$  and (b)  $H_{\perp}$  configurations. The solid lines represent the typical fit to the data using equation  $MR = -\alpha(T)H^n$ . .... 84

Figure 5.11: The temperature dependent magnetoresistance measured at 10 and 50 kOe for both  $H_{\parallel}$  and  $H_{\perp}$  configurations..... 85

Figure 6.1: XRD  $\theta-2\theta$  pattern acquired on the LSMO/Cr<sub>2</sub>O<sub>3</sub>/c-YSZ/Si(001) heterostructure showing the effect of O<sub>2</sub> partial pressure during LSMO growth. .... 97

Figure 6.2. (a) XRD  $\phi$  scan of LSMO/Cr<sub>2</sub>O<sub>3</sub>/YSZ/Si(001) heterostructure. It was collected from (101), (1014), (111) and (111) reflections of LSMO, Cr<sub>2</sub>O<sub>3</sub>, YSZ, and Si, respectively. (b) Schematic arrangement of the growth of LSMO(111) plane on Cr<sub>2</sub>O<sub>3</sub>(0001) plane..... 98

Figure 6.3: (a) low magnification cross-sectional TEM image of the LSMO/Cr<sub>2</sub>O<sub>3</sub>/c-YSZ/Si(001) heterostructure. (b) c-YSZ/Cr<sub>2</sub>O<sub>3</sub> interface. (c) Cr<sub>2</sub>O<sub>3</sub>/LSMO interface. .... 99

Figure 6.4: The isothermal magnetization (M-H) (a) and temperature dependent variation in magnetization (M-T) (b) of all three heterostructures, namely, LSMO (66 nm)/Cr<sub>2</sub>O<sub>3</sub> (55nm); LSMO (264 nm)/Cr<sub>2</sub>O<sub>3</sub> (55nm); LSMO (528 nm)/Cr<sub>2</sub>O<sub>3</sub> (55nm). As the LSMO thickness decreases and by keeping the Cr<sub>2</sub>O<sub>3</sub> layer thickness at 55nm, the magnetization increases. The temperature at which the ZFC and FC curves split is the ‘blocking temperature’ (T<sub>b</sub>). 100

Figure 6.5: Temperature variation of resistivity of LSMO film of 66, 528 nm thicknesses as indicated. The metal to insulator transition in both the films is much reduced compared to bulk value..... 102

Figure 6.6: In-plane (a) and out of plan (b) M-H behavior of LSMO (66nm)/Cr<sub>2</sub>O<sub>3</sub> (55nm) collected at 4K under ZFC and 500 Oe FC conditions; The (c) and (d) shows the enlarged views of (a) and (b) respectively. Significant exchange bias is observed when the magnetic field is applied in-plane of the film, in comparison with that of out of plane. .... 103

Figure 6.7: In-plane M-H behavior of LSMO (66nm)/STO(50 nm)/Cr<sub>2</sub>O<sub>3</sub> (55nm) collected at 4K under ZFC and 500 Oe FC conditions as denoted. .... 104

Figure 6.8: Comparison of all three M-H curves, Cr<sub>2</sub>O<sub>3</sub>(55nm), LSMO(66nm) on STO(50nm)/Cr<sub>2</sub>O<sub>3</sub>(55nm), and LSMO(66nm) on Cr<sub>2</sub>O<sub>3</sub>(55nm). The magnetization is suppressed when a 50nm thin non-magnetic insulating STO layer is inserted between LSMO(66nm) and Cr<sub>2</sub>O<sub>3</sub>(55nm) layers. This clearly shows the role of magnetic exchange interaction at the interface between LSMO(66nm) and Cr<sub>2</sub>O<sub>3</sub>(55nm) layers..... 106

Figure 6.9: The temperature dependences of exchange bias (H<sub>EB</sub>) and coercive field (H<sub>c</sub>) for LSMO(66nm)/Cr<sub>2</sub>O<sub>3</sub>(55nm). The points show the experimental data and the solid curve guides the eye. The fact that the temperature dependence of H<sub>EB</sub> and H<sub>c</sub> shows similar nature, which is an exponential decay, their origin is mostly likely the same, which is the magnetic phase separation in LSMO layer..... 107

## LIST OF TABLES

Table 5.1 Various fit parameters  $n$ ,  $\alpha$  and the goodness parameter,  $R^2$  for the best fits of the data using the equation  $MR = -\alpha(T)H^n$  for both (in-plane,  $H_{\parallel}$ ) and (out-of-plane,  $H_{\perp}$ ) configurations at various temperatures in the field range 2-50 kOe. .... 86

# Chapter 1 Introduction

## 1.1 Spintronics

Spintronics is an acronym for spin based electronics, which is a new field that utilizes both charge and spin degree of freedom of an electron whereas in traditional electronics only electron charge is manipulated to achieve desired functionality. In conventional CMOS technology, the device features are getting decreased day by day but there is going to be a limit where further reduction cannot be done. In these circumstances, alternate technologies are required for the increasing demands of the world wide information technology needs and spintronics is one such approach. It aims at reduced power consumption, high integration density and enhanced functionality compared to present CMOS electronics. The new technologies utilizing spintronic device concepts are read heads of magnetic hard disk drives, spin valves, spin transistors, sensors and MRAM devices. The underlying material property in read heads is magnetoresistance, for which Nobel Prize in Physics was given in 2007. However, for enhancing the reach of this spintronic technology into more device applications, development of multifunctional materials in thin film form integrated on Si substrate, is needed.

## 1.2 Magnetoelectric Effect and $\text{Cr}_2\text{O}_3$

The magnetoelectric effect is a phenomenon in which electric polarization can be induced by applied magnetic fields and magnetization can be induced by applied electric fields. This effect can be linear or non-linear. The linear magnetoelectric response of a material can be expressed using  $P_i(H_j)$  or  $M_i(E_j)$ .

$$P_i = \alpha_{ij}H_j \text{ and } \mu_o M_i = \alpha_{ji}E_j \dots\dots\dots(1.1)^1$$

Where,  $P_i$  is the electronic polarization induced by magnetic field and  $M_i$  is the magnetization induced by electric field. The proportionality constant  $\alpha_{ij}$  is called magnetic tensor and its value is determined by the structure and magnetic symmetry of the material. Hence, the linear ME effect is allowed only in materials in which both space-inversion and time-reversal symmetries are broken. The majority of research on the ME effect was devoted to the linear ME effect. Dzyaloshinskii <sup>2</sup> was the first one to predict that  $\text{Cr}_2\text{O}_3$  show violation of time-reversal symmetry and soon after that pioneering experimental confirmation of an electric-field-induced magnetization <sup>3</sup> and a magnetic field-induced polarization <sup>4, 5</sup> in  $\text{Cr}_2\text{O}_3$ , both linear in the applied field was provided. The ME effect in  $\text{Cr}_2\text{O}_3$  was found to be  $\alpha_{zz} = 4.13 \text{ psm}^{-1}$ .

The sesqui oxide  $\text{Cr}_2\text{O}_3$ , also called as chromia, crystallizes in the corundum structure with  $R\bar{3}c$  space group isomorphous to  $\alpha\text{-Al}_2\text{O}_3$ . It is a Heisenberg antiferromagnet with a Néel temperature of  $T_N = 308 \text{ K}$  and is also a linear magnetoelectric material below its Néel temperature. Since it exhibits both the magnetoelectric and antiferromagnetic properties at room temperature, recently it gained considerable attention with the purpose of using it in multifunctional devices. In zero magnetic field the  $\text{Cr}^{3+}$  spins align themselves parallel to the threefold rhombohedral c-axis, forming an easy-axis antiferromagnet. The corresponding magnetic symmetry  $\bar{3}'m'$  is compatible with a linear ME effect. When the external magnetic field applied along the c-axis reaches a critical value of 10 T, spin flop (SF) transition occurs. SF transition refers to the change of direction of spins from being parallel to c-axis to be oriented perpendicular, i.e in the basal plane.

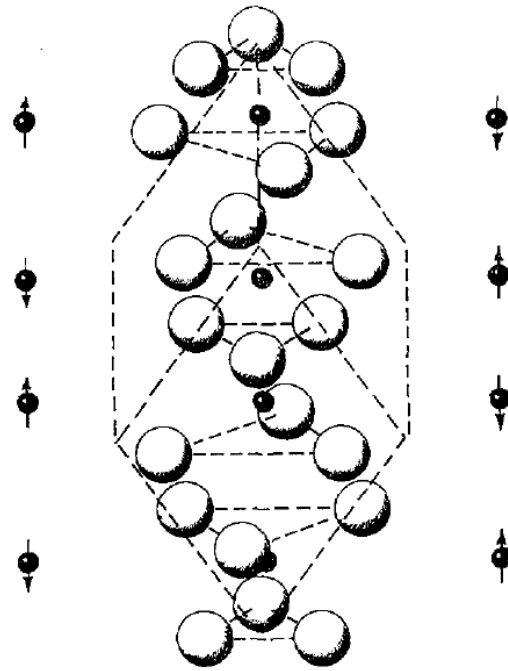


Figure 1.1: The Cr<sub>2</sub>O<sub>3</sub> lattice with rhombohedral unit cell showing the spin direction of Cr<sup>3+</sup> ions in the two antiferromagnetic domains 6.

Antiferromagnetic domains in single crystal Cr<sub>2</sub>O<sub>3</sub> have been postulated by Astrov <sup>3</sup> and Rado <sup>4</sup> to explain certain of their observations of the magnetoelectric effect in this material. For uniaxial crystals with common structural and magnetic axes, such as Cr<sub>2</sub>O<sub>3</sub>, the antiferromagnetic domains are related by 180-degree spin reversal, which are mathematically equivalent to time reversal <sup>7</sup>. Later T. J. martin *et al.*, <sup>6</sup> observed the controlled antiferromagnetic domain reversals in single crystal Cr<sub>2</sub>O<sub>3</sub> as shown in Figure 1.1. Switching between substantially single domain states has been achieved with the simultaneous application of electric and magnetic fields of approximately, 10 kV/cm and 5 kOe, respectively. The switching energy was nearly proportional to the product of the two switching fields. The switched domain state was stable even when the applied energy was reduced and when reversed in sign. The domain state switched back when its value reached

the same order of magnitude as the first threshold energy. The polarization was linear for low applied magnetic fields (<6 T) as shown in Figure 1.2(a) and the temperature variation of the magnetic susceptibility was as shown in Figure 1.2(b).

Controlling the magnetic configuration of the MRAM spintronic devices is of paramount importance. Different methods such as current induced domain switching<sup>8</sup> and magnetic switching by current arrays have been proposed<sup>9</sup>. Since the heat generated by the large currents limits the miniaturization of the devices, voltage controlled low current method was proposed<sup>10</sup>. The idea was to use the linear magnetoelectric effect of the Cr<sub>2</sub>O<sub>3</sub> to control the exchange of the FM in spintronic devices<sup>11, 12</sup>. Utilizing the magnetoelectric effect and the surface magnetism of the single crystal Cr<sub>2</sub>O<sub>3</sub>, isothermal voltage control was used to shift the hysteresis loop of the exchange biased ferromagnetic layer in contact with, instead of the regular field cooling procedure<sup>13</sup>. The ferromagnetic layer used for this was Pd<sub>0.5 nm</sub>/(Co<sub>0.6 nm</sub> Pd<sub>1.0 nm</sub>)<sub>3</sub>, which exhibits perpendicular exchange bias when in contact with the Cr<sub>2</sub>O<sub>3</sub> single crystal<sup>14</sup>.

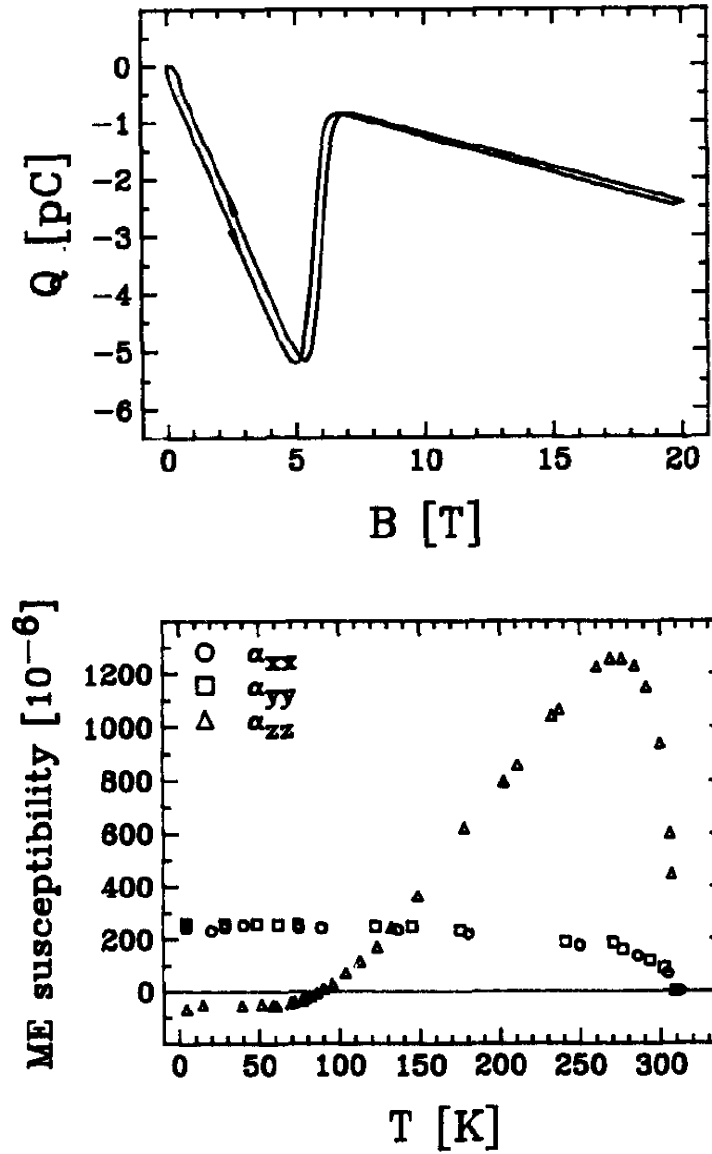


Figure 1.2: (a) The electric polarization along the  $z$ -direction with magnetic field parallel to  $z$ -direction. (b) Magnetic susceptibility variation with temperature <sup>15</sup>.

The existence of surface magnetization, required by symmetry in magnetoelectric antiferromagnets was proved in  $\text{Cr}_2\text{O}_3$  thin films as well <sup>16</sup>. For  $\text{Cr}_2\text{O}_3$  thin films grown on  $\text{Al}_2\text{O}_3$  substrate, direct observation of surface magnetization domains was demonstrated using photoemission electron microscopy with magnetic circular dichroism contrast and

magnetic force microscopy. The domain pattern was strongly affected by the applied electric field conditions. Zero-field cooling resulted in an equal representation of the two domain types, while electric-field cooling selected one dominant domain type. Perpendicular exchange magnetic anisotropy was observed in Pt/Co/Cr<sub>2</sub>O<sub>3</sub> all thin film system<sup>17, 18</sup>, when the Co layer thickness was less than 1.2 nm. The maximum unidirectional magnetic anisotropy energy was 0.33 erg/cm<sup>2</sup>. The perpendicular exchange bias appears in the direction perpendicular to the film independent of the easy direction of magnetization of the Co layer<sup>19, 20</sup>. But the voltage controlled exchange bias in all thin film system still remained as challenge.

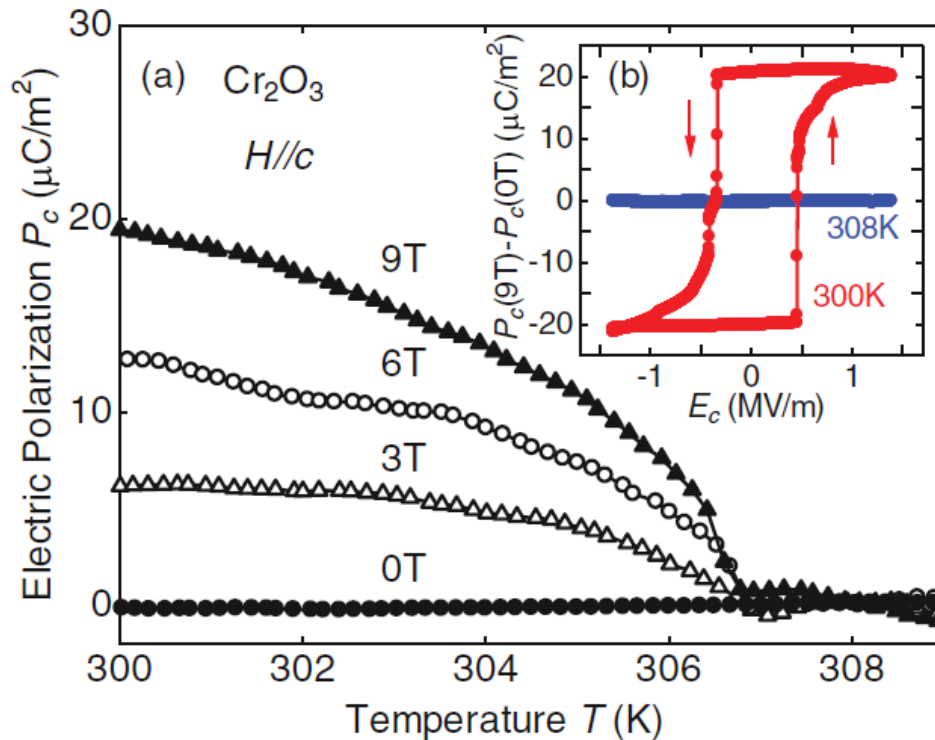


Figure 1.3: Temperature variation of electric polarization measured at various magnetic fields applied parallel to c-axis<sup>21</sup>.

Recently, the magnetoelectric effect in  $\text{Cr}_2\text{O}_3$  was revisited and magnetoelectric hysteresis loops were reproduced in single crystal samples<sup>21</sup>. The figure 1.3 shows the polarization as a function of temperature measured along the c-axis in the presence of magnetic field ranging from 0 T to 9 T. And the magnetization as a function of temperature measured in the external electric field parallel to the c-axis is shown in Figure 1.4.

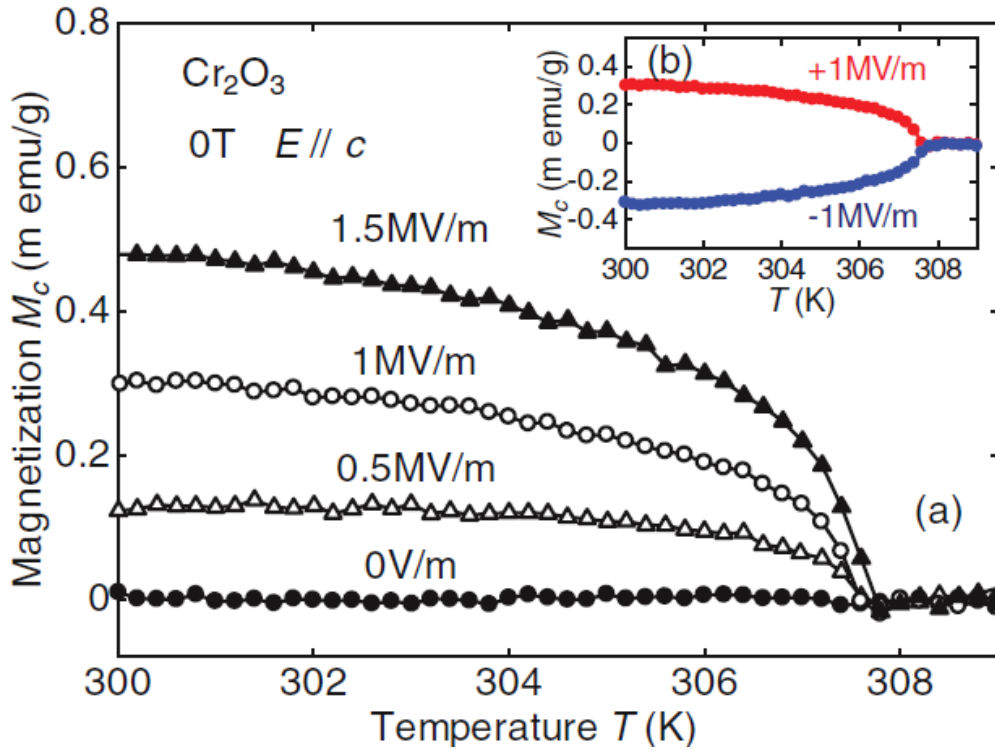


Figure 1.4: Temperature variation of magnetization measured at various electric fields applied along c-axis<sup>21</sup>.

### 1.3 Exchange Bias Effect

Exchange bias effect occurs when a ferromagnetic (FM) and antiferromagnetic (AFM) interface is cooled in the presence of a magnetic field through the Néel temperature ( $T_N$ ) of the AFM<sup>22, 23</sup>. It is accompanied by a shift of the hysteresis loop of the FM along the

magnetic field axis, denoted as exchange bias field  $H_{EB}$ . It is the phenomenon associated with the exchange anisotropy created at the interface between an FM and AFM materials. Meiklejohn and Bean discovered the exchange bias effect in 1956, when they were studying magnetic hysteresis loops of Co particles embedded in their natural antiferromagnetic CoO<sup>24</sup>. Exchange bias effect has also been observed in other types of interfaces involving ferrimagnet-FM<sup>25</sup> and ferrimagnet-AFM<sup>26</sup>. Exchange bias effect in thin film bilayers is more appropriate for the practical devices and is used to pin one of the ferromagnetic layer in magnetic tunnel junctions of MRAM devices. The cartoon in Figure 1.5 shows a simple picture for intuitive understanding of the exchange bias effect. Actual spin configurations and their rotation varies depending on the interface roughness, anisotropy, and magnetic domain structure.

The first phenomenological model of exchange bias is the Meiklejohn and Bean model<sup>22</sup>. The magnitude of the exchange bias field is given in terms of interface energy per unit area

$$\Delta E = M_{FM} t_{FM} H_{EB} \dots \dots \dots (1.2)$$

Where  $M_{FM}$  and  $t_{FM}$  are the saturation magnetization and thickness of the ferromagnet and  $H_{EB}$  is the exchange bias magnitude.

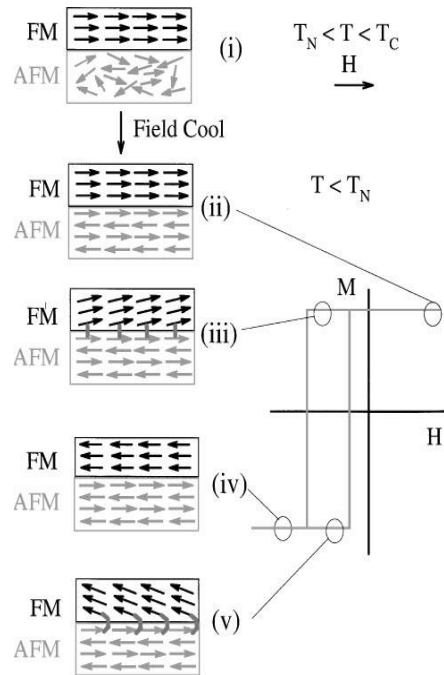


Figure 1.5: Schematic diagram showing the spin configuration of an FM-AFM bilayer at different stages of an exchange biased hysteresis loop <sup>27</sup>.

## 1.4 Magnetoresistance

Magnetoresistance refers to change in resistance of a material/junction when a magnetic field is applied. It finds applications in magnetic data storage, biosensors, magnetic sensors and microelectromechanical systems. There are different types of magnetoresistance and few of them are ‘giant’ and ‘tunneling’ magnetoresistance, which are described below.

### 1.4.1 Giant Magnetoresistance

The giant magnetoresistance (GMR) effect was discovered independently by Albert Fert and Peter Grünberg. It occurs in materials consisting of thin alternating layers of ferromagnetic and non-magnetic metals due to spin dependent transport within the system. The resistivity of the system depends on the relative alignment of the moments of the

ferromagnetic layers. Layers with parallel magnetic moments have lower resistance and layers with antiparallel magnetic moments have higher resistance. In Fe/Cr multilayers, it was found that when the thickness of the nonmagnetic Cr layers was decreased below 20 Å, the Fe layers were coupled antiferromagnetically<sup>28</sup>. With an external magnetic field, the magnetization of the Fe layers can be aligned parallel and the resistance of the multilayer structure decreases. GMR multilayers with 30 Fe/Cr layers showed changes of resistance of up to 50% at 4.2 K in a magnetic field of 2 Tesla, as can be seen in Figure 1.6. The resistance change generally decreases with increase in temperature.

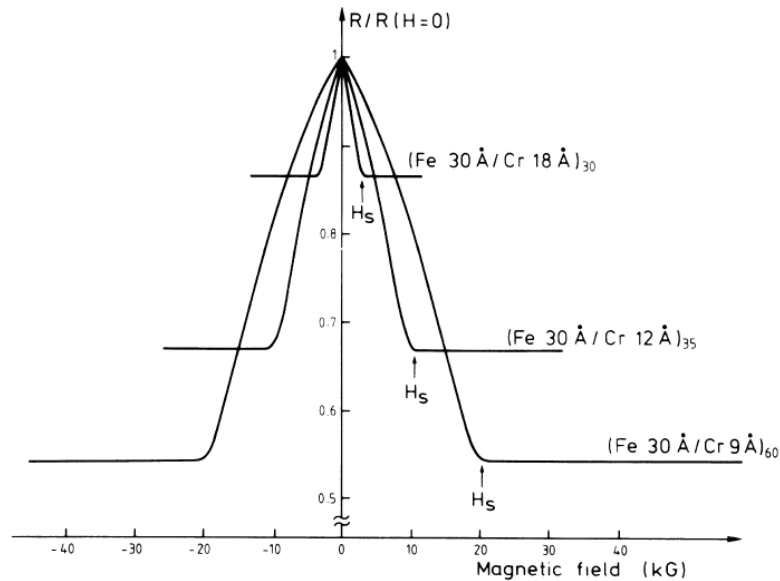


Figure 1.6: Magnetoresistance of three Cr/Fe multilayers measured at 4.2 K, in the CIP configuration<sup>28</sup>.

There are two principal configurations for the GMR system: the current-in-plane (CIP) configuration where the current flows in the plane of the layers, and the current perpendicular-to-plane (CPP) configuration where the current flows perpendicular to the

plane of the layers. In the same magnetic multilayer, CPP-GMR is usually found larger than CIP-GMR.

### 1.4.2 Tunneling Magnetoresistance

Tunneling magnetoresistance (TMR) is an effect that results by the application of magnetic field due to the spin dependent tunneling of electrons between two ferromagnetic (FM) films through a very thin insulating (I) barrier in magnetic tunnel junctions (MTJs). The resistance of MTJs depends on the relative orientations of the magnetizations of two FM films. In general the resistance is low with parallel (P), and high with anti-parallel (AP) alignments and a magnetic field is needed to switch from an AP to a P orientation. These two resistance states can be used to store binary bits of information. TMR is defined as  $(R_{AP} - R_P)/R_P$ , where  $R_{AP}$  and  $R_P$  are the tunnel resistances in anti-parallel and parallel orientations of the magnetization, respectively. It is often expressed as a percentage value.

The first experiment of TMR dates back to 1975 by Julliere, who observed a conductance change of 14% at 4.2 K in Fe/Ge/Co junctions <sup>29</sup>. The real curiosity in this field triggered with the observation of large resistance change of 18% at 300K in Fe/Al<sub>2</sub>O<sub>3</sub>/Fe and 11.8% at 298K in CoFe/Al<sub>2</sub>O<sub>3</sub>/Co junctions by Miyazaki <sup>30</sup> and Moodera <sup>31</sup>, respectively in 1995. The highest TMR value achieved at 300 K to date is 604%, using Co<sub>20</sub>Fe<sub>60</sub>B<sub>20</sub> electrodes and MgO barrier <sup>32</sup>. Figure 1.7 shows the percentage change of junction resistance with the magnetic field applied in the plane of the films.

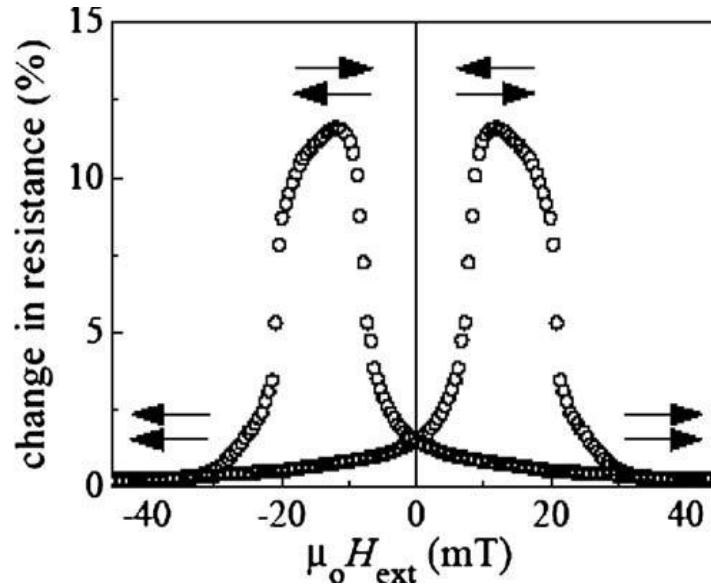


Figure 1.7: TMR effect at room temperature in CoFe/Al<sub>2</sub>O<sub>3</sub>/Co junctions. Arrows indicate the relative orientation of ferromagnetic electrodes <sup>30</sup>.

Based on Tedrow and Meservey's <sup>33</sup> analysis, Julliere <sup>29</sup> gave the expression for TMR as  $2P_1P_2/(1-P_1P_2)$  where  $P_1$  and  $P_2$  are the conduction electron spin polarizations of the two ferromagnetic materials. This is widely used general equation to estimate TMR for a specific pair of electrodes. If both electrodes have  $P=1$ , the above expression gives very high %TMR. Later from the experimental observations <sup>34</sup> it is understood that spin polarization 'P' of a ferromagnetic material is not a unique value and depends on the particular barrier used. It indicates the crucial role played by barrier material in determining the spin polarization and in turn the TMR values. The examples of half metals with 100% spin polarization include La<sub>0.7</sub>Sr<sub>0.3</sub>MnO<sub>3</sub>, Fe<sub>3</sub>O<sub>4</sub> and CrO<sub>2</sub>. In MTJs made of two different FM electrodes having different coercivities, an external magnetic field can change the orientation from antiparallel to parallel. On the other hand if both FM electrodes are similar, the direction of magnetization of one of the electrodes needs to be fixed/pinned so that external field can only

change that of other electrode. This pinning could be done by exchange coupling/biasing the electrode with an antiferromagnetic layer, whose  $T_N$  is greater than  $T_C$  of the FM layer.<sup>35</sup>

### 1.5 $\text{La}_{1-x}\text{Sr}_x\text{MnO}_3$

Many complex oxides such as Sr doped lanthanum manganese oxides  $\text{La}_{1-x}\text{Sr}_x\text{MnO}_3$ , are highly ionic and take the form of the perovskite crystal structure. The generalized perovskite crystal has a chemical composition of  $\text{ABO}_3$  in a simple cubic lattice as shown in Figure 1.8 with a motif of  $(0,0,0)_A$ ,  $(0.5, 0.5, 0.5)_B$ ,  $(0, 0.5, 0.5)_O$ ,  $(0.5, 0, 0.5)_O$ ,  $(0.5, 0.5, 0)_O$ . The Sr substitutes for La and occupies  $(0,0,0)_A$  sites. In LSMO, the A-site cation will assume an ionic state ( $\text{La}^{3+}$  and  $\text{Sr}^{2+}$ ) without any valence electrons and the B-site cations are at the center of an octahedron of oxygen atoms.

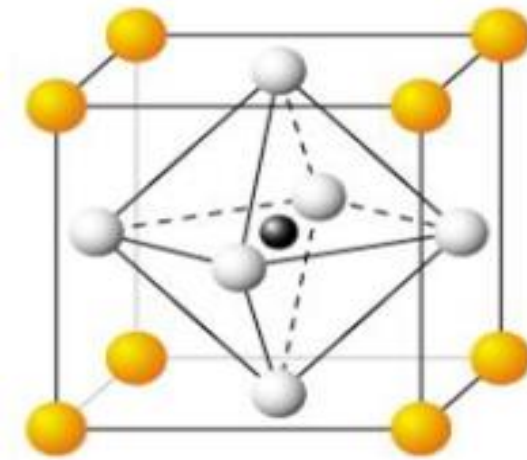


Figure 1.8: The schematic of the perovskite unit cell of  $\text{ABO}_3$ . Yellow: La and/or Sr; Black: Mn; White: O.

The Sr doping leads to the formation of a mixed valence state of the Mn ( $\text{Mn}^{3+}$  and  $\text{Mn}^{4+}$ ) to maintain the charge neutrality of the system<sup>36</sup>. The majority of the electronic interactions related to magnetism and electron transport will be confined to the B-site cations and oxygen

anions. The mixed valence of the Mn ions in similar perovskite complex oxides may also be controlled by varying the oxygen content <sup>37,38</sup>. At intermediate hole doping,  $\text{La}_{1-x}\text{Sr}_x\text{MnO}_3$  has a high Curie temperature of 370 K <sup>39</sup>. In  $\text{La}_{1-x}\text{Sr}_x\text{MnO}_3$  a structural transition occurs from orthorhombic ( $x > 20\%$ ) to rhombohedral ( $x < 20\%$ ) <sup>40</sup>. Depending on the Sr doping, one can obtain ferromagnetic or antiferromagnetic metallic phases, as well as antiferromagnetic insulating phases. In the present study we are interested in the composition  $\text{La}_{0.7}\text{Sr}_{0.3}\text{MnO}_3$ , which is a hole doped room temperature ferromagnetic metal with a Curie temperature of 370 K <sup>39</sup>.

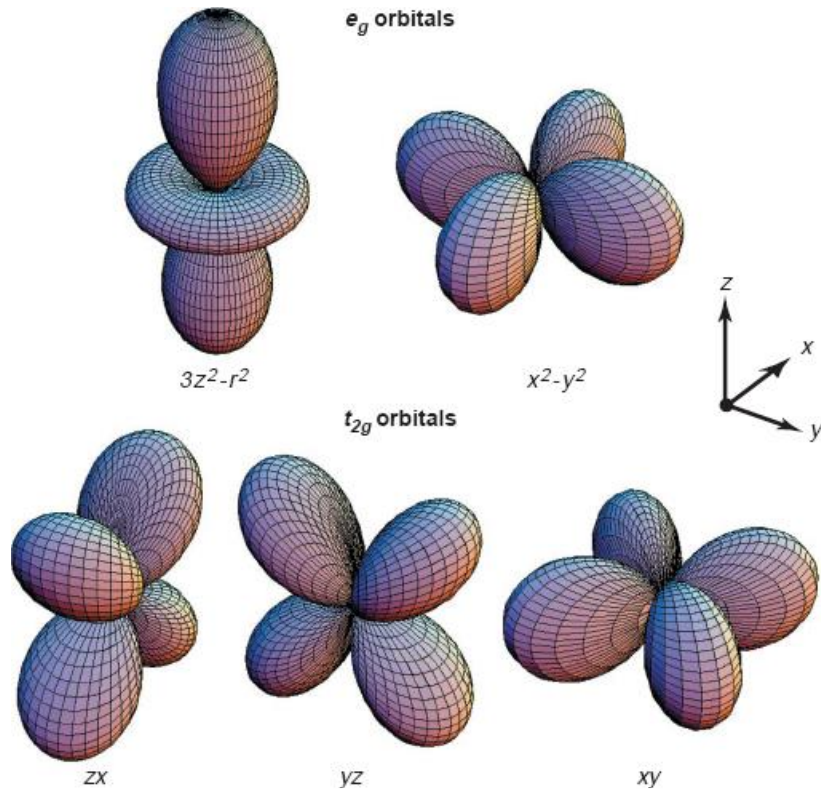


Figure 1.9: Five d orbitals of Mn in  $\text{LaMnO}_3$ . In the cubic crystal field, this fivefold degeneracy is lifted into two  $e_g$  orbitals ( $(x^2 - y^2)$  and  $(3z^2 - r^2)$ ) and three  $t_{2g}$  orbitals ( $(xy)$ ,  $(yz)$  and  $(zx)$ ) <sup>41</sup>.

The physical properties of LSMO involve a complex interplay between the spin, charge, orbital and lattice degrees of freedom, which strongly depend on the site of occupancy of the d orbitals. For LaMnO<sub>3</sub>, in the cubic environment of the MnO<sub>6</sub> octahedron, a crystal field will be generated by the hybridization and electrostatic interaction with oxygen 2p electrons for the outer 3d electrons in Mn<sup>3+</sup>. This crystal field lifts the fivefold degeneracy of the d orbitals (Figure 1.9) in free Mn<sup>3+</sup> ions. The splitting of the energy levels results in the formation of low lying triply degenerate  $t_{2g}$  states and higher doublet  $e_g$  states<sup>42</sup>, as shown in Figure 1.10. The low lying  $t_{2g}$  triplet consists of the  $d_{xy}$ ,  $d_{yz}$  and  $d_{zx}$  orbitals and these orbitals have lobes oriented between the O<sup>2-</sup> ions. The higher energy  $e_g$  doublet consists of  $d_{x^2-y^2}$  and  $d_{3z^2-r^2}$  orbitals and their lobes point in the directions of the O<sup>2-</sup> ions. Due to coulombic repulsion, the lowest energy d-orbitals are those that are farthest from the orbitals of the neighboring atoms. A distortion of the oxygen octahedron further removes the degeneracy of the  $e_g$  orbitals due to the orbital–lattice interaction and is called Jahn–Teller distortion.

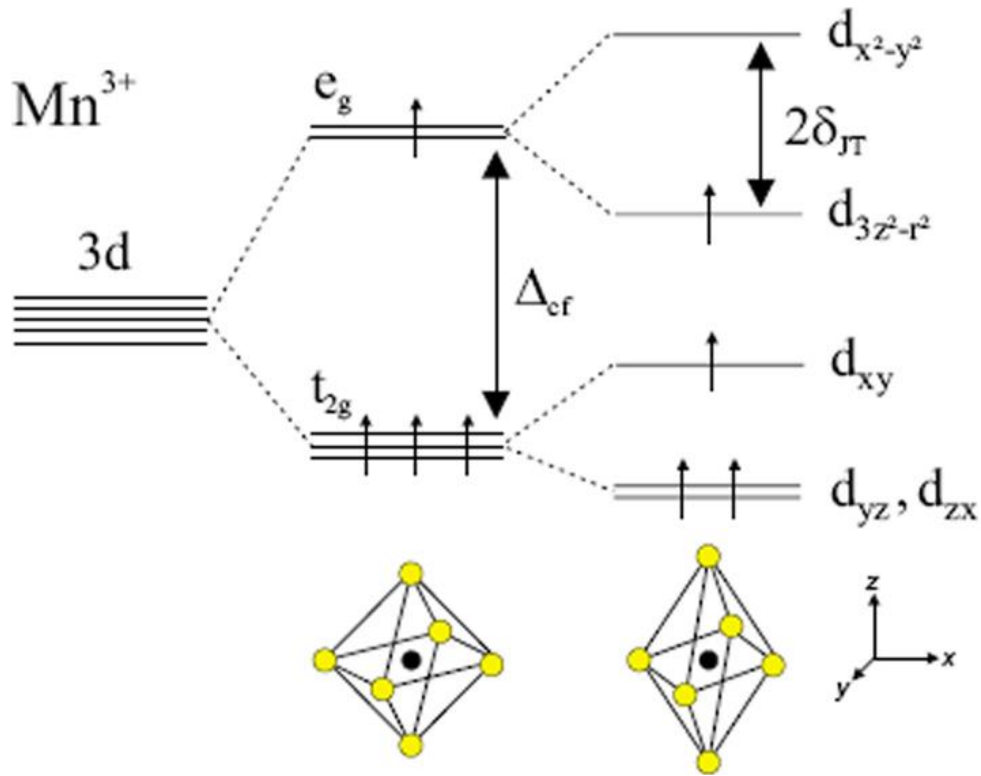


Figure 1.10: Crystal field splitting of the 3d orbitals of  $Mn^{3+}$  and further degeneracy removal of the  $e_g$  orbital due to Jahn–Teller distortion <sup>43</sup>.

The LSMO is a ferromagnetic conducting oxide, in which the electron conduction occurs through a hopping mechanism. Since La and Sr have the stable oxidation states of 3+ and 2+, respectively, the Mn ions are left in a combination of 3+ and 4+ oxidation states. Zener gave an intuitive explanation for the ferromagnetism, as arising from an indirect coupling between ‘incomplete d shells’ of  $Mn^{3+}$  and  $Mn^{4+}$  via ‘conducting electrons’ of oxygen, which is called double exchange mechanism <sup>44</sup>. The mixed valence Mn oxidation states correspond to electron configurations of  $t_{2g}^3 e_g^1$  and  $t_{2g}^3$ , which is shown in Figure 1.11. Here, a competition occurs between the crystal field energy and Hund's pairing energy. The crystal field energy splits the 3d levels and favors occupation of the  $t_{2g}$  states whereas Hund's energy favors a maximization of the total spin quantum number. The final electron configuration will

therefore be determined by the relative strengths of the crystal field and pairing energy. In LSMO, the Hund's pairing energy dominates and the movement of the  $e_g$  electron of the  $Mn^{3+}$  ion through the crystal is facilitated by the overlap between the Mn d-orbitals and the O p-orbitals. The  $t_{2g}$  electrons encounter the on-site repulsion and are consequently localized. Electron transfer is more energetically favorable if neighboring moments are aligned, so reducing the kinetic energy term and hence ferromagnetism.

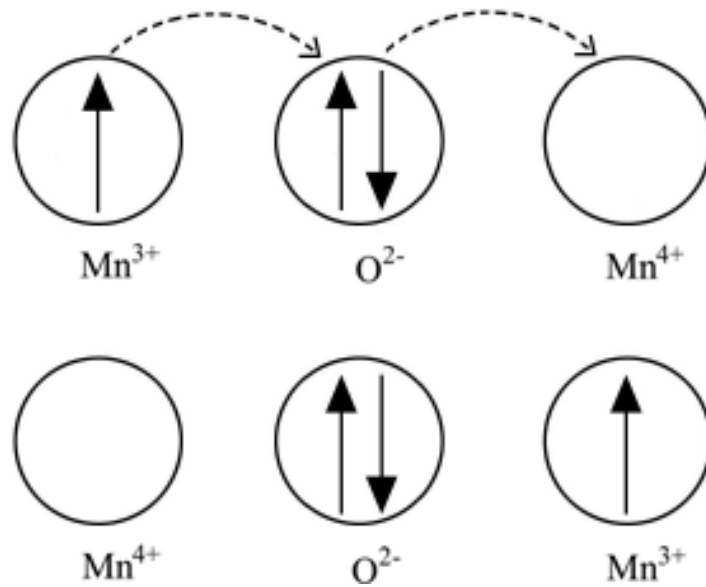


Figure 1.11: Schematic of the double exchange mechanism between  $Mn^{3+}$  and  $Mn^{4+}$  ions proposed by Zener<sup>44</sup>.

The  $La_{0.7}Sr_{0.3}MnO_3$  exhibits colossal magnetoresistance and Half metals are the materials with 100% spin polarization at the Fermi level, This term is derived from their ability to act as a metal for one spin orientation, but an insulator for the other spin orientation.

## 1.6 Thin Film Epitaxy

Epitaxy is an important concept in thin films and has its roots in two ancient Greek words  $\epsilon \pi \iota$  (epi - placed or resting upon) and  $\tau \alpha \xi \iota \xi$  (taxis - arrangement). In thin films context, epitaxy refers to the formation of an extended single-crystalline film on top of a crystalline substrate. Epitaxy is broadly categorized into two forms, called homoepitaxy and heteroepitaxy. In homoepitaxy, the film and substrate are made of same material, where as they are different in heteroepitaxy. An example of homoepitaxy is growth of epitaxial Si film on Si substrate and an example of heteroepitaxy is growth of Ge film on Si substrate. The heteroepitaxy is of technological significance, which allows the growth of novel materials and devices on commonly used substrate systems such as Si and  $\text{Al}_2\text{O}_3$ . The lattice misfit between the substrate and film is the key parameter that controls the growth, morphology, and properties of the film. The lattice misfit strain is defined as:

$$\text{strain} = \frac{a_f - a_s}{a_s} \dots\dots\dots (1.3)$$

Where  $a_f$  is lattice constant of film and  $a_s$  is lattice constant of substrate. Now we will discuss two types of epitaxy.

### 1.6.1 Lattice Matching Epitaxy

In lattice matching epitaxy (LME), there is a one-to-one matching of the lattice parameters of the film and substrate across the interface. The lattice matching epitaxy is applicable when the misfit strain is less than 7 – 8 %. In LME, the film grows pseudomorphically until it reached a critical thickness, above which strain energy becomes high enough to initiate the nucleation of dislocations to relax the film. The critical thickness

at which dislocation nucleation occurs is directly related to the misfit. In low misfit systems the critical thickness for dislocation nucleation may be quite large and dislocation nucleation and therefore, strain relaxation are difficult to achieve.

### 1.6.1 Domain Matching Epitaxy

In case of systems with lattice misfit larger than 7-8%, the conventional lattice matching epitaxy is unable to explain the thin film epitaxy based on one-to-one matching of lattice parameter across the film/substrate interface. LME predicts that for larger misfits the thin film growth converts to textured or poly-crystalline growth instead of epitaxial growth. However, heterostructure epitaxial growth is observed in some of large lattice misfit systems (>7-8%), such as ZnO(0001)/Al<sub>2</sub>O<sub>3</sub>(0001), GaN(0001)/Al<sub>2</sub>O<sub>3</sub>(0001), AlN(0001)/Si(111) and TiN(100)/Si(100). Epitaxial growth in such systems can be explained under the framework of domain matching epitaxy (DME), which was proposed by Narayan et al <sup>45</sup>. Based on the domain matching epitaxy theory, an epitaxial film can be deposited on the substrate with different orientations. Under the DME framework, the film adopts either a fixed or the same orientation relationship with the substrate, depending upon the nature of the misfit. The misfit is accommodated by matching of integral multiples of lattice planes, where one extra half plane (dislocation) corresponding to each domain. The schematic in Figure 1.12 illustrates such an example of growth of film. In DME, the strain can be relieved within a couple of monolayers, so that the misfit strain and dislocations can be engineered to confine close to the interface. The residual strain is minimized by matching of m planes of films with n planes of substrate, given as

$$\epsilon_r = \frac{md_f}{nd_s} - 1 \dots\dots\dots (1.4)$$

Where  $m$  and  $n$  are simple integers and  $d_f$  and  $d_s$  are the inter-planar spacing of film and substrate, respectively. If the misfit corresponds to the perfect matching ratios of planes ( $md_f = nd_s$ ), the residual strain will be zero. On the other hand, if the misfit falls away from perfect matching, the residual strain is relieved by two domains, alternating with a certain frequency ( $\alpha$ ) to provide for a zero residual strain, given as

$$(m + \alpha)d_f = (n + \alpha)d_s \dots\dots\dots (1.5)$$

Where  $\alpha$  is the domain variation parameter. For example, if  $\alpha = 0.5$ , then  $m/n$  and  $(m+1)/(n+1)$  domains alternate with an equal frequency.

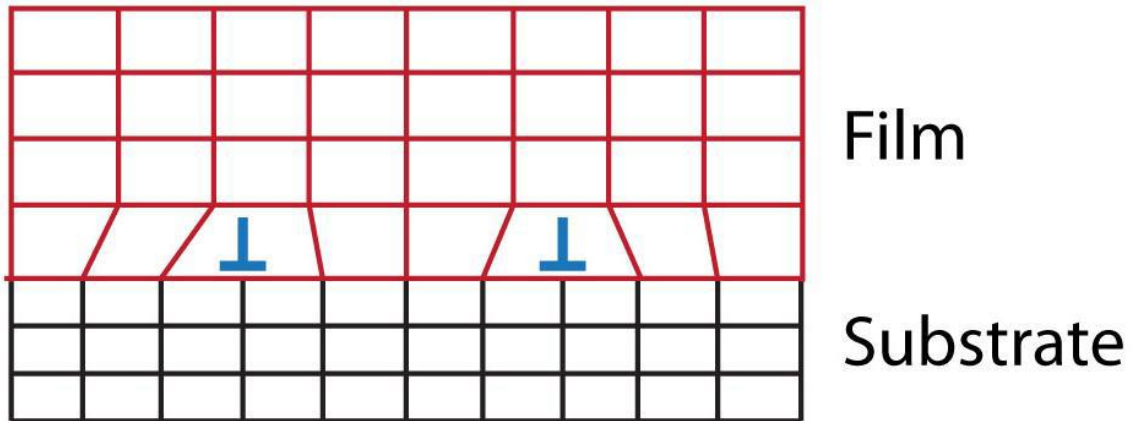


Figure 1.12: Schematic representation of domain matching epitaxy (DME), in which three lattice planes of film match with four lattice planes of substrate.

## 1.9 References

1. L. D. Landau and E. M. Lifshitz, *Electrodynamics of Continuous Media* (Addison-Wesley Publishing Company, Inc., Reading, Massachusetts, 1960), p. 119. (English translation of a 1958 Russian edition.)
2. E. Dzyaloshinskii, *J. Exptl. Theoret. Phys. (U.S.S.B.)* **37**, 881 (1959) [ translation: *Soviet Phys .—JETP* **10**, 628 (1960)].
3. D.N. Astrov, *Sov. Phys. JETP* **13**, 729 (1961).
4. G.T. Rado and V.J. Folen, *Phys. Rev. Lett.* **7**, 310 (1961).
5. V.J. Folen, G.T. Rado, and E.W. Stalder, *Phys. Rev. Lett.* **6**, 607 (1961).
6. T.J. Martin and J.C. Anderson, *IEEE Trans. Magn.* **2**, 446 (1966).
7. R.R. Birss, *Reports Prog. Phys.* **26**, 307 (1963).
8. E.B. Myers, *Science* (80-. ). **285**, 867 (1999).
9. G.A. Prinz, *Science* (80-. ). **282**, 1660 (1998).
10. X. Chen, A. Hochstrat, P. Borisov, and W. Kleemann, *Appl. Phys. Lett.* **89**, 202508 (2006).
11. P. Borisov, A. Hochstrat, X. Chen, W. Kleemann, and C. Binek, *Phys. Rev. Lett.* **94**, 117203 (2005).
12. C. Binek, A. Hochstrat, X. Chen, P. Borisov, W. Kleemann, and B. Doudin, *J. Appl. Phys.* **97**, 10C514 (2005).
13. X. He, Y. Wang, N. Wu, A.N. Caruso, E. Vescovo, K.D. Belashchenko, P.A.

Dowben, and C. Binek, *Nat. Mater.* **9**, 579 (2010).

14. P. Borisov, A. Hochstrat, X. Chen, W. Kleemann, and C. Binek, *Phys. Rev. Lett.* **94**, 117203 (2005).

15. H. Wiegmann, A.G.M. Jansen, P. Wyder, J.-P. Rivera, and H. Schmid, *Ferroelectrics* **162**, 141 (1994).

16. N. Wu, X. He, A.L. Wysocki, U. Lanke, T. Komesu, K.D. Belashchenko, C. Binek, and P.A. Dowben, *Phys. Rev. Lett.* **106**, 087202 (2011).

17. Y. Shiratsuchi, Y. Takechi, K. Toyoki, Y. Nakano, S. Onoue, C. Mitsumata, and R. Nakatani, *123004*, 2 (2014).

18. Y. Shiratsuchi, H. Noutomi, H. Oikawa, T. Fujita, and R. Nakatani, *J. Appl. Phys.* **109**, 07C101 (2011).

19. Y. Shiratsuchi, T. Nakatani, S. Kawahara, and R. Nakatani, *J. Appl. Phys.* **106**, 033903 (2009).

20. Y. Shiratsuchi, S. Kawahara, H. Noutomi, and R. Nakatani, *IEEE Trans. Magn.* **46**, 1618 (2010).

21. A. Iyama and T. Kimura, *Phys. Rev. B* **87**, 180408 (2013).

22. W.H. Meiklejohn, *J. Appl. Phys.* **33**, 1328 (1962).

23. W.H. Meiklejohn and C.P. Bean, *Phys. Rev.* **105**, 904 (1957).

24. W.H. Meiklejohn and C.P. Bean, *Phys. Rev.* **102**, 1413 (1956).

25. P.J. van der Zaag, A.R. Ball, L.F. Feiner, R.M. Wolf, and P.A.A. van der Heijden, J.

Appl. Phys. **79**, 5103 (1996).

26. W.C. Cain and M.H. Kryder, J. Appl. Phys. **67**, 5722 (1990).

27. J. Nogués and I.K. Schuller, J. Magn. Magn. Mater. **192**, 203 (1999).

28. M.N. Baibich, J.M. Broto, A. Fert, F.N. Van Dau, and F. Petroff, Phys. Rev. Lett. **61**, 2472 (1988).

29. M. Julliere, Phys. Lett. A **54**, 225 (1975).

30. T. Miyazaki and N. Tezuka, J. Magn. Magn. Mater. **139**, L231 (1995).

31. J.S. Moodera, L.R. Kinder, T.M. Wong, and R. Meservey, Phys. Rev. Lett. **74**, 3273 (1995).

32. S. Ikeda, J. Hayakawa, Y. Ashizawa, Y.M. Lee, K. Miura, H. Hasegawa, M. Tsunoda, F. Matsukura, and H. Ohno, Appl. Phys. Lett. **93**, 082508 (2008).

33. P.M. Tedrow and R. Meservey, Phys. Rev. Lett. **26**, 192 (1971).

34. J.M. De Teresa, Science (80-. ). **286**, 507 (1999).

35. E. V. Khomenko, N.G. Chechenin, A.Y. Goikhman, and A. V. Zenkevich, JETP Lett. **88**, 602 (2009).

36. G.H. Jonker and J.H. Van Santen, Physica **16**, 337 (1950).

37. Y.G. Zhao, M. Rajeswari, R.C. Srivastava, A. Biswas, S.B. Ogale, D.J. Kang, W. Prellier, Z. Chen, R.L. Greene, and T. Venkatesan, J. Appl. Phys. **86**, 6327 (1999).

38. W. Prellier, A.M. Haghiri-Gosnet, B. Mercey, P. Lecoeur, M. Hervieu, C. Simon, and B. Raveau, Appl. Phys. Lett. **77**, 1023 (2000).

39. A. Urushibara, Y. Moritomo, T. Arima, A. Asamitsu, G. Kido, and Y. Tokura, Phys. Rev. B **51**, 14103 (1995).
40. J. Dho, W.S. Kim, and N.H. Hur, Phys. Rev. Lett. **87**, 187201 (2001).
41. Y. Tokura, Science (80-. ). **288**, 462 (2000).
42. Cox P A 1995 Transition Metal Oxides: An Introduction to Their Electronic Structure and Properties (Oxford: Clarendon).
43. Tokura Y (ed), 2000 *Colossal Magnetoresistive Oxides* (London: Gordon and Breach).
44. C. Zener, Phys. Rev. **81**, 440 (1951).
45. J. Narayan and B.C. Larson, J. Appl. Phys. **93**, 278 (2003)

## Chapter 2 Experimental Methods

### 2.1 Pulsed Laser Deposition

Pulsed laser deposition (PLD) is a versatile non-equilibrium physical vapor deposition technique to grow thin films of material. In 1965, laser-assisted growth was first demonstrated by Smith et. al.<sup>1</sup>, using a high power ruby laser. However major milestone in PLD thin film deposition occurred in 1987 when the growth of  $\text{YBa}_2\text{Cu}_3\text{O}_7$  superconducting thin films was demonstrated on sapphire substrate by Dijkkamp et. al.<sup>2</sup>. Since it can precisely control complex stoichiometry, it became popular to synthesize variety of high quality oxide thin films. The schematic in Figure 2.1 depicts the pulsed laser deposition assembly. It makes use of a high-powered laser to vaporize a polycrystalline target material and the resulting plume gets deposited on the substrate in thin film form. The target material should be dense and uniform in composition. The whole deposition process takes place in a vacuum chamber. During the deposition some oxygen background pressure is used to control the kinetic energy of the species in the plume. The main advantage of PLD arises due to the high energy of the ablated species<sup>3,4</sup>. The energy of the ablated species can be as high as 10 to 100 eV, which is very high compared with the energy of the ejected species in thermal and electron beam evaporation techniques. For example, the thermal energy ( $KT$ ) at 1200 K is about 0.1 eV. The high kinetic energy of the species helps to form good crystalline films at comparatively reduced temperatures.

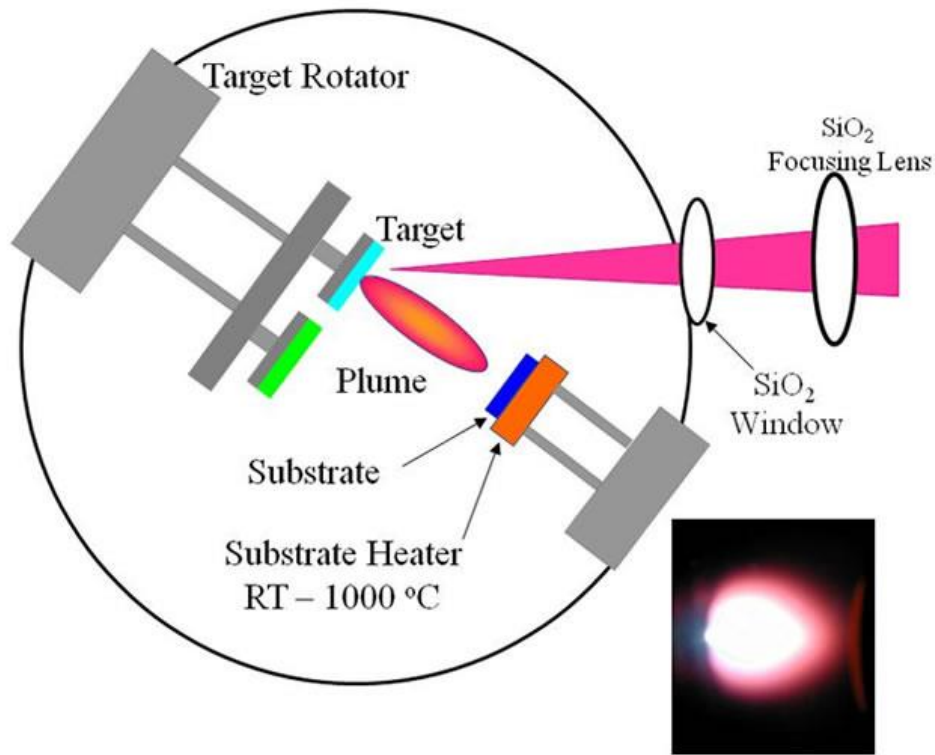


Figure 2.1: Schematic diagram showing the pulsed laser deposition assembly.

The plume in PLD is forward directed and so imposes restriction on the position of the substrate and any deviation from this result in thickness non-uniformity. Since the target carousel is capable of holding 4 or 6 targets, multilayer thin films can be deposited in-situ without breaking the vacuum. One main disadvantage of the PLD is that samples larger than 1x1 cm<sup>2</sup> in size suffer from variation in film thickness because of the more directional nature of the plume. Another drawback of PLD is the formation of chunks on the film, which degrades the quality of the film. All samples in this work were deposited using pulsed laser deposition with a KrF excimer laser of 248 nm wavelength and 25 ns pulse duration.

## 2.2 X-ray Diffraction

X-ray diffraction (XRD) was used to study the crystalline nature, quality and to obtain the epitaxial relationships between the substrate and buffer layers. It also provides information about the phase composition, lattice parameter, and lattice strain. The XRD technique is based on the principle of diffraction governed by the Bragg's law. Generally, diffraction occurs when waves of wavelength of the same order as the repeat distance of the periodic structure interacts with the periodic structure. Since X-rays have wavelengths few angstroms, which is of the same order as the inter-atomic distances in crystals, they are used to investigate the crystals. When an X-ray beam is incident at an angle of  $\theta$  on parallel planes of atoms, the waves interact either constructively or destructively depending upon the path difference. For the constructive interference, the path difference should be equal to the integral multiples of wavelength as given by Bragg's law <sup>5</sup>.

$$n\lambda = 2d \sin\theta \dots\dots\dots 2.1$$

Where  $n$  is an integer indicating the order of reflection,  $\lambda$  is the wavelength of the X-ray beam,  $d$  is the inter-planar spacing and  $\theta$  is the incident angle. Bragg's law is the necessary condition for the diffraction to occur but not sufficient. The schematic of an XRD system in the  $\theta$ - $2\theta$  configuration is shown in Figure 2.2. In the  $\theta$ - $2\theta$  scan, the sample moves by  $\theta$  and the detector measures the diffracted beam at an angle  $2\theta$  and moves by  $2\theta$ . Copper  $K\alpha$  x-rays of wavelength  $1.54 \text{ \AA}$  were used for the diffraction. The X-ray diffraction is a non-destructive technique which provides crystal information from a relatively large area of the sample and requires minimal sample preparation.

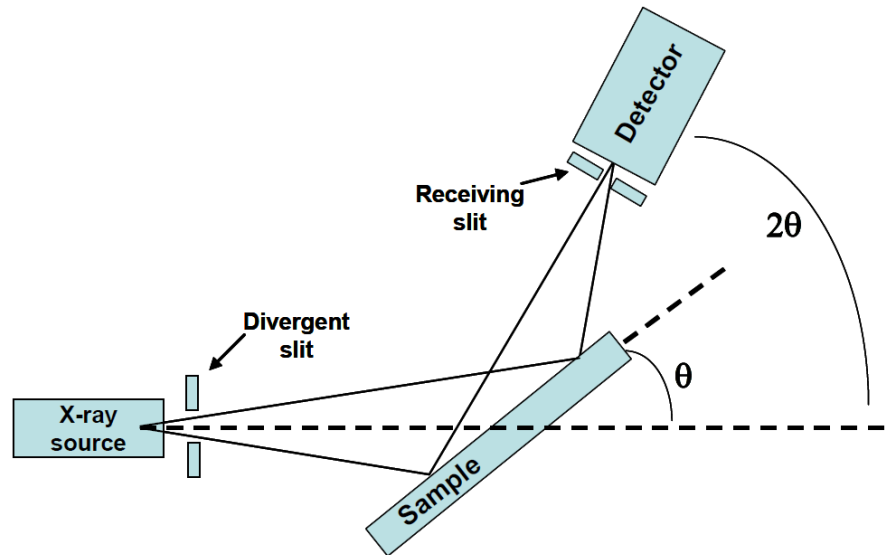


Figure 2.2: Schematic representation of XRD  $\theta$ - $2\theta$  scan configuration.

One disadvantage of the XRD is that it is difficult to detect if the amount of material is less than 10 % by weight and hence particles or precipitates with sizes in the nano-regime may not be detected. The two-circle diffractometer gives information about the growth orientation and a four-circle diffractometer is used to know the in-plane orientations of thin films to establish the epitaxy.

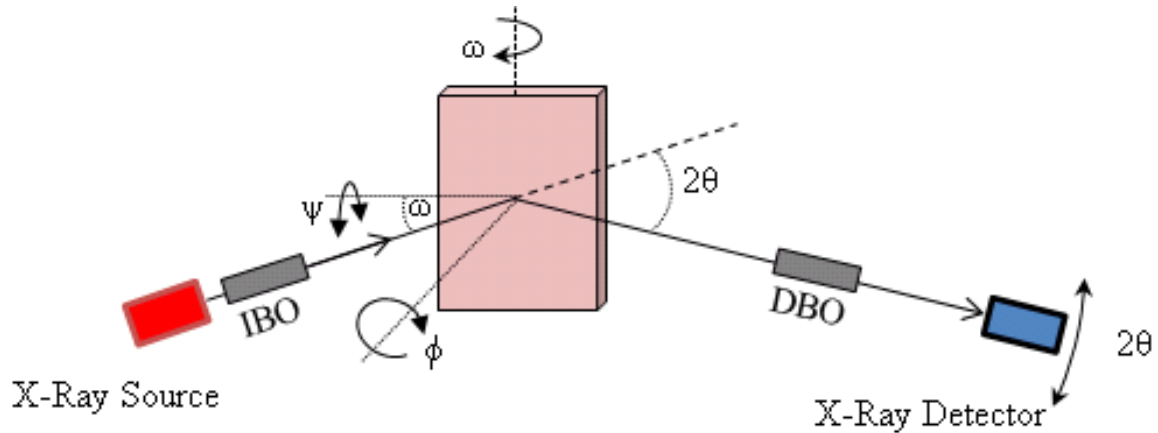


Figure 2.3: Schematic representation of the Philips X'Pert diffractometer used for  $\varphi$ -scans. IBO: Incident beam optics, DBO: diffracted beam optics

In four-circle diffractometer, in addition to rotation along  $\theta$ - and  $2\theta$ -axis, the sample can be tilted with respect to the incident beam ( $\psi$ -axis) and also rotated  $360^\circ$  around the surface normal ( $\varphi$ -axis). A schematic diagram of the four-circle diffractometer is shown in Figure 2.3. The in-plane epitaxial relationships can be established by  $\varphi$ -scans. To perform a  $\varphi$ -scan an appropriate crystallographic plane ( $hkl$ ), which is inclined at an angle  $\psi$  to the growth/sample surface plane, is identified. The  $\theta$  and  $2\theta$  angles are set corresponding to Bragg angle for the identified plane. The sample will be tilted to  $\psi$  angle and the diffraction intensity will then be recorded as a function of sample rotation along  $\varphi$ -axis. The epitaxial film exhibits sharp peaks at certain  $\varphi$ -angles in the  $\varphi$ -scan.

### 2.3 Transmission Electron Microscopy

Cross-sectional transmission electron microscopy (TEM) was performed on the samples to study the interface microstructure, estimate the thickness of the layers and to verify the epitaxial relationships. JEOL 2010F and the aberration corrected STEM–FEI Titan

80-300 microscopes were used in this study. The imaging techniques mainly used were: bright field, high resolution phase contrast and STEM-Z imaging. Selected area diffraction (SAED) was performed to identify the crystalline nature and epitaxy.

The cross section TEM samples were prepared by a series of steps including mechanical polishing, and ion-milling. To begin with, two small sample pieces (about 2 x 2 mm) were stuck together using an M-Bond 610 adhesive with the film side facing each other. The sample attached to a pyrex stub was mechanically flat polished on one side until mirror finish and nearly scratch free. After that it was flipped to other side and flat polished until 40  $\mu\text{m}$  thickness after which it was wedge polished ( $2^\circ$ ) until 1  $\mu\text{m}$  thickness. For these purposes, a series of diamond papers with reducing grit sizes were used. Final polish was usually done on a felt wheel using 0.05 micron colloidal silica slurry. When the sample is about 1  $\mu\text{m}$  thickness, it exhibits fringes when observed under optical microscope. Once the wedge polish was done, a ring of 3.05 mm diameter made up of Ta or Mo was attached to the sample with the thin region at the center of the ring. The combined sample was then ion milled until electron transparency.

## 2.4 Magnetic Measurements

All the magnetic measurements were performed in Quantum Design Magnetic Property Measurement System (MPMS) incorporating SQUID magnetometer. SQUID stands for superconducting quantum interference device. SQUID magnetometer is composed of a pickup coil with two Josephson junctions in parallel and allows the detection of changes in magnetic flux as small as single magnetic flux quanta [48]. SQUID is a very sensitive instrument and we were able to resolve magnetic signals as small as  $1 \times 10^{-7}$  emu. The MPMS is capable of reaching fields as high as 7 T and the temperatures ranging from 2-400K.

In-plane magnetic measurements were performed with magnetic field lying in the plane of the sample whereas out-of-plane measurements were performed with magnetic field applied along the sample normal. Two types of measurements were performed; M-H hysteresis loops and M-T measurement. For M-H loops, generally the sample was cooled down to the particular temperature of measurement from room temperature and the magnetization was measured as a function of field. For exchange bias study, the sample was cooled from above the Neel temperature of the AFM under certain applied field after which M-H measurement was performed. Since SQUID measures the bulk moment of the whole sample (films + substrate) the substrate and buffer layer diamagnetic contributions has to be subtracted. The diamagnetic contribution appears as a straight line in the magnetic moment vs. applied field data and can be subtracted using the slope multiplied by field from the obtained data.

## 2.5 Transport and Magneto-transport Measurements

The transport and magneto-transport measurements were performed on 5mmx5mm samples in Quantum Design, EverCool-II PPMS with base temperature down to 2 K and magnetic field up to 9.0 T. PPMS stands for physical property measurement system. For both the measurements four indium dots were mechanically pressed on the corners of the sample and resistance measurements were performed in four probe van der Pauw configuration. The sample with pressed indium dots was mounted on a custom built rotatable pogo-pin setup in the PPMS. The magneto-transport measurements were performed in AC delta mode with model 6000 PPMS controller to measure magnetoresistance accurately without any error in the measurements. The magnetoresistance was measured along XX direction with applied perpendicular field along ZZ direction. In the next step, the sample was rotated by 90 degree

to apply in-plane magnetic field along XX direction and in-plane magneto-resistance was measured along the same XX direction.

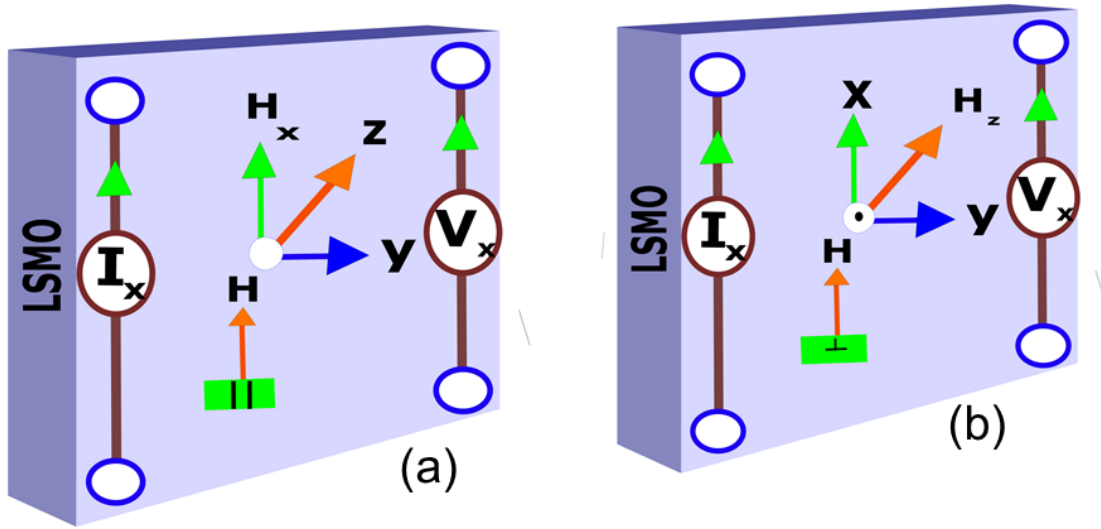


Figure 2.4: Schematics of the magneto-resistance measurements. (a) In-plane magneto-resistance. (b) Out-of-plane Magneto-resistance.

## 2.5 References

1. H. M. Smith and A. F. Turner, *Appl. Opt.* **4**, 147 (1965)
2. D. Dijkkamp, T. Venkatesan, X. D. Wu, S. A. Shaheen, N. Jisrawi, Y. H. Min-Lee, W. L. McLean, and M. Croft, *Appl. Phys. Lett.* **51**, 619 (1987).
3. R. K. Singh, O. W. Holland, and J. Narayan, *J. Appl. Phys.* **68**, 233 (1990)
4. R. K. Singh and J. Narayan, *Phys. Rev. B* **41**, 8843 (1990).
5. Cullity, B.D., *Elements of X-Ray Diffraction*. 1982, Addison-Wesley Publishing Co. Inc.

# Chapter 3 Strain induced ferromagnetism in epitaxial Cr<sub>2</sub>O<sub>3</sub> thin films integrated on Si(001)

Published in Applied Physics Letters, Volume 105, (2014) 132401 doi: 10.1063/1.4896975

Sandhyarani Punugupati, Jagdish Narayan and Frank Hunte

*Department of Materials Science and Engineering, North Carolina State University, Raleigh, NC- 27695*

## 3.1 Abstract:

We report on the epitaxial growth and magnetic properties of antiferromagnetic and magnetoelectric (ME) Cr<sub>2</sub>O<sub>3</sub> thin films deposited on cubic yttria stabilized zirconia (c-YSZ)/Si(001) using pulsed laser deposition (PLD). The X-ray diffraction ( $2\theta$  and  $\Phi$ ) and TEM characterizations confirm that the films were grown epitaxially. The Cr<sub>2</sub>O<sub>3</sub>(0001) growth on YSZ(001) occurs with twin domains. There are four domains of Cr<sub>2</sub>O<sub>3</sub> with in-plane rotation of 30° or 150° from each other about the [0001] growth direction. The epitaxial relation between the layers is given as [001]Si || [001]YSZ || [0001]Cr<sub>2</sub>O<sub>3</sub> and [100]Si || [100]YSZ || [10 $\bar{1}$ 0]Cr<sub>2</sub>O<sub>3</sub> or [11 $\bar{2}$ 0]Cr<sub>2</sub>O<sub>3</sub>. Though the bulk Cr<sub>2</sub>O<sub>3</sub> is an antiferromagnetic with T<sub>N</sub> = 307 K, we found that the films exhibit ferromagnetic like hysteresis loops with high saturation and finite coercive field up to 400K. The thickness dependent magnetizations together with oxygen annealing results suggest that the ferromagnetism (FM) is due to oxygen related defects whose concentration is controlled by strain present in the films. The out-of-plane magnetic measurements on Cr<sub>2</sub>O<sub>3</sub>(0001) films showed magnetic behavior suggesting antiferromagnetic nature. This FM in addition to the intrinsic magneto-electric properties of Cr<sub>2</sub>O<sub>3</sub>, opens the door to relevant spintronics applications.

### 3.2 Introduction:

The transition metal sesqui oxide  $\text{Cr}_2\text{O}_3$  that crystallizes in the corundum structure with  $R\bar{3}c$  space group is an antiferromagnetic insulator below Néel temperature 307 K <sup>1,2</sup> and is also the first room temperature (RT) magneto electric material reported <sup>3,4</sup>. ME effect refers to the induction of magnetism by the application of an electric field (E) and vice versa <sup>5</sup>. The high insulating nature of  $\text{Cr}_2\text{O}_3$  makes it a suitable candidate to be employed as a tunnel barrier in magnetic tunnel junctions <sup>6</sup>. There is a revival of interest in  $\text{Cr}_2\text{O}_3$  because of the recent studies in multiferroics. Room temperature ferromagnetism (ferro electricity) has been observed in finite E (H) fields in bulk  $\text{Cr}_2\text{O}_3$  single crystal <sup>7</sup>. Isothermal electric control of exchange bias at RT has been realized in a system of  $\text{Cr}_2\text{O}_3$  in contact with a ferromagnetic film <sup>8</sup>. It is shown using spin polarized photoemission spectroscopy, first principles calculations and magnetometry that the (0001) surface of  $\text{Cr}_2\text{O}_3$  has a roughness-insensitive electrically switchable magnetization <sup>8</sup>. Spatially resolved magnetization domain structure has been observed on the (0001) surface of  $\text{Cr}_2\text{O}_3$  by electric field control <sup>9</sup>.

Although there are many reports in the literature on the thin film deposition of  $\text{Cr}_2\text{O}_3$ , most of them are related to the use of sapphire as a substrate because of the similarity in the crystal structure <sup>10-12</sup>, while some attempts have been made at depositing  $\text{Cr}_2\text{O}_3$  films on Si substrate <sup>13-15</sup>. Shiratsuchi *et al.*, report the integration of epitaxial  $\text{Cr}_2\text{O}_3(0001)$  films on Si(111) by using an Au(111) buffer layer <sup>16</sup>. However, no report has been made on the epitaxial growth of  $\text{Cr}_2\text{O}_3$  on Si(001). The recent theoretical predictions and experimental observations <sup>8</sup> demonstrating the capability of  $\text{Cr}_2\text{O}_3$  to be used in future advanced electronic devices indirectly necessitate its integration with Si(001), which is the mainstay substrate in

micro-electronics industry. It is difficult to grow  $\text{Cr}_2\text{O}_3$  directly on Si because of the amorphous native oxide present on it. This can be solved by choosing c-YSZ buffer layer that can be epitaxially grown on Si(001)<sup>17,18</sup>. The YSZ can chemically react and be able to remove the native oxide on Si. Once it removes the native oxide, the epitaxial growth of YSZ takes place due to the lattice matching between Si and c-YSZ (5.37%). In this letter, we report on the epitaxial growth of  $\text{Cr}_2\text{O}_3$  thin films integrated on Si(001) using epitaxial c-YSZ buffer layer by PLD technique. We present a detailed structural characterization of the grown films using XRD ( $2\theta$  and  $\Phi$ ), TEM and XPS. The in-plane magnetization results acquired from the samples show typical ferromagnetic behavior up to 400K. The ferromagnetic behavior in otherwise antiferromagnetic material is attributed to the oxygen related defects whose concentration is controlled by strain present in the films. The temperature variation of coercive field is following the well-known Bean and Livingston relation for an assembly of non-interacting single domain particle system. This room temperature ferromagnetism (RTFM) in magneto electric and antiferromagnetic  $\text{Cr}_2\text{O}_3$  is promising for the future non-volatile memory applications like spintronics.

### 3.3 Experimental Details:

The  $\text{Cr}_2\text{O}_3$ /YSZ thin films were grown epitaxially on Si(001) using pulsed laser deposition that utilized a KrF laser ( $\lambda=248$  nm,  $\tau=25$  ns). First, the YSZ buffer layer of 160 nm was grown at 600°C with a few initial pulses under  $1 \times 10^{-5}$  Torr vacuum and the remaining under  $5 \times 10^{-4}$  Torr  $\text{O}_2$ . The  $\text{Cr}_2\text{O}_3$  film was then deposited from the Cr target on the YSZ/Si that was held at 650°C under oxygen partial pressure of  $5 \times 10^{-2}$  Torr  $\text{O}_2$ . We found that the stoichiometry of the film can be controlled better by using metallic Cr target instead of oxide  $\text{Cr}_2\text{O}_3$ . The laser frequency was 5 Hz for both the cases whereas the fluency was 2.8

J/cm<sup>2</sup> for YSZ and 3.2 J/cm<sup>2</sup> for Cr<sub>2</sub>O<sub>3</sub>. The crystal structure of the films was studied using Rigaku X-ray diffractometer (2 $\theta$ -scans) and epitaxial relationships were determined from the  $\Phi$  scans using Panalytical X'Pert PRO MRD HR X-Ray Diffraction System. The JEOL 2010F TEM was used for imaging and estimation of the thicknesses of the layers. The chemical analysis for Cr<sub>2</sub>O<sub>3</sub> films was carried out using X-ray photoelectron spectrometer in SPECS FlexMod system equipped with an Al K $\alpha$  monochromatic x-ray source (1486.7eV). The magnetic properties were measured by applying magnetic field parallel to the Cr<sub>2</sub>O<sub>3</sub>(0001) surface, using Super-conducting Quantum Interference Device (SQUID).

### 3.4 Results and Discussion:

Figure 3.1 shows the typical XRD  $\theta$ -2 $\theta$  pattern of Cr<sub>2</sub>O<sub>3</sub>/YSZ/Si heterostructure. The presence of only (00 $l$ ) reflections corresponding to Cr<sub>2</sub>O<sub>3</sub>, YSZ and Si excludes the possibility of secondary phases and also confirms the textured growth of the films. The rocking curve ( $\omega$ -scan) for the (0006) plane of Cr<sub>2</sub>O<sub>3</sub> shown in the inset of Figure 3.1 gives a FWHM of 0.6 $^\circ$ , indicating a good crystallinity of the film. In order to confirm the epitaxial nature of the films and establish the epitaxial relationships, XRD  $\Phi$ -scan measurements were performed. Figure 3.2(a) shows the typical  $\Phi$ -scan for the heterostructure. The phi-scan is excited on the (111) planes which are inclined at 54.73 $^\circ$  from (001) plane for YSZ and Si and on (10 $\bar{1}$ 4) reflections, which are inclined at 38.24 $^\circ$  from (0006) plane for Cr<sub>2</sub>O<sub>3</sub>. The four-fold symmetry of YSZ(111) reflections coincident with those of Si(111) shows that the YSZ(002) grows on Si(001) with cube-on-cube geometry. The epitaxial nature of Cr<sub>2</sub>O<sub>3</sub> is evident from the twelve equi-spaced sharp peaks appearing in the  $\Phi$ -scan. The epitaxial growth of Cr<sub>2</sub>O<sub>3</sub> on YSZ can be understood in the paradigm of domain matching epitaxy<sup>19</sup>. The presence of twelve peaks, instead of three corresponding to 3-fold symmetry of the C-

axis indicates that there are four different in-plane domain variants with a single out-of-plane orientation. This is expected due to the growth of 3-fold symmetric  $\text{Cr}_2\text{O}_3(0001)$  on 4-fold symmetric  $\text{YSZ}(002)$ .

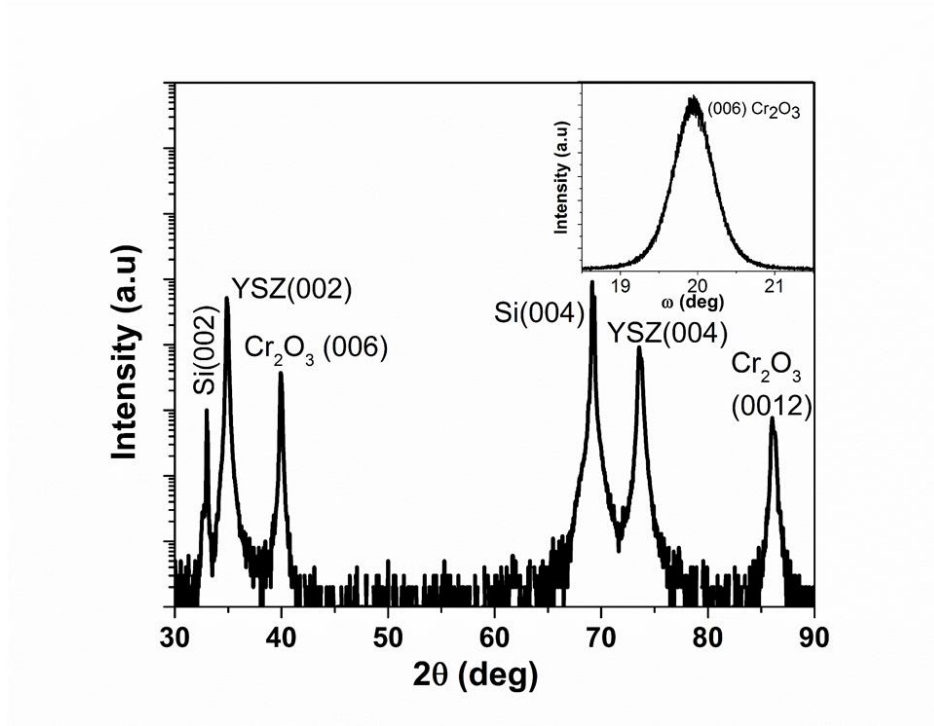


Figure 3.1: Typical XRD  $\theta$ - $2\theta$  pattern of  $\text{Cr}_2\text{O}_3/\text{YSZ}/\text{Si}(001)$  heterostructure. Inset:  $\omega$ -scan excited on (0006) peak of  $\text{Cr}_2\text{O}_3$ .

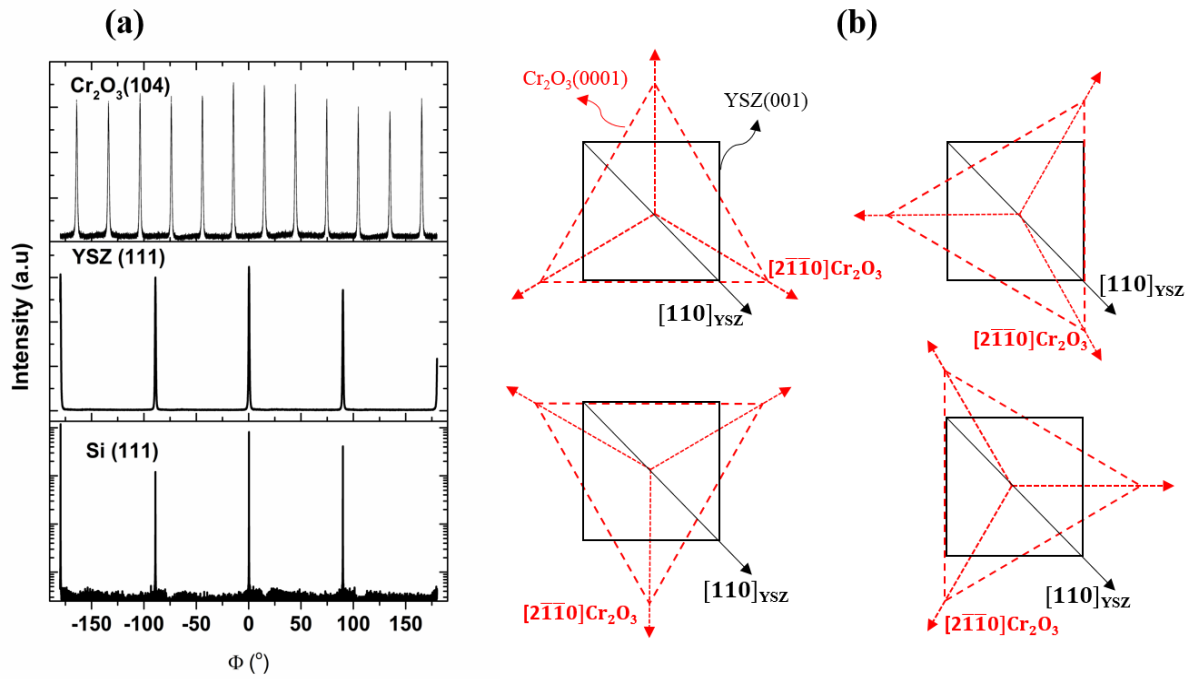


Figure 3.2: (a) Typical XRD  $\phi$  scan of  $\text{Cr}_2\text{O}_3/\text{YSZ}/\text{Si}(001)$  heterostructure. It was excited on  $(10\bar{1}4)$ ,  $(111)$  and  $(111)$  reflections of  $\text{Cr}_2\text{O}_3$ , YSZ, and Si, respectively. (b) Schematic arrangement of the alignment of four different in-plane domain variants of  $\text{Cr}_2\text{O}_3$  with YSZ unit cell planes across  $\text{Cr}_2\text{O}_3/\text{YSZ}$  interface.

It can be seen in Figure 3.2(a) that the intensity of all four domains is almost the same, implying that all domains are equally probable. The schematic showing the alignment of four different domain variants of  $\text{Cr}_2\text{O}_3$  on YSZ across the  $\text{YSZ}/\text{Cr}_2\text{O}_3$  interface is in Figure 3.2(b). The epitaxial relationships obtained from  $\Phi$ -scan data can be written as  $[001]\text{Si} \parallel [001]\text{YSZ} \parallel [0001]\text{Cr}_2\text{O}_3$  and  $[100]\text{Si} \parallel [100]\text{YSZ} \parallel [10\bar{1}0]\text{Cr}_2\text{O}_3(\text{or}) [11\bar{2}0]$  (or)  $[01\bar{1}0](\text{or}) [\bar{1}2\bar{1}0]\text{Cr}_2\text{O}_3$ . It can be seen from the schematic in Figure 3.2(b) that the lower  $\text{Cr}_2\text{O}_3$  domains are twin equivalent to the upper ones.

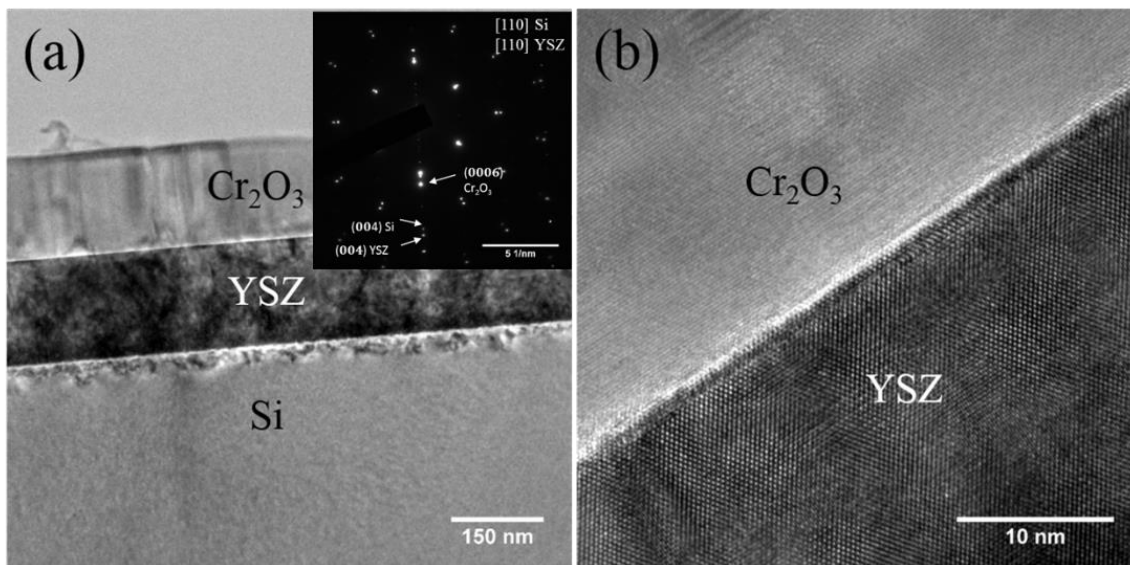


Figure 3.3: (a) Low magnification cross-sectional TEM image of  $\text{Cr}_2\text{O}_3/\text{YSZ}/\text{Si}(001)$  heterostructure. (b) HRTEM image of  $\text{Cr}_2\text{O}_3/\text{YSZ}$  interface. Inset of (a) shows the  $[110]$  zone axis SAED pattern acquired across the Si/YSZ interface.

We have performed TEM analysis to study the microstructure and further confirm the epitaxial nature of the films. The low magnification bright field cross sectional TEM image for  $\text{Cr}_2\text{O}_3/\text{YSZ}/\text{Si}$  heterostructure is shown in Figure 3.3(a). The growth rate of the  $\text{Cr}_2\text{O}_3$  thin film is estimated as  $0.4 \text{ \AA}^\circ$  per laser pulse. The interface between YSZ and  $\text{Cr}_2\text{O}_3$  is clean, sharp and reaction free, which can be seen in HRTEM image in Figure 3.3(b). To further confirm the epitaxial relations, we acquired SAED patterns for the heterostructure. The  $[110]$  SAED pattern acquired at the Si/YSZ interface is shown in the inset of Figure 3.3(a), which is in agreement with the  $\Phi$ -scan data. The SAED pattern for region covering only  $\text{Cr}_2\text{O}_3$  is shown in Figure 3.4. In order to determine the surface composition and valence state of Cr in our films, XPS measurements were performed. The survey spectrum shows peaks related to chromium, oxygen and some atmosphere carbon as shown in Figure 3.5. The high resolution XPS data collected (not shown here) for the Cr 2p core level peaks suggests that Cr is in +3

valence state. We did not observe any peaks corresponding to metallic and other valence states of Cr.

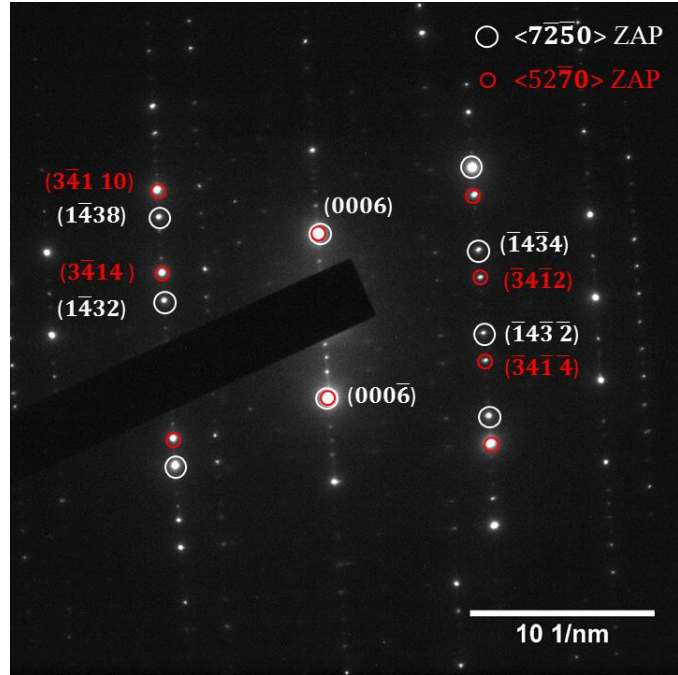


Figure 3.4: The SAED pattern acquired on  $\text{Cr}_2\text{O}_3$  thin film showing two patterns along  $\langle 7\bar{2}50 \rangle$  and  $\langle 52\bar{7}0 \rangle$  zone axes corresponding to two domains of  $\text{Cr}_2\text{O}_3$ .

The magnetic measurements, in all the cases, were performed by applying the magnetic field parallel to the (0001) plane of  $\text{Cr}_2\text{O}_3$ . The data collected from a 40 nm thick  $\text{Cr}_2\text{O}_3$  is displayed in the main panel of Figure 3.6(a). It shows the isothermal magnetic hysteresis (M-H) loops measured in the -10 KOe to +10 KOe field range at temperature ranging from 5K to 400K. The diamagnetic contribution from the substrate and the buffer layer has been subtracted. It can be seen that the loops exhibit saturation and finite coercive field at all the measured temperatures, indicating a typical ferromagnetic like behavior up to 400K.

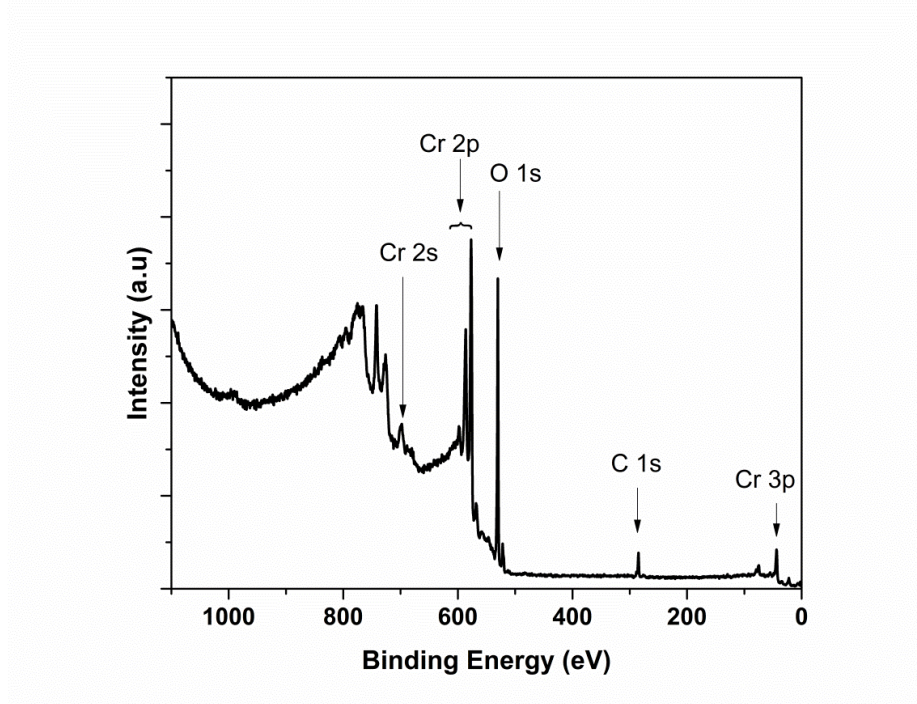


Figure 3.5: XPS survey spectrum of  $\text{Cr}_2\text{O}_3$  thin film, showing peaks corresponding to chromium, oxygen and some atmospheric carbon.

The field dependent magnetization at 300K starts to saturate around 5000 Oe, above which it is parallel to the field axis. The saturation magnetization ( $M_s$ ) and coercive field ( $H_c$ ) at 300K are 33 emu/cc and 75 Oe, respectively. Lower right inset of Figure 3.6(a) shows the enlarged view of the same. To identify the nature of ferromagnetism, the thermal variation of  $H_c$  extracted from M-H loops is plotted in the upper left inset of Figure 3.6(a). According to Bean and Livingston, the coercive field for an assembly of non-interacting single domain particles with uniaxial anisotropy follows the law  $H_c = H_0[1 - (T/T_B)^{1/2}]^{20}$ . Here  $T_B$  is the blocking temperature above which the particles become super-paramagnetic. It can be seen that  $H_c$  decreases linearly with the square root of temperature up to 300K, which is consistent with the above model. From this we may say that the contribution to FM is from single domain regions.

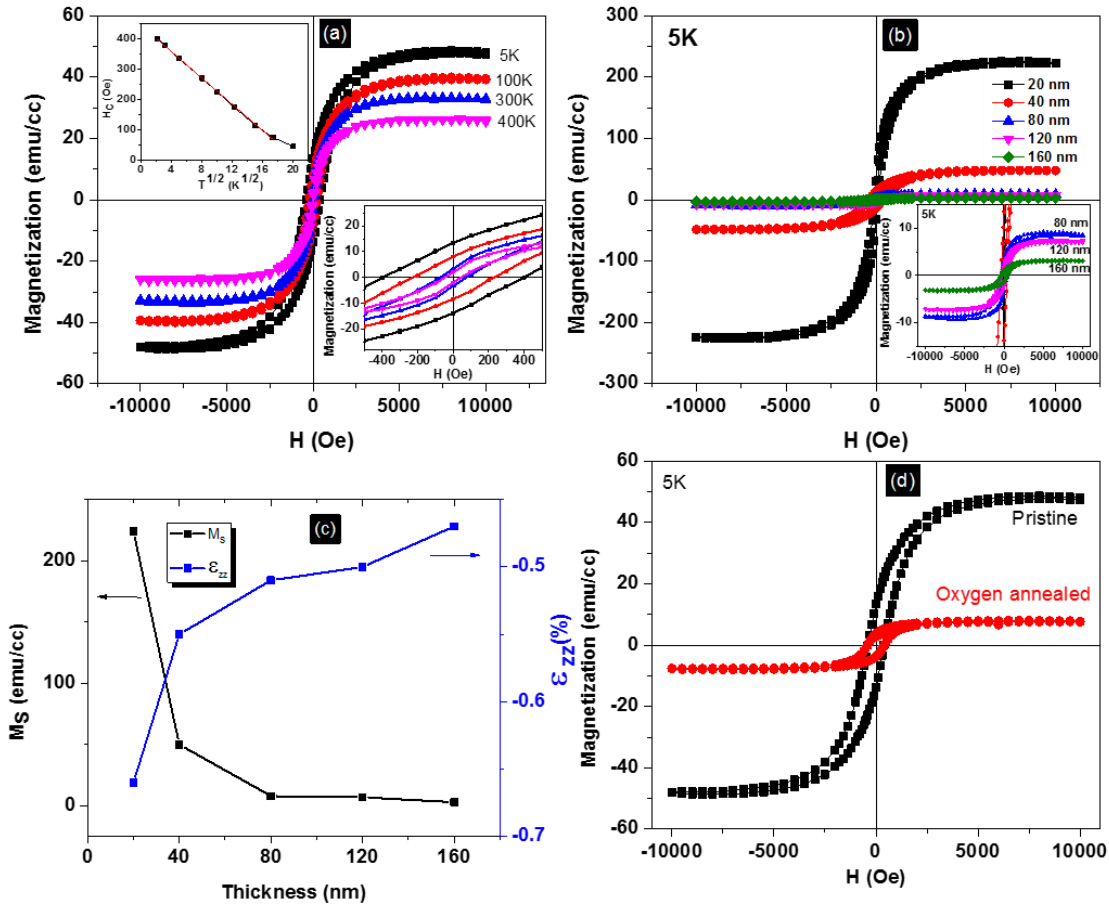


Figure 3.6: (a) Isothermal field dependent magnetization plots of 40 nm thick Cr<sub>2</sub>O<sub>3</sub> film ranging from 5K to 400K. Lower inset: Enlarged view of the same in the -500 Oe to +500 Oe field range. Upper inset: Plot of  $H_c$  vs  $T^{1/2}$  showing linear fit in the range 5K to 300K. (b) M-H loops acquired at 5K for Cr<sub>2</sub>O<sub>3</sub> films with thickness ranging from 20 to 160 nm. Inset shows the enlarged version of the same. (c) Thickness dependent saturation magnetization  $M_S$  and out-of-plane strain  $\epsilon_{zz}$  measured from XRD  $2\theta$  scans (d) M-H loops for 40 nm thick Cr<sub>2</sub>O<sub>3</sub> acquired at 5K for pristine and oxygen annealed samples. For all the magnetic measurements field was applied parallel to the (0001) surface of Cr<sub>2</sub>O<sub>3</sub>.

The  $T_B$  using the above fit is determined to be 415K. The M-H loops in Figure 3.6(a) and magnetization versus temperature data in Figure 3.7 indicate that the Curie temperature  $T_C$  is above 400K, which is well above the Néel temperature 307K of bulk Cr<sub>2</sub>O<sub>3</sub>.

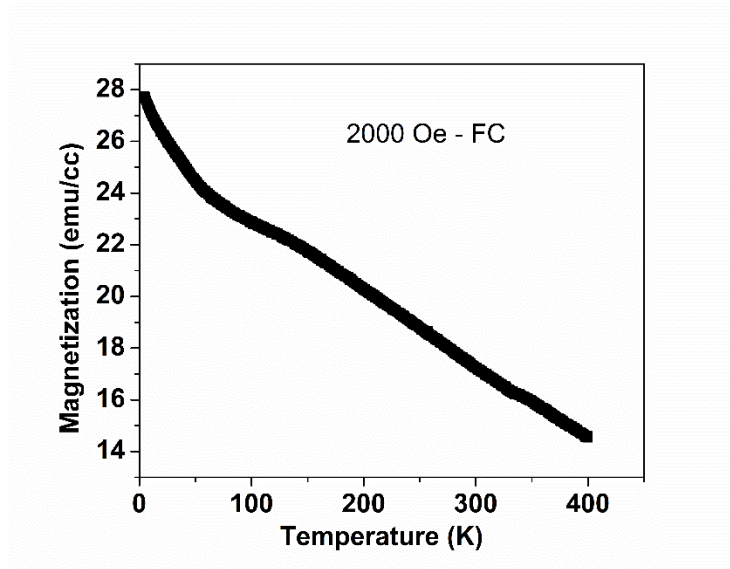


Figure 3.7: The magnetization versus temperature data measured on a 40nm thick  $\text{Cr}_2\text{O}_3$  film. The sample was cooled from 400K to 5K under an applied field of 2000 Oe and the data was collected during warming cycle with the same field.

The FM observed on the (0001) plane of  $\text{Cr}_2\text{O}_3$  is in contrast to what has been reported earlier in  $\text{Cr}_2\text{O}_3$  thin films<sup>21</sup>. In bulk single crystal  $\text{Cr}_2\text{O}_3$ , the  $\text{Cr}^{+3}$  spins are oriented along the *C*-axis (parallel and anti-parallel). In the absence of external field, the number of spin up's is equal to that in down direction and there will be no net magnetization. When a magnetic field is applied along the *C*-axis, it results in some net surface magnetization in the applied field direction. However, recently, there is a report on the observation of soft ferromagnetic behavior (in-plane) up to 315 K in poly/textured  $\text{Cr}_2\text{O}_3$  films grown on Au buffer layer, which was attributed to lattice misfit strain<sup>15</sup>. The  $\text{Cr}_2\text{O}_3/\text{YSZ}/\text{Si}$  sample in the present case shown high  $H_C$  and  $T_C$  compared to previous reports. In the literature, observation of FM in otherwise AFM materials in thin film or nano particles form has been widely reported<sup>22-24</sup>, attributed to domain boundaries, uniform spin canting and strain.

To identify whether the origin of FM in Cr<sub>2</sub>O<sub>3</sub> thin film is due to strain, we have grown films of various thicknesses ranging from 20 nm to 160 nm. The in-plane M-H loops acquired at 5K from the samples are plotted in Figure 3.6(b); inset shows the enlarged view of the same for 80, 120, 160 nm thick films. All of the above samples shown typical FM nature up to 400K. It can be clearly seen that M<sub>S</sub> is decreased with increasing thickness, indicating a strong effect of thickness on M<sub>S</sub>. The thickness dependent M<sub>S</sub> can be correlated with the strain present in the film. High resolution XRD 2θ-scans around the Cr<sub>2</sub>O<sub>3</sub>(006) peak were collected to determine the strain. The peak position is shifted towards lower 2θ values with increasing thickness of the film. It means that the out-of-plane lattice constant (C<sub>00P</sub>) is increased with increasing thickness, approaching bulk value for thicker films. The strain  $\epsilon_{zz}$  present along this direction can be found from  $\epsilon_{zz} = (C_{00P} - C_{\text{bulk}}) / C_{\text{bulk}}$ ; where C<sub>bulk</sub> is the bulk value of C (13.594 Å). The variation of  $\epsilon_{zz}$  and saturation magnetization (M<sub>S</sub>) with thickness is presented in Figure 3.6(c). It is evident from this plot that M<sub>S</sub> is maximum (minimum) when the magnitude of  $\epsilon_{zz}$  is maximum (minimum). The -ve sign for  $\epsilon_{zz}$  indicates a compressive strain. These results suggest that FM in Cr<sub>2</sub>O<sub>3</sub> is induced by strain. A similar thickness dependent magnetism was observed in BFO<sup>25</sup> and Co:ZnO<sup>26</sup> films. Strain in thin film systems has three sources: lattice misfit, thermal and defect induced. Defect-induced or oxygen vacancy induced ferromagnetism has been observed in some oxide materials like ZnO<sup>27</sup> and Sr<sub>3</sub>SnO films<sup>28</sup>. In order to identify whether the strain present in our films is due to defects, we have performed post O<sub>2</sub> annealing on the 40 nm thick sample at 100 Torr and 650°C for 3 h. It is well known that annealing in oxygen atmosphere improves the crystallinity of the film by reducing point defects such as oxygen vacancies and

hence relieving the strain. We found that  $M_s$  at 5K is reduced dramatically from 48 to 8 emu/cc after  $O_2$  annealing, as shown in Figure 3.6(d).

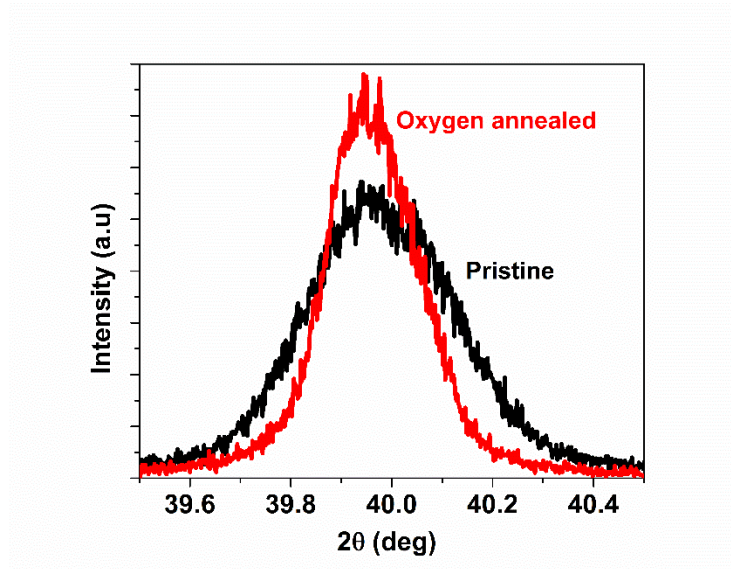


Figure 3.8: The XRD data collected around  $Cr_2O_3(0006)$  peak on a 40 nm thick  $Cr_2O_3$  film before and after oxygen annealing. The out-of-plane strain decreased from -0.55 % to -0.50% with oxygen annealing.

To confirm that crystal structure and phase of  $Cr_2O_3$  has not changed after annealing, we did XRD after oxygen annealing and found that the structure retained same. And there is a decrease in the out-of-plane lattice strain  $\epsilon_{zz}$  after oxygen annealing that can be seen from the shift of the  $Cr_2O_3(0006)$  peak position in Figure 3.8. Further, the XPS data excludes the presence of any magnetic impurities and supports that the observed magnetic moment can't be an impurity induced one. These results suggest that FM is mainly due to oxygen related defects whose concentration is controlled by strain present in the films.

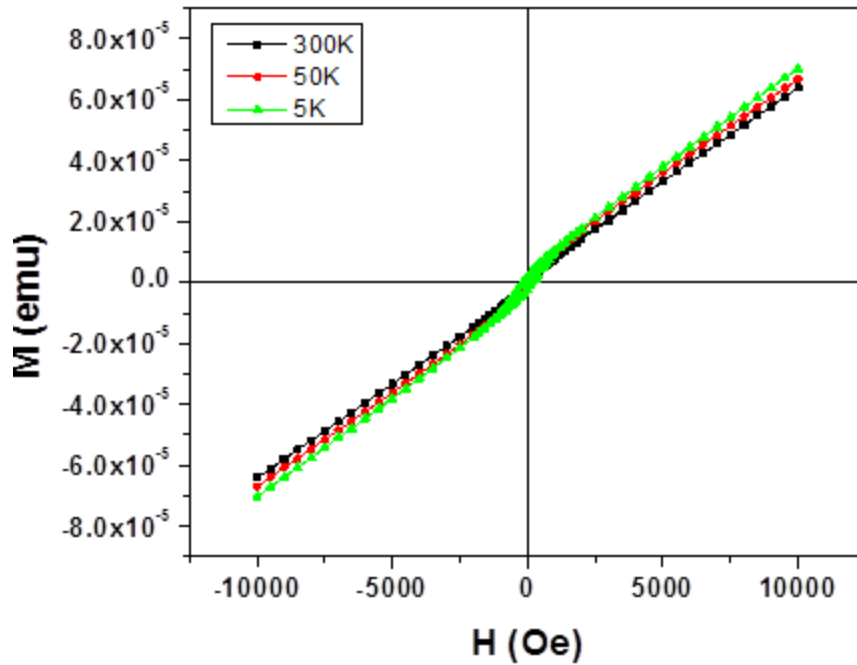


Figure 3.9: Isothermal field dependent magnetization plots of 40 nm thick  $\text{Cr}_2\text{O}_3$  film at temperatures 5K, 50K and 300K as denoted. The magnetic field was applied along the out-of-plane [0001] direction, which is the easy axis for antiferromagnetic  $\text{Cr}_2\text{O}_3$ .

In order to verify whether the  $\text{Cr}_2\text{O}_3$  thin films are showing antiferromagnetic nature or not, we have performed M-H hysteresis loop on oxygen annealed thin film of 40 nm with applied field along the out-of-plane [0001] direction, which is the easy axis for antiferromagnetic  $\text{Cr}_2\text{O}_3$ . As can be seen in Figure 3.9, there is a linear variation of magnetization with the applied field at all the temperatures except a small loop near the origin for 5K data. Similar linear unsaturated variation of M with H was observed in epitaxial  $\text{Cr}_2\text{O}_3(0001)$  thin films grown on  $\text{Al}_2\text{O}_3$  substrate. These results suggest antiferromagnetic nature of  $\text{Cr}_2\text{O}_3$  along the out-of-plane as expected.

### 3.5 Conclusions:

In conclusion, we have integrated epitaxial  $\text{Cr}_2\text{O}_3$  films on  $\text{Si}(001)$  substrate via YSZ buffer layer using pulsed laser deposition. The X-ray  $\Phi$ -scan and TEM confirmed the epitaxial nature of the films. The epitaxial relations can be written as  $(001)[100]\text{Si} \parallel (001)[100]\text{YSZ}$  and  $(001)[100]\text{YSZ} \parallel (0001)[10\bar{1}0]\text{Cr}_2\text{O}_3$  (or)  $(0001)[11\bar{2}0]\text{Cr}_2\text{O}_3$  (or)  $(0001)[01\bar{1}0]\text{Cr}_2\text{O}_3$  (or)  $(0001)[\bar{1}2\bar{1}0]\text{Cr}_2\text{O}_3$ . The in-plane magnetic measurements showed ferromagnetic behavior with high saturation magnetization and finite coercivity existing up to 400K. The magnetization is found to be a strong function of thickness, which is correlated with the residual strain present in films. The thickness dependent magnetizations together with oxygen annealing results suggest that the FM is due to oxygen related defects whose concentration is controlled by strain present in the films. The out-of-plane magnetic measurements on  $\text{Cr}_2\text{O}_3(0001)$  films showed magnetic behavior suggesting antiferromagnetic nature. The in-plane ferromagnetism in addition to the intrinsic magneto-electric properties of  $\text{Cr}_2\text{O}_3$  opens the door to relevant spintronics applications.

### 3.6 References:

1. T. Nagamiya, K. Yosida, and R. Kubo, *Adv. Phys.* **4**, 1 (1955).
2. T. R. McGuire, E. J. Scott and F. H. Grannis, *Phys. Rev.* **102**(4), 1000 (1956).
3. I. E. Dzyaloshinskii, *J. Exptl. Theoret. Phys. (U.S.S.R.)* **37**, 881 (1959) [translation: *Soviet Phys. —JETP* **10**, 628 (1960)].
4. D. N. Astrov, *J. Exptl. Theoret. Phys. (U. S.S.R.)* **38**, 984 (1960) [translation: *Soviet Phys. —JETP* **11**, 708 (1960)].
5. L. D. Landau and E. M. Lifshitz, *Electrodynamics of Continuous Media* (Addison-Wesley Publishing Company, Inc., Reading, Massachusetts, 1960), p. 119.
6. R. Cheng, C. N. Borca, N. Pilet, B. Xu, L. Yuan, B. Doudin, S. H. Liou, and P. A. Dowben, *Appl. Phys. Lett.* **81**, 2109 (2002).
7. A. Iyama and T. Kimura, *Phys. Rev. B* **87**, 180408(R) (2013).
8. X. He, Y. Wang, N. Wu, A. N. Caruso, E. Vescovo, K. D. Belashchenko, P. A. Dowben and C. Binek, *Nat. Mater.* **9**, 579 (2010).
9. N. Wu, X. He, A. L. Wysocki, U. Lanke, T. Komesu, K. D. Belashchenko, C. Binek, and P. A. Dowben, *Phys. Rev. Lett.* **106**, 087202 (2011).
10. J. wang, A. Gupta, T. M. Klein, *Thin Solid Films* **516**, 7366 (2008).
11. S-Y. Jeong, J-B. Lee, H. Na, and T-Y. Seong, *Thin Solid Films* **518**, 4813 (2010).
12. H. Mändar, T. Uustare, J. Aarik, A. Tarre, and A. Rosenthal, *Thin Solid Films* **515**, 4570 (2007).
13. T. Kosaka, S. Suzuki, M. Saito, Y. Waseda, E. Matsubara, K. Sadamori and E. Aoyagi, *Thin Solid Films* **289**, 74 (1996).
14. M. Shima, T. Tepper, and C. A. Ross, *J. Appl. Phys.* **91**, 7920 (2002).

15. A. Ghosh, K. Dey, S. Sabyasachi, A. Karmakar, S. Majumdar, and S. Giri, Appl. Phys. Lett. **103**, 052412 (2013).
16. Y. Shiratsuchi, T. Nakatani, S. Kawahara, and R. Nakatani, J. Appl. Phys. **106**, 033903 (2009).
17. D. K. Fork, D. B. Fenner, G. A. N. Connell, J. M. Phillips and T. H. Geballe, Appl. Phys. Lett. **57**, 1137 (1990).
18. Th. Matthee, J. Wecker, H. Behner, G. Friedl, O. Eibl and K. Samwer, Appl. Phys. Lett. **61**, 1240 (1992).
19. J. Narayan, and B.C. Larson, J. Appl. Phys. **93**, 278 (2003).
20. C. P. Bean and J. D. Livingston, J. App. Phys. **30**, 1208 (1959).
21. S. Sahoo and CH. Binek, Philos. Mag. Lett. **87**(3–4), 259 (2007).
22. C. Vázquez- Vázquez , M. Bañobre-López, M.A. López-Quintela, L. E. Hueso, and J. Rivas, J. Magn. Magn. Mater. **272-276**, 1547 (2004).
23. D. Li, Z. Han, J. G. Zheng, X. L. Wang, D. Y. Geng, J. Li, and Z. D. Zhang, J. App. Phys. **106**, 053913 (2009).
24. J.S. White, M. Bator, Y. Hu, H. Luetkens, J. Stahn, S. Capelli, S. Das, M. Döbeli, Th. Lippert, V.K. Malik, J. Martynczuk, A. Wokaun, M. Kenzelmann, Ch. Niedermayer and C.W. Schneider, Phys. Rev. Lett. **111**, 037201 (2013)
25. X. J. Liu, C. Song, F. Zeng, F. Pan, B. He and W. S. Yan, J. App. Phys. **103**, 093911 (2008)
26. J. Wang, J. B. Neaton, H. Zheng, V. Nagarajan, S. B. Ogale, B. Liu, D. Viehland, V. Vaithyanathan, D. G. Schlom, U. V. Waghmare, N. A. Spaldin, K. M. Rabe, M. Wuttig, and R. Ramesh, Science **299**, 1719 (2003)

27. S. Mal, S. Nori, C. Jin, J. Narayan, S. Nellutla, I. Smirnov and J. T. Prater, *J. App. Phys.* **108**, 073510 (2010)
28. Y.F. Lee, F. Wu, J. Narayan, and J. Schwartz, *MRS Comm.* **4**, 7 (2014).

# Chapter 4 Room temperature ferromagnetism in epitaxial $\text{Cr}_2\text{O}_3$ thin films grown on r-sapphire

Published in Journal of Applied Physics, Volume 117, 2015, 19390. doi: 10.1063/1.4921435

Sandhyarani Punugupati, Jagdish Narayan and Frank Hunte

*Department of Materials Science and Engineering, North Carolina State University, Raleigh, NC- 27695*

## 4.1 Abstract:

We report on the epitaxial growth and magnetic properties of  $\text{Cr}_2\text{O}_3$  thin films grown on r-sapphire substrate using pulsed laser deposition. The X-ray diffraction ( $2\theta$  and  $\Phi$ ) and TEM characterization confirm that the films are grown epitaxially. The r-plane (01 $\bar{1}2$ ) of  $\text{Cr}_2\text{O}_3$  grows on r-plane of sapphire. The epitaxial relations can be written as: [01 $\bar{1}2$ ]  $\text{Cr}_2\text{O}_3$   $\parallel$  [01 $\bar{1}2$ ]  $\text{Al}_2\text{O}_3$  (out-of-plane) and [ $\bar{1}\bar{1}20$ ]  $\text{Cr}_2\text{O}_3$   $\parallel$  [ $\bar{1}\bar{1}20$ ]  $\text{Al}_2\text{O}_3$  (in-plane). The as-deposited films showed ferromagnetic behavior up to 400K but ferromagnetism almost vanishes with oxygen annealing. The Raman spectroscopy data together with strain measurements using high resolution XRD indicate that ferromagnetism in r- $\text{Cr}_2\text{O}_3$  thin films is due to the strain caused by defects such as oxygen vacancies.

## 4.2 Introduction:

The sesqui oxide  $\text{Cr}_2\text{O}_3$  is an antiferromagnetic (AFM) insulator below the Néel temperature 307K. It crystallizes in the corundum structure with  $R\bar{3}c$  space group and belongs to  $\bar{3}'m'$  magnetic point group, with the easy axis of magnetization along the [0001] direction.  $\text{Cr}_2\text{O}_3$  has been used in a broad range of applications such as protective coatings on stainless steels <sup>1</sup>, as a catalyst <sup>2</sup> and as a solar thermal energy collector <sup>3</sup>. Since  $\text{Cr}_2\text{O}_3$  is a

very insulating material, it can also be used as a tunnel barrier in magnetic tunnel junctions <sup>4</sup>, <sup>5</sup>. It was the first compound in which the linear magnetoelectric (ME) effect was theoretically predicted <sup>6</sup> and experimentally observed <sup>7</sup>. The ME effect refers to the appearance of electric polarization by the application of magnetic field and *vice versa* <sup>8</sup>. Although ME effect is a well-studied phenomenon, recently there is a rejuvenation of interest in this area with the aim of use in technological applications like spintronics <sup>9,10</sup>. The ME effect of Cr<sub>2</sub>O<sub>3</sub> is exploited to alter the magnetization of a ferromagnetic (FM) layer that is exchange biased with the adjacent AFM <sup>11</sup>. Recently, electrically switchable exchange bias has been realized at room temperature in Cr<sub>2</sub>O<sub>3</sub> single crystal when in contact with a ferromagnetic film, utilizing an unconventional surface magnetism on the Cr<sub>2</sub>O<sub>3</sub>(0001) surface <sup>12,13</sup>.

So far, the magnetoelectric property of Cr<sub>2</sub>O<sub>3</sub> has been demonstrated only in single crystals <sup>12,14</sup>. Room temperature ferromagnetic (electric) hysteresis loops have been reported under external electric (magnetic) fields in Cr<sub>2</sub>O<sub>3</sub> single crystals. Since the net magnetic moment induced by applied electric field in ME Cr<sub>2</sub>O<sub>3</sub> is small <sup>14</sup>, it is interesting and useful to see whether magnetic moment can be induced by other means, for example, by defects in the present case. Though, many reports are available on the growth of Cr<sub>2</sub>O<sub>3</sub> thin films, using different techniques <sup>15-17</sup>, in-depth study of their magnetic properties is lacking. For device applications, a good understanding of the structure property correlation in thin films is required. With this aim, we prepared epitaxial thin films of Cr<sub>2</sub>O<sub>3</sub> on r-sapphire substrates and studied their magnetic properties using a SQUID magnetometer. Here, we report on the epitaxial growth and magnetic properties of Cr<sub>2</sub>O<sub>3</sub> thin films grown on single crystal r-sapphire (01 $\bar{1}$ 2) substrate by pulsed laser deposition. The as grown films are well characterized using high-resolution (HR) XRD (2 $\theta$ ,  $\Phi$ ), TEM and Raman spectroscopy. The

films are found to be epitaxial with good crystallinity, as evidenced from the XRD and TEM data. The in-plane SQUID measurements performed (5-400K) on the pristine samples revealed ferromagnetism with Curie temperature above 400K. After oxygen annealing, the FM is almost completely suppressed. The FM in the as deposited films is attributed to the strain present in the films as inferred from HR XRD and Raman measurements. The decrease of strain with oxygen annealing indicates that strain is due to point defects such as oxygen vacancies. This study to understanding the origin of FM in Cr<sub>2</sub>O<sub>3</sub> thin films is useful to better design the spintronic devices.

### 4.3 Experimental Details:

The Cr<sub>2</sub>O<sub>3</sub> thin films were grown on r-plane sapphire (Al<sub>2</sub>O<sub>3</sub>) substrates by ablating high purity Cr target in oxygen ambience using pulsed laser deposition (PLD). The substrates were vapor cleaned in trichloro-ethylene at 250°C and then ultrasonically cleaned by immersing in acetone and methanol each for 5 min. The PLD chamber utilized a KrF laser of 248 nm wavelength and 25 ns pulse duration. The laser energy density was kept at 3.2 J/cm<sup>2</sup> with a repetition rate of 5 Hz and the target to substrate distance was maintained at 4 cm during the deposition. The base pressure of the chamber before deposition was less than 1×10<sup>-6</sup> Torr. The thin film deposition was performed at a substrate temperature of 650°C and 5×10<sup>-2</sup> Torr oxygen partial pressure. The cooling was carried under the same oxygen partial pressure at 10°C/min to room temperature. The phase structure of the films was determined by X-ray diffraction  $\theta$ -2 $\theta$  scans using Rigaku X-ray diffractometer with Cu K $\alpha$  (0.154 nm) radiation. The in-plane orientation of the films was determined by  $\Phi$  scans using Panalytical X'Pert PRO MRD HR X-Ray Diffraction System. The JEOL 2010F TEM was used for imaging and determination of thicknesses of thin film layers. Selected area electron

diffraction (SAED) was taken to further confirm the epitaxial nature and establish the epitaxial relationship between the film and the substrate. The in-plane magnetic properties were measured using a Super-conducting Quantum Interference Device (SQUID). Raman spectra were taken using a Horiba Labram HR800 system using a 532 nm wavelength laser.

#### 4.4 Results and Discussion:

Figure 4.1(a) shows the indexed  $\theta$ - $2\theta$  X-ray diffraction pattern of a 230 nm thick  $\text{Cr}_2\text{O}_3$  film grown on  $\text{Al}_2\text{O}_3(01\bar{1}2)$  substrate. The presence of only reflections corresponding to the  $(01\bar{1}2)$  plane of  $\text{Cr}_2\text{O}_3$  and their higher orders indicate that the film was grown highly textured or epitaxial. It also eliminates the possibility of formation of other phases of chromium oxide within the detection limit of XRD measurements. The  $(01\bar{1}2)$  peak position of  $\text{Cr}_2\text{O}_3$  film at  $2\theta = 24.352$  (bulk value 24.494) indicates that the out-of-plane lattice constant is elongated compared to the bulk value with a tensile strain of 0.57 % along that axis. The rocking curve ( $\omega$ -scan) taken on the  $(01\bar{1}2)$  plane shown in Figure 4.1(b) measures a full width at half maximum (FWHM) of  $0.8^\circ$ , indicating good crystallinity of the film. The XRD  $\phi$ -scan measurements were performed to identify the epitaxial nature of the film and establish the epitaxial relationship between the film and substrate. Figure 4.2 shows the  $\Phi$ -scan excited on the  $(006)$  plane of the film and substrate, inclined at  $\psi = 57.61^\circ$  from the  $(01\bar{1}2)$  plane. It should be noted that both  $\text{Cr}_2\text{O}_3$  and  $\text{Al}_2\text{O}_3$  crystallize in the corundum structure. The presence of a single peak at the same  $\Phi$ -position as the substrate peak indicates that the r-plane of the film has grown epitaxially without any rotation in the basal plane. The epitaxial relations are determined as  $[01\bar{1}2] \text{Cr}_2\text{O}_3 \parallel [01\bar{1}2] \text{Al}_2\text{O}_3$  (out-of-plane) and  $[\bar{1}\bar{1}20]\text{Cr}_2\text{O}_3 \parallel [\bar{1}\bar{1}20]\text{Al}_2\text{O}_3$  (in-plane).

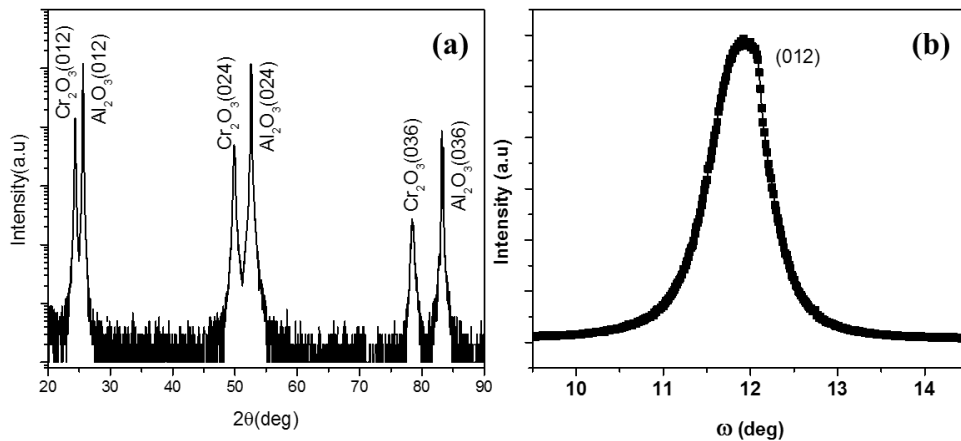


Figure 4.1: XRD (a)  $\theta$ - $2\theta$  scan, (b)  $\omega$  scan of  $\text{Cr}_2\text{O}_3/\text{Al}_2\text{O}_3$  heterostructure when  $\text{Cr}_2\text{O}_3$  was grown at  $650^\circ\text{C}$  substrate temperature and  $5 \times 10^{-2}$  Torr oxygen partial pressure.

Figure 4.3(a) shows the indexed SAED pattern acquired along the  $[2\bar{2}01]$  zone axis of the  $\text{Cr}_2\text{O}_3/\text{Al}_2\text{O}_3$  heterostructure. The spot pattern confirms that the film was grown epitaxially. The SAED pattern also excludes the formation of any other oxide phases of chromium. The epitaxial relations obtained from the data are in agreement with those obtained from the XRD  $\Phi$ -scan data. The inset of Figure 4.3(a) shows the low magnification cross sectional TEM image of the heterostructure. It can be seen from the HRTEM image in the Figure 4.3(b) that the interface between the film and the substrate is atomically clean, reaction free and so indicating that there is no secondary phase formation at the interface.

The magnetic field dependent magnetization (M vs H) loops measured in the -10 kOe to +10 kOe range on a 230 nm thick film are plotted in Figure 4.4(a). To make sure that the magnetism is originating from the film instead of the substrate, we have performed measurements on the substrate and subtracted the diamagnetic contribution from the substrate. The film displayed typical ferromagnetic behavior in the measurement

temperatures ranging from 5K to 400K, as seen in Figure 4.4(a). Figure 4.4(b) shows the enlarged view of the same in the -300 Oe to +300 Oe range. The hysteresis loops show finite coercivity that has decreased from 173 Oe at 5K to 17 Oe at 400K. The room temperature saturation magnetization ( $M_S$ ) and coercivity are 0.12 emu/g and 25 Oe, respectively. The magnetic moment observed here is very small compared to that reported in Cu doped ZnO<sup>18</sup> and Co doped CeO<sub>2</sub><sup>19</sup>. The variation of  $M_S$  with the temperature is plotted in Figure 4.4(c). The  $M_S$  is not a strong function of temperature in the measurement range of 5K to 400K, which implies that the FM in this case could be induced by defects. In Cr<sub>2</sub>O<sub>3</sub>, the spin axis is along the c-axis with the Cr<sup>+3</sup> spins aligned parallel and antiparallel to the c-axis.

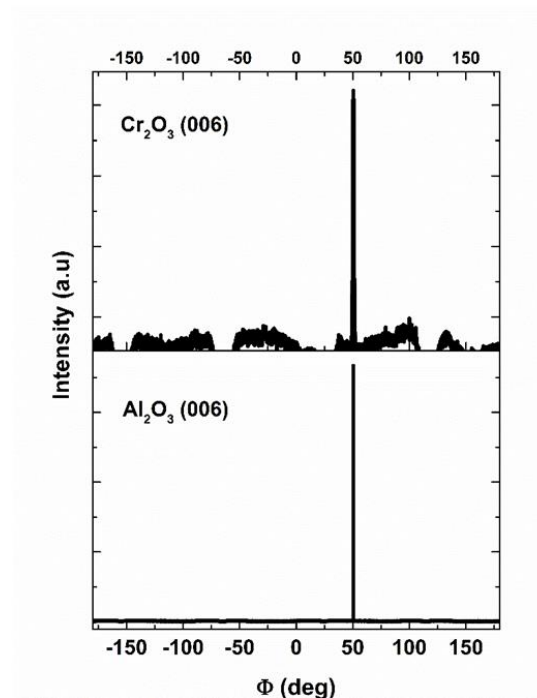


Figure 4.2: The  $\phi$ -scans of Cr<sub>2</sub>O<sub>3</sub>/Al<sub>2</sub>O<sub>3</sub> heterostructure excited on the (006) plane of the film and substrate, which is inclined at 57.61° from (01 $\bar{1}$ 2).

It is shown, using first-principles calculations and magnetometry, that the surface of c-plane of Cr<sub>2</sub>O<sub>3</sub> has electrically switchable magnetization with orientation perpendicular to the

plane. Based on the spin configuration, the r-plane should not exhibit any FM behavior. However, FM in otherwise AFM or non-magnetic materials has been well reported in the literature with reasons including strain and defects<sup>20-22</sup>.

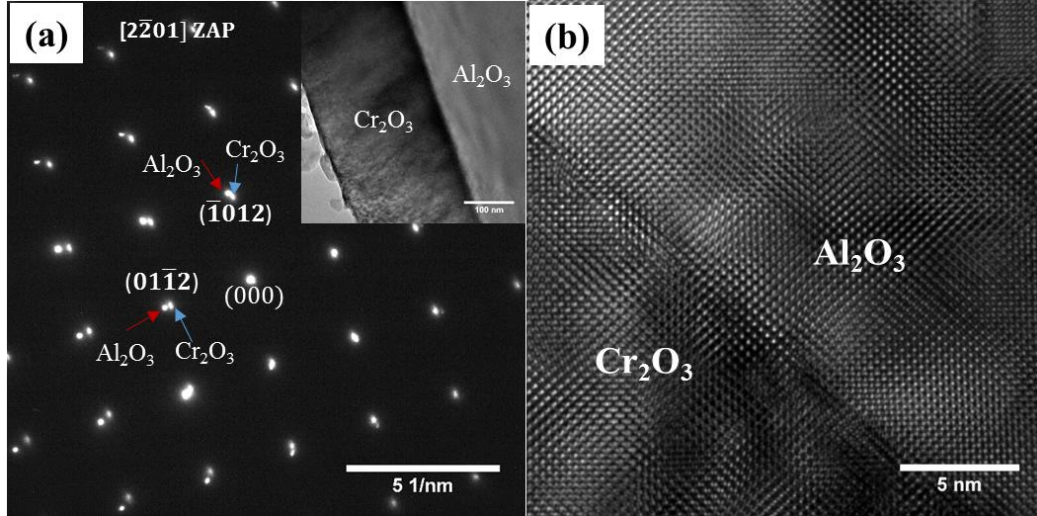


Figure 4.3: (a) Indexed  $[2\bar{2}01]$  SAED pattern acquired across  $\text{Cr}_2\text{O}_3/\text{Al}_2\text{O}_3$  thin film heterostructure. Inset: low magnification image of the same. (b) HRTEM image of the heterostructure showing clean and sharp interface.

To investigate the origin of FM in our films, we have performed post oxygen annealing (OA) on the sample at  $650^\circ\text{C}$  for 1hr at 5 Torr partial pressure of  $\text{O}_2$ . Figure 4.4(d) shows the effect of OA on the magnetic hysteresis loop measured at 300K. It can be seen from the graph that the magnetic moment (0.01 emu/g) almost vanishes with OA. The M vs T data collected from the sample before and after OA can be seen in Fig. S2. This data suggests that oxygen vacancies are the reason for the observed FM in our pristine films and, filling the vacancies reduces the FM order. In order to determine whether the crystal structure has changed after the OA, we performed XRD on the sample and found that it remained the same. The plot in Figure 4.5(a) shows the high-resolution  $2\theta$ -scan measured around the (012) peak of the

pristine and OA sample. It can be clearly seen that the peak position shifted towards higher  $2\theta$  values (towards the bulk value of  $24.494^\circ$ ) after OA. The pristine  $r\text{-Cr}_2\text{O}_3$  film is found to have +0.57% strain in the out-of-plane direction, which is decreased to +0.31% after OA. The residual in-plane strain  $\epsilon_{xx}$  (or)  $\epsilon_{yy}$  calculated using the relation  $\epsilon_{zz} = -2\nu*\epsilon_{xx}/(1-\nu)$  is about -0.85 % for pristine and -0.46 % for oxygen annealed sample, using the poisson's ratio  $\nu = 0.25$ .

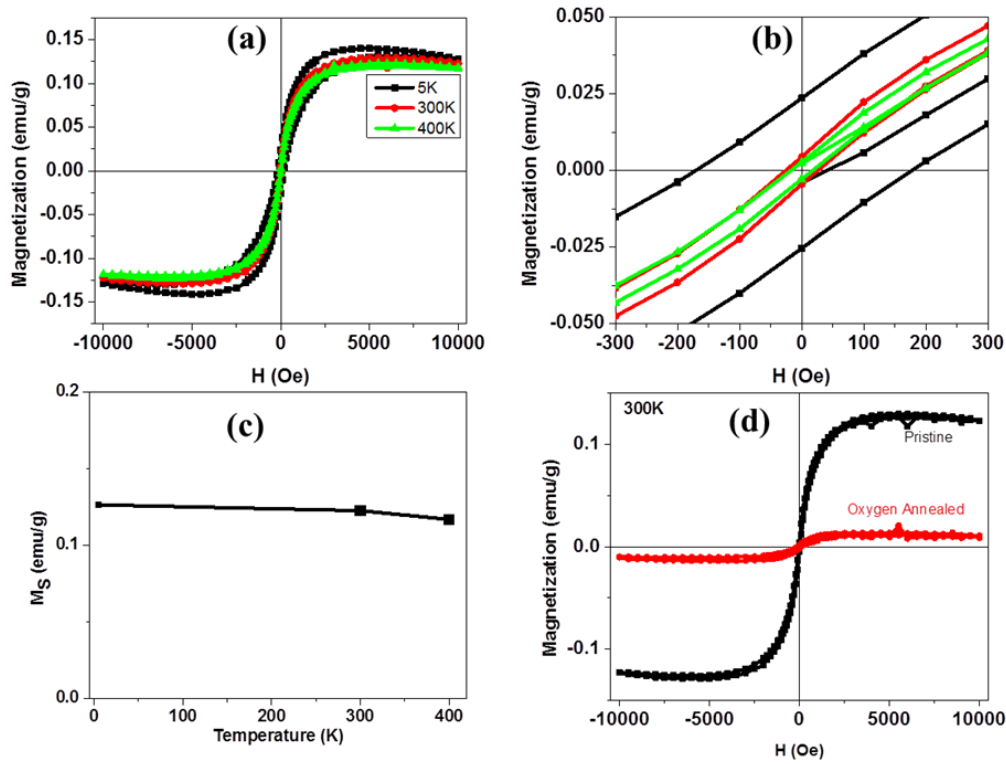


Figure 4.4: (a) Isothermal magnetic field dependent magnetization loops of 230 nm thick  $\text{Cr}_2\text{O}_3$  film measured at 5K, 300K and 400K. (b) Enlarged view of the same. (c) Saturation magnetization variation with temperature. (d) M vs H loops measured at 300K for the pristine and oxygen annealed samples. The magnetic field is applied in the  $r$ -plane of  $\text{Cr}_2\text{O}_3$ .

To further confirm that OA is decreasing the amount of strain present in the films, we have measured Raman spectra at room temperature on the pristine and OA samples. The Raman

vibrations are very sensitive to the amount of stress present in the films thus giving the Raman shift, which is a direct evidence for the presence of strain in the films. For  $\text{Cr}_2\text{O}_3$ , the vibrations with symmetry  $A_{1g}$  and  $E_g$  are Raman active. Out of the seven active modes ( $2A_{1g}+5E_g$ ), one  $A_{1g}$  and four  $E_g$  are usually observed. The most intense peak corresponds to  $A_{1g}$  mode (out-of-plane vibration) and can be used for strain estimation<sup>23, 24</sup>. It is evident from the graphs in Figure 4.5(b) that, with the OA, the  $A_{1g}$  mode for the pristine sample at  $561.6 \text{ cm}^{-1}$  is shifted to  $558.6 \text{ cm}^{-1}$  approaching bulk value of  $552 \text{ cm}^{-1}$ . The change in the peak position of  $A_{1g}$  can be written as  $\Delta\omega = \omega_{\text{stressed}} - \omega_{\text{bulk}}$ . The strain is tensile when  $\Delta\omega$  is negative and compressive when  $\Delta\omega$  is positive. We found a  $\Delta\omega$  of  $-9.6 \text{ cm}^{-1}$  for the pristine and  $-6.6 \text{ cm}^{-1}$  for the OA sample, indicating that the strain is tensile and also decreased with the OA. Thus the results from Raman measurements are in good qualitative agreement with those obtained from XRD. From these results we can conclude that FM is induced by the strain due to defects such as oxygen vacancies.

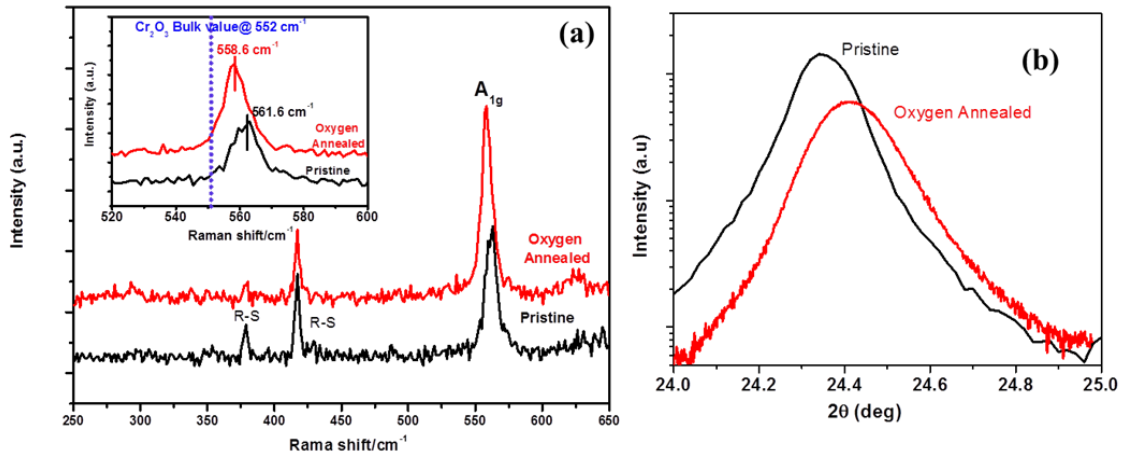


Figure 4.5: (a) Raman spectra collected on the pristine and oxygen annealed sample. Inset: Enlarged view of  $A_{1g}$  peak. (b) High resolution XRD  $2\theta$  scan acquired on the (012) peak of pristine and oxygen annealed sample.

Defects play a critical role in controlling the physical properties of the material. For instance, defect induced FM in otherwise nonmagnetic and un-doped oxides like TiO<sub>2</sub>, ZnO and SnO<sub>2</sub>, is widely reported in the literature often attributed to point defects such as oxygen vacancies, cation vacancies and cation interstitials <sup>25-28</sup>. In ZnO, it is shown that room temperature ferromagnetism (RTFM) can be created by a controlled introduction of Zn vacancies, where magnetic coupling is provided by carriers from oxygen vacancy and Zn interstitial clusters <sup>29</sup>. In PLD grown HfO<sub>2</sub> films, highly anisotropic FM was induced by defects <sup>22</sup>. A review of FM in various oxide systems is made recently <sup>30</sup>. Since defect generation is controlled by strain, strain engineering can be used to tune magnetic properties in thin films. Strain induced FM and Néel temperature change in AFMs has been demonstrated theoretically and experimentally in previous studies <sup>31-33</sup>.

Strain induced FM in many systems in the form of thin films and nanoparticles, is well reported in the literature. A tensile uniaxial strain of the order of 2%, in AFM thin films of LaMnO<sub>3</sub>, is found to change the orbital state and magnetic ground state significantly <sup>31</sup>. The epitaxial growth of Cr<sub>2</sub>O<sub>3</sub> on sapphire occurs via lattice matching epitaxy with a misfit strain of -4%. In thin films there are three different sources of strain; lattice, thermal mismatch and defect induced. In our case, when the thickness of the film is about 230 nm, most of the lattice misfit strain relaxes through the generation of dislocations and the contribution of thermal mismatch is very small. The residual strain in our pristine sample, which is experimentally observed to be +0.57%, could be mostly due to defects such as oxygen vacancies and related point defects. Under near equilibrium growth conditions, Cr<sub>2</sub>O<sub>3</sub> has no specific type of point defects, whereas oxygen partial pressure determines the type of defects. When Cr<sub>2</sub>O<sub>3</sub> is grown under a partial pressure of  $5 \times 10^{-2}$  Torr O<sub>2</sub>, we expect some

oxygen deficiency in the films and thus defect induced strain. When the sample is annealed in oxygen ambient, most of the oxygen vacancies are diffused out and thus reducing the amount of strain in the film. It is well known that antiferromagnets are piezo magnetics and strain induces magnetic moment. Recently it is found from theoretical studies that the two unpaired electrons due to oxygen vacancy are localized on the surrounding Cr atoms and hence enhancing the magnetic moment of the Cr atoms surrounding the oxygen vacancy <sup>34</sup>. We speculate that in addition to the increased magnetic moment of the Cr atoms surrounding the oxygen vacancy, the local compressive strain is inducing a canting of the magnetic moments away from the c-axis towards the r-plane and hence resulting in RTFM in the r-plane of Cr<sub>2</sub>O<sub>3</sub>. It should be noted that the angle between the r-axis and the c-axis in bulk Cr<sub>2</sub>O<sub>3</sub> crystal is 57.61° and r-axis is perpendicular to r-plane. To get a clear understanding of the origin of RTFM in r-plane Cr<sub>2</sub>O<sub>3</sub>, more advanced experimental and theoretical studies are required.

#### 4.5 Conclusions:

We have investigated RTFM in epitaxially grown Cr<sub>2</sub>O<sub>3</sub> thin films on r-sapphire by using PLD. The XRD ( $2\theta$  and  $\Phi$ ) and TEM data confirm that the films are grown epitaxially with the underlying sapphire substrate. Further TEM study indicated that there is no secondary phase formation in the film and also the interface between the substrate and film is clean and sharp. The epitaxial relations between the substrate and film were established as  $[01\bar{1}2] \text{ Cr}_2\text{O}_3 \parallel [01\bar{1}2] \text{ Al}_2\text{O}_3$  (out-of-plane) and  $[\bar{1}\bar{1}20] \text{ Cr}_2\text{O}_3 \parallel [\bar{1}\bar{1}20] \text{ Al}_2\text{O}_3$  (in-plane). The as deposited films exhibited ferromagnetic nature with Curie temperature above 400K. The room temperature coercivity and saturation magnetization are 25 Oe and 0.12 emu/g, respectively. The ferromagnetic nature almost vanished after oxygen annealing. The high

resolution XRD and Raman measurements indicate that the pristine films are strained, and the strain was reduced by oxygen annealing. The FM nature in the pristine films is attributed to strain induced defects such as oxygen vacancies.

#### 4.6References:

1. A. S. Cao, M. F. Doerner, V. J. Novotny, *J. Appl. Phys.* **66**, 5315 (1989).
2. P. S. Robbert, H. Geisler, C. A. Ventrice, J. van Ek, S. Chaturvedi, J. A. Rodriguez, M. Kuhn, U. Diebold, *J. Vac. Sci. Technol. A* **16**, 990 (1998).
3. V. Teixeira, E. Sousa, M.F. Costa, C. Nunes, L. Rosa, M. J. Carvalho, M. Collares-Pereira, E. Roman, J. Gago, *Thin Solid Films* **392**, 320 (2001).
4. A. M. Bratkovsky, *Phys. Rev. B* **56**, 2344 (1997).
5. R. Cheng, C. N. Borca, N. Pilet, B. Xu, L. Yuan, B. Doudin, S. H. Liou, and P. A. Dowben, *Appl. Phys. Lett.* **81**, 2109 (2002).
6. I. E. Dzyaloshinskii, *J. Exptl. Theoret. Phys. (U.S.S.R.)* **37**, 881 (1959) [*Soviet Phys. —JETP* **10**, 628 (1960)].
7. D. N. Astrov, *J. Exptl. Theoret. Phys. (U. S.S.R.)* **38**, 984 (1960) [*Soviet Phys. —JETP* **11**, 708 (1960)].
8. L. D. Landau and E. M. Lifshitz, *Electrodynamics of Continuous Media* (Addison-Wesley Publishing Company, Inc., Reading, Massachusetts, 1960), p. 119.
9. W. Eerenstein, N. D. Mathur and J. F. Scott, *Nature* **442**, 759 (2006).
10. M. Fiebig, *J. Phys. D* **38**, R123 (2005).
11. P. Borisov, A. Hochstrat, X. Chen, W. Kleemann, and C. Binek, *Phys. Rev. Lett.* **94**, 117203 (2005).
12. X. He, Y. Wang, N. Wu, A. N. Caruso, E. Vescovo, K. D. Belashchenko, P. A. Dowben and C. Binek, *Nat. Mater.* **9**, 579 (2010).
13. N. Wu, X. He, A. L. Wysocki, U. Lanke, T. Komesu, K. D. Belashchenko, C. Binek, and P. A. Dowben, *Phys. Rev. Lett.* **106**, 087202 (2011).

14. A. Iyama and T. Kimura, *Phys. Rev. B* **87**, 180408(R) (2013).
15. S-Y. Jeong, J-B. Lee, H. Na, and T-Y. Seong, *Thin Solid Films* **518**, 4813 (2010).
16. H. Mändar, T. Uustare, J. Aarik, A. Tarre, and A. Rosenthal, *Thin Solid Films* **515**, 4570 (2007).
17. J. Wang, A. Gupta, T. M. Klein, *Thin Solid Films* **516**, 7366 (2008).
18. A. Tiwari, M. Snure, D. Kumar, and J. T. Abiade, *Appl. Phys. Lett* **92**, 062509 (2008).
19. A. Tiwari, V. M. Bhosle, S. Ramachandran, N. Sudhakar, J. Narayan, S. Budak, and A. Gupta, *Appl. Phys. Lett.* **88**, 142511 (2006).
20. D. Rubi, C. de Graaf, C. J. M. Daumont, D. Mannix, R. Broer, and B. Nohedal, *Phys. Rev. B* **79**, 014416 (2009).
21. S. Punugupati, J. Narayan, and F. Hunte, *Appl. Phys. Lett.* **105**, 132401 (2014).
22. J. M. D. Coey, M. Venkatesan, P. Stamenov, C. B. Fitzgerald, and L. S. Dorneles, *Phys. Rev. B* **72**, 024450 (2005).
23. J. Birnie, C. Craggs, D. J. Gardinier, and P. R. Graves, *Corros. Sci.* **33**, 1, (1992).
24. J. Mougín, T. Le Bihan, and G. Lucazeau, *J. Phys. Chem. Solids* **62**, 553, (2001).
25. S. D. Yoon, Y. Chen, A. Yang, T. L. Goodrich, X. Zuo, D. A. Arena, K. Ziemer, C. Vittoria and V. G. Harris, *J. Phys.: Condens. Matter* **18**, L355 (2006).
26. S. Mal, S. Nori, C. Jin, J. Narayan, S. Nellutla, I. Smirnov and J. T. Prater, *J. App. Phys.* **108**, 073510 (2010).
27. M. Khalid, M. Ziese, A. Setzer, P. Esquinazi, M. Lorenz, H. Hochmuth, M. Grundmann, D. Spemann, T. Butz, *Phys. Rev. B* **80**, 035331 (2009).
28. N. H. Hong, N. Poirot, and J. Sakai, *Phys. Rev. B* **77**, 033205 (2008).

29. S. Mal, T-H. Yang, P. Gupta, J. T. Prater, and J. Narayan, *Acta Mater.* **59**, 2526 (2011).
30. M. C. Prestgard , G. P. Siegel , A. Tiwari, *Adv. Mat. Lett.* **5(5)**, 242 (2014)
31. K. H. Ahna, A. J. Millis, *Physica B* **312–313**, 766 (2002).
32. Y. Kota, H. Imamura, and M. Sasaki, *Appl. Phys. Express* **6**, 113007 (2013).
33. K. H. Wu, H.-J. Chen, C. C. Hsieh, C.W. Luo, T. M. Uen, J.-Y. Lin, J. Y. Juang, *J Supercond Nov Magn.* **26**, 801 (2013).
34. F. Lebreau, M. M. Islam, B. Diawara, and P. Marcus, *J. Phys. Chem. C* **118**, 18133 (2014).

# Chapter 5 Growth, magnetic and magnetotransport properties of bi-epitaxial $\text{La}_{0.7}\text{Sr}_{0.3}\text{MnO}_3(110)$ thin films integrated on $\text{Si}(001)$

## 5.1 Abstract:

We report the growth of bi-epitaxial  $\text{La}_{0.7}\text{Sr}_{0.3}\text{MnO}_3(110)$  thin films integrated on  $\text{Si}(100)$  substrate with cubic yttria stabilized zirconia (c-YSZ)/ $\text{SrTiO}_3$  (STO) buffer layers by pulsed laser deposition. The  $\text{La}_{0.7}\text{Sr}_{0.3}\text{MnO}_3$  and STO thin films were grown with a single  $[110]$  out-of-plane orientation and with two in-plane domain variants, which is confirmed by XRD and TEM study. The bi-epitaxial growth of STO on c-YSZ can be explained by the paradigm of domain matching epitaxy. The epitaxial relationship between STO and c-YSZ can be written as  $[110](001)\text{ c-YSZ} \parallel [\bar{1}\bar{1}\bar{1}](110)\text{ STO}$  (or)  $[110](001)\text{ c-YSZ} \parallel [\bar{1}\bar{1}\bar{2}](110)\text{ STO}$ . The  $\text{La}_{0.7}\text{Sr}_{0.3}\text{MnO}_3$  thin films are ferromagnetic with Curie temperature 324K and showed metal to insulator transition at 285K. The  $\text{La}_{0.7}\text{Sr}_{0.3}\text{MnO}_3$  thin films showed hysteresis loops in magnetoresistance when magnetic field is applied in both in-plane  $(110)$  and out-of-plane  $[110]$  directions. The highest magnetoresistance obtained in this study is -32% at 50K and 50 kOe for in-plane configuration whereas the room temperature magnetoresistance is -4% at 10 kOe and -17% at 50 kOe. The hysteresis in the magnetoresistance and the controlled domain boundaries in bi-epitaxial  $\text{La}_{0.7}\text{Sr}_{0.3}\text{MnO}_3$  films integrated on Si can offer significant advantages over the polycrystalline counterparts.

## 5.2 Introduction:

The doped manganese perovskites of the type  $\text{La}_{1-x}\text{Sr}_x\text{MnO}_3$  have attracted great deal of attention due to their rich physics and fascinating magnetoresistance (MR) properties <sup>[1-3]</sup>. They are potential candidates to be used in the emerging technological applications such as magnetic read heads, magnetic resistance memory and other novel spintronic devices. In particular, the  $\text{La}_{0.7}\text{Sr}_{0.3}\text{MnO}_3$  (LSMO) is a hole doped half metal with a Curie temperature ( $T_C \sim 360\text{K}$ ) above room temperature. In LSMO and other manganites, huge MR, called colossal magnetoresistance (CMR) is observed close to  $T_C$  but at very high magnetic fields <sup>[4-6]</sup>. For device applications, the MR should be achieved at low fields and at or above room temperature. Following the observation of extrinsic low field magnetoresistance (LFMR) in polycrystalline bulk materials <sup>[7, 8]</sup> and thin films <sup>[9-11]</sup>, which possess natural grain boundaries, efforts are made to improve LFMR by introducing artificial grain boundaries. Nanocomposite films of LSMO with secondary phases such as  $\text{ZnO}$  <sup>[12-14]</sup>,  $\text{BaTiO}_3$  <sup>[15]</sup>, and  $\text{NiO}$  <sup>[16]</sup> have been investigated for this purpose. We have introduced bi-epitaxial films (or epitaxial films with domain boundaries in this study to achieve LFMR in a controlled way. Compared to the grain boundaries in polycrystalline and nanocomposite thin films, the domain boundaries in these films are well characterized having a fixed orientation relationship between the domains. Since boundaries play a significant role in controlling the transport properties, understanding their effect on transport properties can be useful to better design the devices for practical applications. The intrinsic CMR effect in manganite epitaxial films is explained by a theory which combines the John-Teller effect and double exchange mechanism <sup>[3, 17, 18]</sup>. In contrast, the extrinsic LFMR in polycrystalline and nano composite thin films is explained by spin-polarized tunneling <sup>[7, 19]</sup> or spin-dependent scattering at the

grain boundaries <sup>[10, 20]</sup>. Though, Ramesh group has reported the effect of in-plane domains on the MR <sup>[21]</sup>, the LSMO in their case was integrated on MgO substrate and also detailed magneto-transport properties study in such films is lacking.

On the other hand, integration of perovskite STO thin films with Si substrate is of technological importance for fabricating multifunctional devices on Si (100), the preferred substrate for microelectronic industry. By using molecular beam epitaxy, researchers succeeded in growing STO (100) directly on Si (100) <sup>[22-25]</sup>. PLD has been demonstrated to be effective for a controlled growth of STO (110) directly on Si (100) <sup>[26, 27]</sup>. But in most of these cases, an intermediate layer forms which was crucial for the subsequent formation of the STO film <sup>[24, 25, 26]</sup>. The chemical and thermal stability and their influence on physical properties have to be considered for device applications. On the other hand, more stable and insulating buffer layers like ceria doped zirconia <sup>[28]</sup> and CeO<sub>2</sub>/c-YSZ <sup>[29]</sup> were also used to grow epitaxial STO (110) films. In this study, the primary focus is on the details of bi-epitaxial growth and the role of domain boundaries on the magnetotransport properties. First we analyze the bi-epitaxial integration of LSMO (110) thin films on Si (100) using c-YSZ/STO buffer layers and study the atomic structure of the c-YSZ/STO interface. Second, we perform detailed study of the effect of domain boundaries in LSMO thin films on the electrical, magnetic and magnetotransport properties.

We have integrated STO (110) bi-epitaxial films with Si (100) substrate using c-YSZ buffer. The growth of STO on c-YSZ takes place with two in-plane domain variants and can be explained by the paradigm of domain matching epitaxy (DME), where integral multiples of lattice planes match across the film-substrate interface to accommodate the misfit under a large misfit conditions 10%. Here the critical thickness is less than a monolayer and misfit

strain can be relaxed from the beginning so that the rest of the film can grow defect-free, except the thermal strain. The LSMO (110) films deposited on STO/c-YSZ/Si are ferromagnetic with  $T_C \sim 324\text{K}$  and exhibit metal to insulator transition at  $285\text{K}$ . The easy axis of the magnetization lies in the LSMO (110) plane whereas the hard axis is along the out-of-plane [110] direction. The LSMO films showed hysteresis loops in MR measurements under applied field in both in-plane and out-of-plane directions. The temperature dependent MR showed a peak in low temperature region followed by a monotonic decrease up to  $350\text{K}$ . The highest MR obtained in this study is  $-32\%$  at  $50\text{K}$  and  $50\text{ kOe}$  for magnetic field parallel to the film plane whereas the room temperature MR is  $-4\%$  at  $10\text{ kOe}$  and  $-17\%$  at  $50\text{ kOe}$ . The hysteresis in MR and the controlled domain boundaries in bi-epitaxial  $\text{La}_{0.7}\text{Sr}_{0.3}\text{MnO}_3$  films can offer significant advantages over the polycrystalline counterparts, where microstructure control presents a serious challenge in terms of reliability of solid state devices.

### 5.3 Experimental Details:

The LSMO/STO/c-YSZ/Si (001) heterostructure was grown in a multi target PLD chamber that utilized KrF laser of  $248\text{ nm}$  wavelength and  $25\text{ ns}$  pulse duration. The target to substrate distance was maintained at  $4\text{ cm}$  during the deposition and the base pressure of the chamber before the deposition was less than  $1 \times 10^{-6}\text{ Torr}$ . The laser energy density was  $2.8\text{ J/cm}^2$  for c-YSZ and  $3.0\text{ J/cm}^2$  for STO and LSMO whereas the repetition rate was  $5\text{ Hz}$  for all the layers. The substrate was vapor cleaned in trichloro-ethylene at  $200^\circ\text{C}$  and then ultrasonically cleaned by immersing in acetone and methanol each for  $5\text{ min}$ . Initially after heating the substrate to  $675^\circ\text{C}$ , the c-YSZ layer was deposited with  $500$  pulses under  $1 \times 10^{-5}\text{ Torr}$  vacuum and the rest under  $8.5 \times 10^{-4}\text{ Torr O}_2$ , and then oxygen partial pressure was

adjusted to  $1 \times 10^{-2}$  Torr for the deposition of STO. After that the substrate was taken to  $700^\circ\text{C}$  and LSMO was deposited at  $3 \times 10^{-1}$  Torr oxygen partial pressure. Once the deposition was completed, the sample was cooled down to room temperature at  $10^\circ\text{C}/\text{min}$  under 5 Torr oxygen partial pressure. The phase structure of the films was determined by X-ray diffraction  $\theta$ - $2\theta$  scans using Rigaku X-ray diffractometer with  $\text{Cu K}\alpha$  (0.154 nm) radiation. The JEOL 2010F TEM was used for imaging and to obtain selected area electron diffraction (SAED) patterns. The aberration corrected STEM–FEI Titan 80-300 was used for high-angle annular dark field (HAADF) imaging of the heterostructure. The cross-sectional TEM specimen was wedge polished until 1  $\mu\text{m}$  thickness and then ion milled to electron transparency. The magnetic measurements were done using Quantum design Super-conducting Quantum Interference Device (SQUID). Magneto-transport measurements were performed on 5 mm  $\times$  5 mm LSMO thin films in Quantum Design, EverCool-II PPMS. Four indium dots were mechanically pressed on the corners of the sample to perform four probe resistance measurements in van der Pauw configuration. The sample with pressed indium dots was mounted on a custom built rotatable pogo-pin setup in the PPMS. All the measurements were performed in AC delta mode with model 6000 PPMS controller to measure magnetoresistance accurately without any error in the measurements.

#### 5.4 Results and Discussion:

The XRD  $2\theta$  scan acquired on the LSMO/STO/c-YSZ/Si heterostructure is shown in Figure 5.1. The growth of STO thin film on c-YSZ (002) took place with (110) out of plane orientation at the deposited substrate temperature of  $670^\circ\text{C}$ . Since the LSMO (3.876 Å) is lattice matched with STO (3.905 Å), it resulted in the same orientation as STO. The STO (110) has a peak position at  $32.364^\circ$ , which corresponds to a lattice constant of 3.911 Å.

Compared to the bulk lattice constant, the STO film is tensile strained about +0.1% along the out-of-plane direction. The details of the STO growth and strain analysis will be discussed later. The LSMO film is -1.7 % compressively strained along the [110] out-of-plane direction as measured from the XRD  $2\theta$  scan. All of the films exhibit a single out-of-plane orientation, inferring that as grown films are either highly textured or epitaxial in nature. In order to determine the crystalline and epitaxial characteristics, and the interface microstructure of the films, we have performed detailed cross-sectional transmission electron microscopy study of the heterostructure.

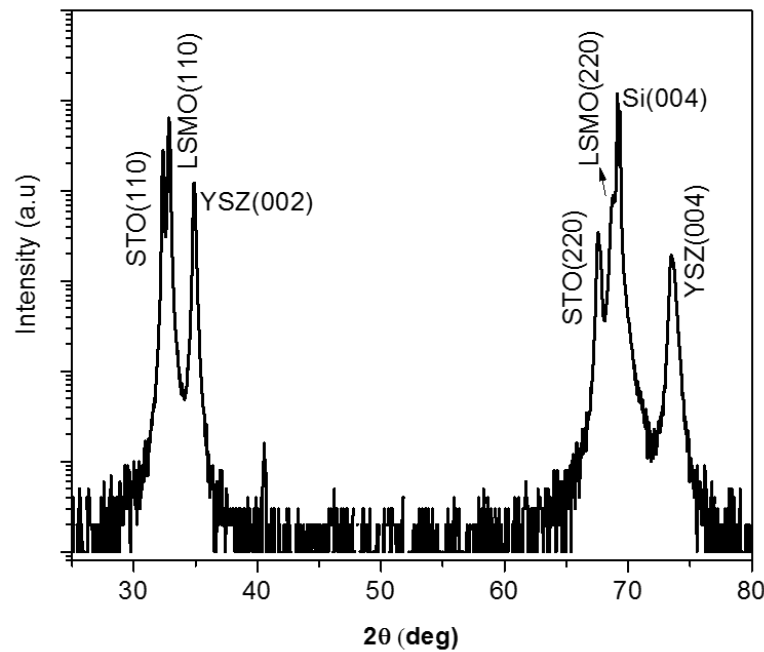


Figure 5.1: XRD  $2\theta$  scan of LSMO/STO/YSZ heterostructure grown on Si (001) substrate.

Figure 5.2(a) shows the low magnification image of the heterostructure, where columnar grains of STO and the extension of grain boundaries into LSMO film are visible. The growth rates of STO and LSMO are  $0.95 \text{ \AA}$  and  $1 \text{ \AA}$  per laser pulse at the chosen oxygen partial

pressure and substrate temperature. The epitaxial nature of the films is confirmed from the selected area electron diffraction (SAED) pattern acquired from the cross-section sample. The growth of c-YSZ on Si occurs with cube-on-cube, which can be explained in the paradigm of domain matching epitaxy<sup>[30]</sup>. Further details of the c-YSZ thin film epitaxy can be found elsewhere<sup>[31]</sup>. Figure 5.2(b) shows the indexed SAED pattern acquired at the c-YSZ/STO interface. It is found that there are two different in-plane domain variants of STO on c-YSZ with a single out-of-plane orientation and they are related by an in-plane rotation of 27.37° in the (110) plane. The epitaxial relationship between c-YSZ and STO can be written as  $[110] (001) \text{ c-YSZ} \parallel [\bar{1}\bar{1}\bar{1}] (110) \text{ STO}$  (or)  $[110] (001) \text{ c-YSZ} \parallel [\bar{1}\bar{1}\bar{2}] (110) \text{ STO}$ . The LSMO film on STO grows pseudo-cubic and has two in-plane domain variants with the same single out-of-plane orientation as STO. The epitaxial relationship between STO and LSMO can be written as  $[\bar{1}\bar{1}\bar{1}] (110) \text{ STO} \parallel [\bar{1}\bar{1}\bar{1}] (110) \text{ LSMO}$  (or)  $[\bar{1}\bar{1}\bar{2}] (110) \text{ STO} \parallel [\bar{1}\bar{1}\bar{2}] (110) \text{ LSMO}$ . The lattice constants of STO and LSMO measured from SAED patterns are in agreement with those obtained from the XRD.

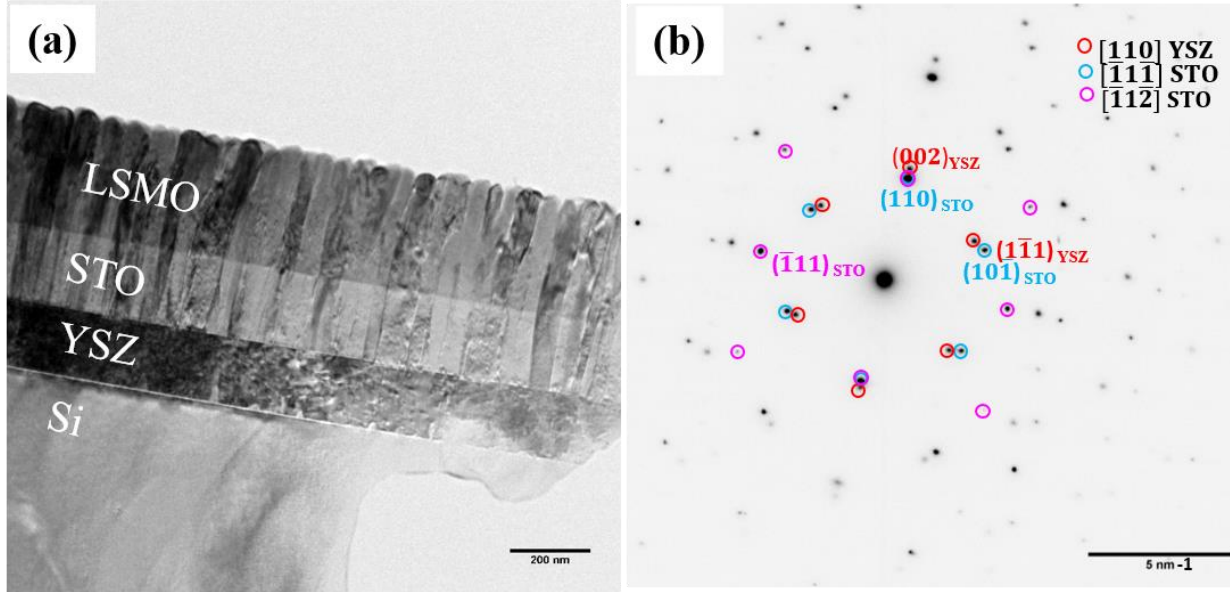


Figure 5.2: TEM study of the Si/YSZ/STO/LSMO heterostructure showing (a) low magnification image, (b) SAED pattern near the YSZ/STO interface taken along [110] zone axis of YSZ.

The bi-epitaxial (or) two domain growth of STO is evident from the images shown in Figure 5.3. The high angle annular dark field (HAADF) STEM-Z image acquired at the c-YSZ/STO interface along the  $[\bar{1}1\bar{1}]$  zone of STO is shown in Figure 5.3(a). Figure 5.3(b) shows the high resolution TEM image acquired at the c-YSZ/STO interface along the  $[\bar{1}1\bar{2}]$  zone of STO. In both cases, we did not observe any secondary phase formation or reaction at the interface. The growth of STO on c-YSZ can be explained by the DME paradigm. Since the critical thickness will be less than a monolayer above which dislocations are formed, most of the strain will be located at the interface and the rest of the film grows defect-free. For the domain one shown in Figure 3(a), the two times the planar spacing of  $(1\bar{1}2)$  planes of STO ( $3.188 \text{ \AA}$ ) matches with that of  $(110)$  planes of YSZ ( $3.634 \text{ \AA}$ ) with a misfit strain of  $-12.2 \%$ . According to DME, this leads to the  $7/8$  and  $8/9$  matching of the planes and hence results in a misfit strain (in-plane)  $< 1 \%$ . From Figure 5.3(a), we clearly see the alignment of 8 planes of

YSZ with 9 planes of STO and also the presence of edge dislocations at the interface. As shown in Figure 5.3(b), two times the planar spacing of  $(\bar{1}1\bar{1})$  planes of STO (4.5094 Å) matches with that of (110) planes of YSZ (3.634 Å) with a misfit strain of 24.08 %. According to DME, this leads to the 4/3 and 5/4 matching of the planes and hence results in a misfit strain < 1 %. The STO film with 0.1% strain as measured from the XRD and SAED, also corroborates with DME paradigm. This residual strain could be due to thermal mismatch and/or defect induced and can be reduced further by slowly cooling the sample down to room temperature under O<sub>2</sub> pressure close to atmosphere pressure. In contrast, the LSMO film of thickness 250 nm is found to have -1.7% strain in the out-of-plane direction, which is a cumulative of lattice, thermal mismatch and defect induced. Thus, smaller misfit is harder to relax and is retained within the film. The lattice matched growth of LSMO on STO can be seen from the images in Figure 5.4.

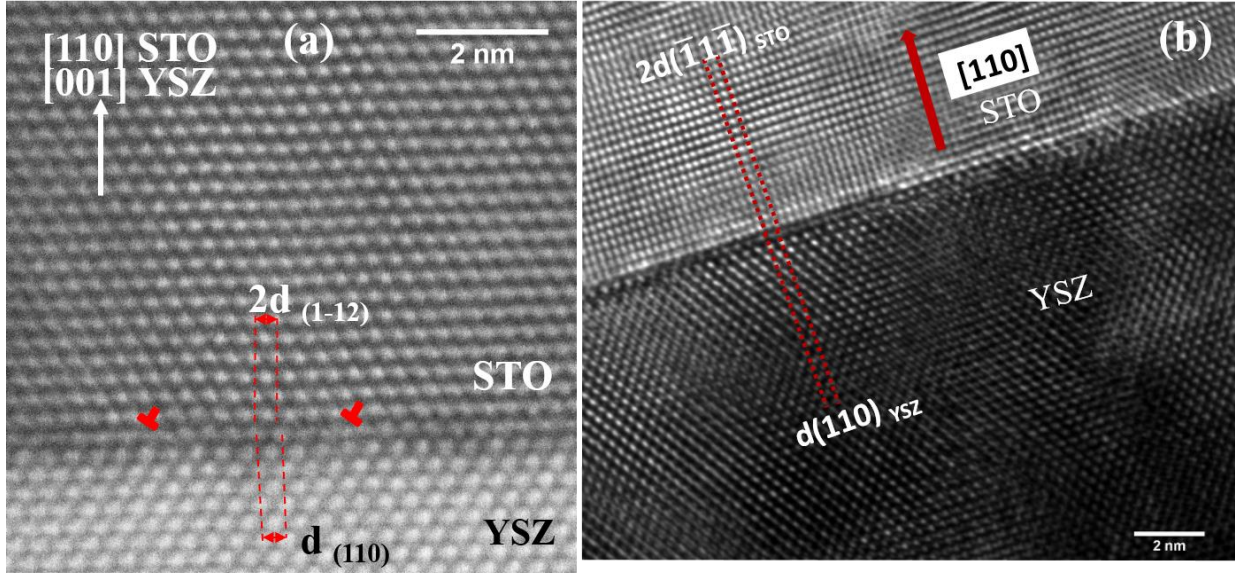


Figure 5.3: (a) HAADF STEM-Z image acquired at the YSZ/STO interface along the  $[110]$  zone of YSZ (or  $[111]$  zone of STO) and (b) High resolution TEM image of the YSZ/STO interface along  $[110]$  zone of YSZ (or  $[\bar{1}1\bar{2}]$  zone of STO). We can see the domain matching of the planes across the interface indicated by dotted lines.

The temperature dependent resistivity (in zero field) of the LSMO film is plotted in Figure 5.5. The resistivity (10-20 m $\Omega$ .cm) is comparable to epitaxial films<sup>[21, 32]</sup> and very less than that of polycrystalline films<sup>[19, 21]</sup>. The in-plane domain boundaries do not seem to have a much effect on the resistivity of the film but they reduce the metal to insulator transition temperature  $T_{MI}$ . The  $T_{MI}$  in the present case is 285K which is  $\sim 40$ K less than the  $T_C$  (324K) determined from the magnetization measurements. The  $T_{MI}$  values  $> 300$ K are obtained in good quality epitaxial films grown on buffered STO films<sup>[33-35]</sup>, on STO<sup>[36, 32]</sup> and  $\text{LaAl}_2\text{O}_3$ <sup>[32, 37, 38]</sup> single crystals. Much reduced  $T_{MI}$  values were observed in polycrystalline films directly grown on Si<sup>[39, 40]</sup>. The value of  $T_{MI}$  in the present case is in between those of polycrystalline and epitaxial films.

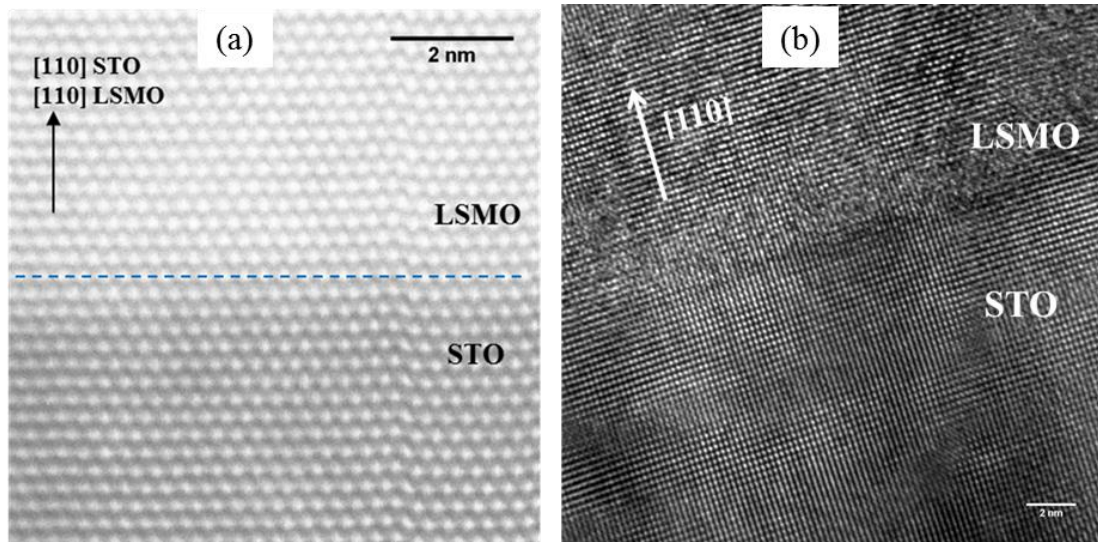


Figure 5.4: (a) HAADF STEM-Z image acquired at the STO/LSMO interface [111] zone of STO and (b) High resolution TEM image of the STO/LSMO interface along  $[\bar{1}1\bar{2}]$  zone of STO. We can see the growth of LSMO on STO via lattice matching epitaxy.

Both temperature- and field-dependent magnetization data of the LSMO thin film are presented in Figure 5.6 (a-d). Plotted in the upper panel are the isothermal field-dependent magnetization (M-H) plots measured in magnetic fields up to  $\pm 10$  kOe applied along (a) in-plane and (b) out-of-plane to the films at 10, 200 and 300 K. The in-plane magnetization (a) begins to saturate from about 1000 Oe and reaches saturation state by 10 kOe. The saturation magnetization ( $M_s$ ) increases by nearly threefold from  $\sim 120$  emu/cc at 300K to  $\sim 330$  emu/cc at 10K. The out of plane magnetization (b) showed ‘S’ shaped curves, which did not saturate even up to 10 kOe for all the temperatures. From here onwards, the in-plane and out-of-plane will be denoted as  $H_{\parallel}$  and  $H_{\perp}$  configurations, respectively.

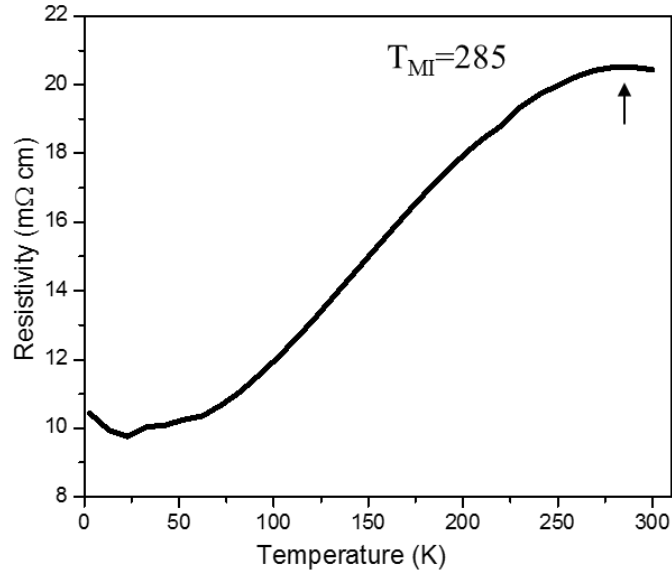


Figure 5.5: Resistivity versus temperature measurement of LSMO thin film acquired from 4K to 300K in the absence of magnetic field.

The insets of the top panel are the enlarged M-H hysteresis loops showing the coercivities varying from 23 Oe at 300K to about 300 Oe at 10K for  $H_{\parallel}$  and 33 Oe at 300K to 327 Oe at 10K for  $H_{\perp}$  configurations. It is evident from the M-H data that the easy axis of magnetization lies in the (110) plane and hard axis is along the [110] out-of-plane direction. This is in agreement with the reported literature, where it was found that in epitaxial films, tensile in-plane strain induces an in-plane easy axis and compressive in-plane strain induces an out-of-plane easy axis <sup>[41, 32]</sup>. The temperature dependence of the magnetization (M-T) is plotted in the lower panel of Figure 5.6, for (c)  $H_{\parallel}$  and (b)  $H_{\perp}$  orientations. From the M-T plots we say that the LSMO sample undergoes the magnetic phase transition from a ferromagnetic phase at low temperatures to a paramagnetic phase well above room temperature with the Curie temperature,  $T_C \approx 324K$  (determined from the peak in  $dM/dT$  versus T plot).

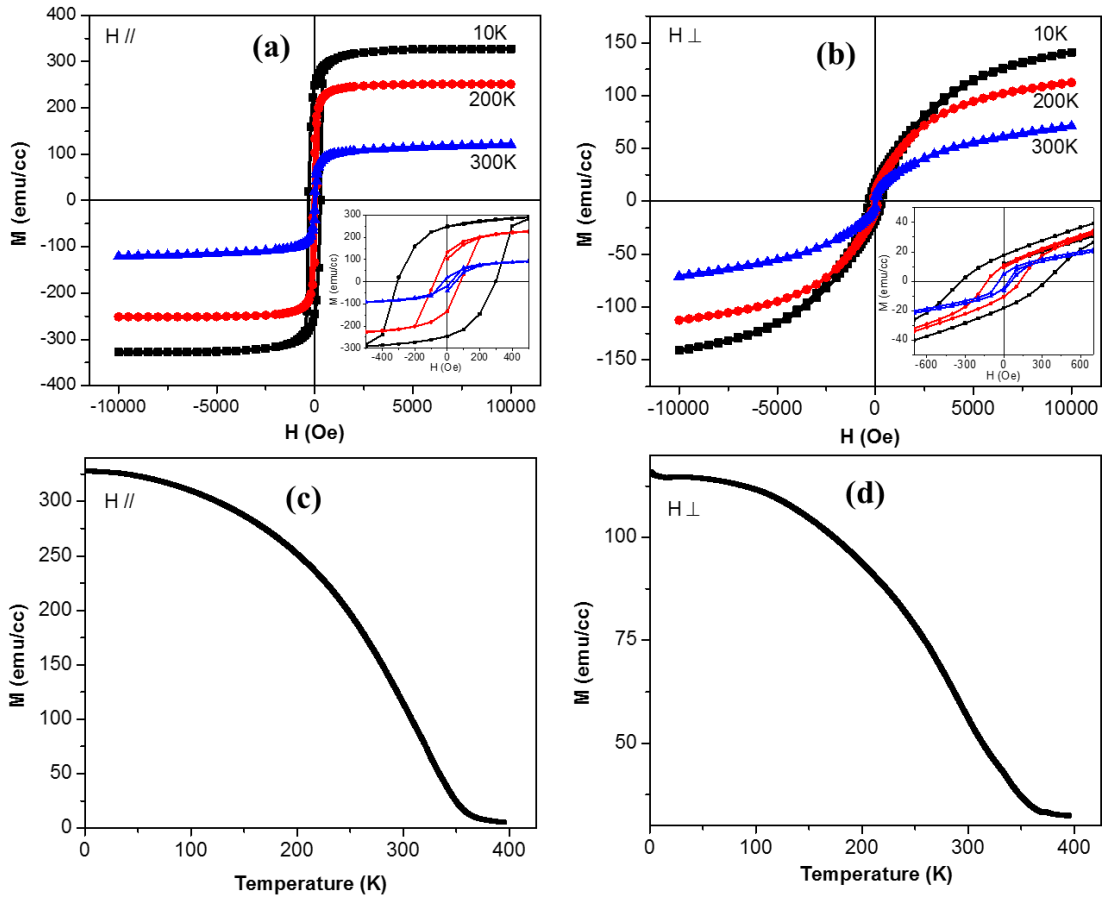


Figure 5.6: Magnetic field dependent magnetization data of the LSMO (110) thin film with field applied (a) in-plane denoted as  $H_{\parallel}$  (b) out-of-plane denoted as  $H_{\perp}$ . Temperature dependent magnetization data of the LSMO thin film with field applied (c) in-plane denoted as  $H_{\parallel}$  (d) out-of-plane denoted as  $H_{\perp}$ . The insets of (a) and (b) shows the enlarged view of the same showing coercivities.

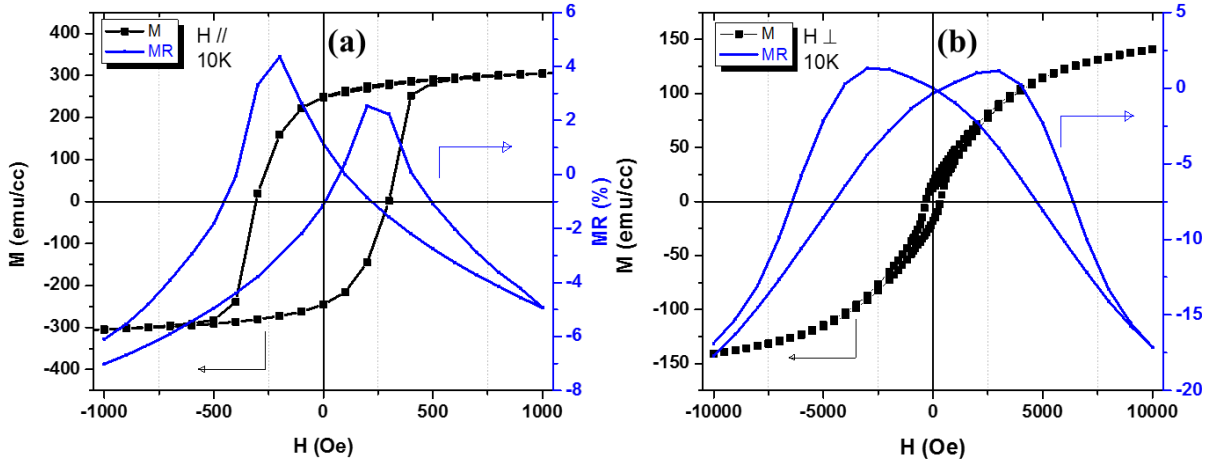


Figure 5.7: Magnetic field dependent magnetization and magnetoresistance of LSMO (110) thin film measured at 10K with field applied (a) in-plane denoted as  $H_{\parallel}$  (b) out-of-plane denoted as  $H_{\perp}$ .

After the magnetization measurements, we have performed detailed magnetotransport measurements on LSMO thin films. Conventionally, MR is defined as the ratio of the difference in resistance values in the presence of an applied magnetic field to that in zero-field and often expressed as a percentage value given as

$$MR = \left( \frac{\rho(H) - \rho(0)}{\rho(0)} \right) \times 100 \quad \dots \dots \dots (5.1)$$

Where,  $\rho(H)$  and  $\rho(0)$  are the resistivities in the presence of finite and zero-magnetic fields, respectively. In general, in case of manganites, the resistance decreases in the presence of a magnetic field and hence the difference  $[\rho(H) - \rho(0)]$  is negative. We have measured MR for both  $H_{\parallel}$  and  $H_{\perp}$  configurations.

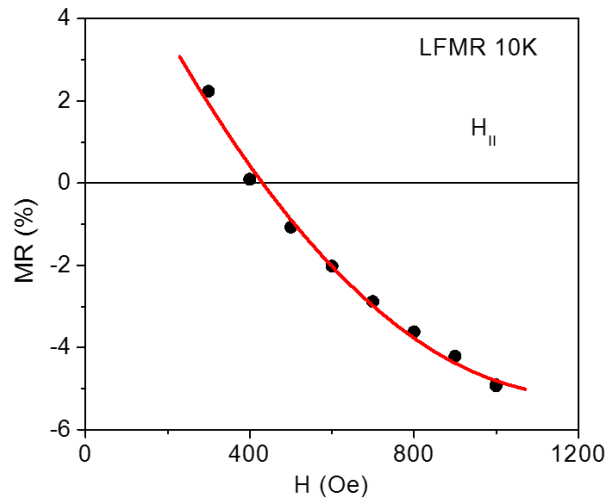


Figure 5.8: The magnetoresistance variation with magnetic field up to 1 kOe measured at 10K in  $H_{\parallel}$  configuration. The solid line represent the fit to the data using the equation  $MR = a_1 + a_2H + a_3H^2$ .

Figure 5.7 shows the MR and M-H hysteresis loops measured at 10K for  $H_{\parallel}$  and  $H_{\perp}$  configurations for the LSMO thin film. One of the most striking features of this current investigation is the observation of hysteresis in magnetoresistance data during the magnetic field sweeps. In the literature, very few groups <sup>[10, 21, 42]</sup> reported the observation of hysteresis loops in MR and most of them are on polycrystalline films. The shape of the MR curves is more like a butterfly-type in case of  $H_{\perp}$  configuration at the measured temperatures of 5, 10, 25, 50, 100, and 200K. While the isothermal MR in  $H_{\parallel}$  showed a cusp-like variation, the MR in  $H_{\perp}$  reveals a smudged or rounded off nature. The observed MR, as defined in the equation (1), in our films is predominantly negative after some initial upturn with positive MR at low fields. Also, there is considerable hysteresis present in both  $H_{\parallel}$  as well as in  $H_{\perp}$  measurements. The field at which crossover from positive to negative MR occurs, is nearly matches with the coercive field for  $H_{\parallel}$  and with the field where pinching of M-H occurs

for  $H_{\perp}$ . One important aspect which was not discussed in the literature is that up to what temperature the hysteresis in MR is present. We found that hysteresis in MR is present below the temperature  $T_{MI}$  when LSMO is in ferromagnetic metal phase and above that we still see MR but no loop.

The films in the present study showed LFMR with the values better than epitaxial counter parts <sup>[21, 36]</sup> and comparable to LSMO:ZnO nanocomposite film on STO <sup>[36]</sup>. The LFMR at 50K and 10 kOe is about -16% for  $H_{\parallel}$  and -10% for  $H_{\perp}$  orientations. In order to understand the mechanism behind the LFMR, we have analyzed the data and fitted (shown in Figure 5.8) one of the positive branches of LFMR of the  $H_{\parallel}$  orientation to the following equation.

$$MR = a_1 + a_2H + a_3H^2 \dots\dots\dots (5.2)$$

The above data fits very well (goodness parameter  $R^2 = 0.9931$ ) to equation (5.2). The dominant contribution comes from the quadratic term, implying that the low field magnetoresistance data varies predominantly as  $\sim H^2$ . Since for a pure ferromagnetic phase the MR varies as  $H^2$  <sup>[43]</sup>, our LFMR data suggests that LSMO is in ferromagnetic phase at low temperatures. Since both spin dependent scattering and spin polarized tunneling across the grain boundaries have the same field dependence ( $M^2$ ), the mechanism for LFMR is either of these.

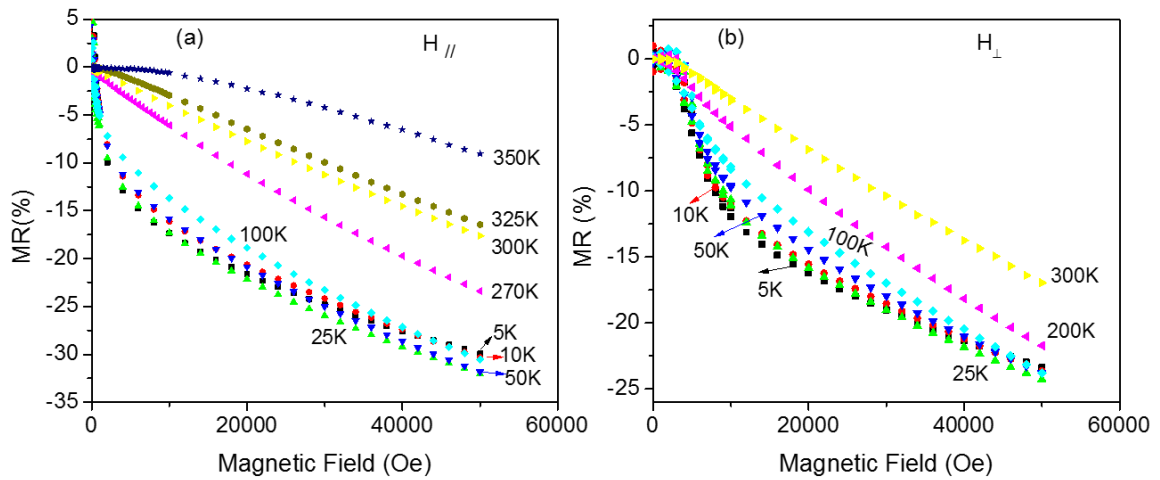


Figure 5.9: Isothermal magnetic field dependent magnetoresistance in the field range 0 - 50 kOe for (a) in-plane denoted as  $H_{||}$  (d) out-of-plane denoted as  $H_{\perp}$ .

The isothermal MR curves measured as a function of applied magnetic field up to  $\pm 50$  kOe are plotted in Figure 5.9. In order to gain a quantitative understanding of the nature and the shape of the MR curves, the MR data has been analyzed in the light of scaling theory<sup>[44]</sup>. For magnetic systems, especially in case of LSMO, involving several magnetic phases at different temperatures, such as ferromagnetic, antiferromagnetic, mixed phase or spin-glass type, scaling theory predicts different functional forms for the LFMR as well as normal or high field MR<sup>[45]</sup>. We have fitted the magnetic field dependence of MR data for the temperatures, 5, 10, 25, 50, 100, 200, 300, 325 and 350K to the equation (3) below,

$$MR = -\alpha(T)H^n \dots\dots\dots (5.3)$$

Where,  $\alpha$  and the exponent  $n$  assume different values for different magnetic phases which in turn vary as a function of temperature.

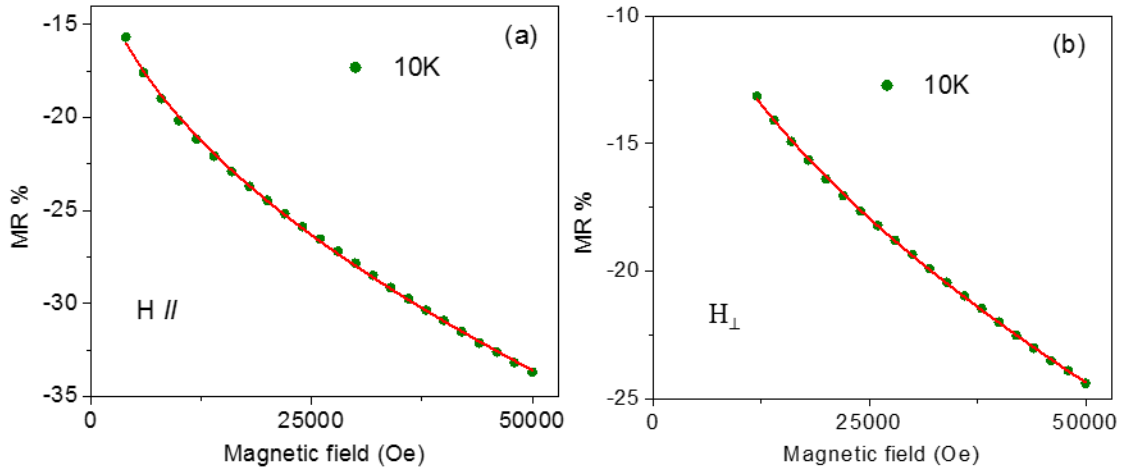


Figure 5.10: The magnetic field dependent magnetoresistance variation in the field range 4 - 50 kOe at 10K for (a)  $H_{\parallel}$  and (b)  $H_{\perp}$  configurations. The solid lines represent the typical fit to the data using equation  $MR = -\alpha(T)H^n$ .

Table 5.1 summarizes all the important fit parameters  $n$ ,  $\alpha$  and  $R^2$  for the best fits of the data using equation (3) at different temperatures, for both  $H_{\parallel}$  and  $H_{\perp}$  configurations in the field range 2 - 50 kOe. In Figure 5.10 (a and b) we present the representative best fits to the data using equation (3) for both  $H_{\parallel}$  (a) and  $H_{\perp}$  (b) MR data measured at 10 K in the field range 4-50 kOe. It is evident that the data fits are excellent with  $R^2$  values, 0.99942 for  $H_{\parallel}$  and 0.99978 for  $H_{\perp}$ , which are very close to unity. The exponent,  $n$  values extracted from the fits are 0.52 and 0.53 for  $H_{\parallel}$  and  $H_{\perp}$  measurements, respectively, signifies the long range FM order at low temperatures.

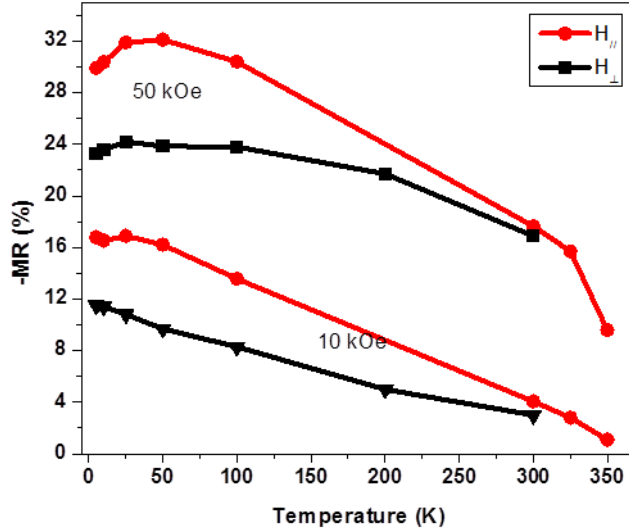


Figure 5.11: The temperature dependent magnetoresistance measured at 10 and 50 kOe for both  $H_{||}$  and  $H_{\perp}$  configurations.

The ferromagnetic phase observed at low temperatures in LSMO gradually changes to that of paramagnetic above room temperatures with a possible coexistence of several other types of magnetic orderings. The different magnetic phase signatures are reflected in MR data and can be captured by fitting the MR data at higher temperatures. A close look at the exponent in Table 5.1 for both orientations illustrates that, the exponent  $n$  varies from about 0.5 at low temperatures to 0.9 at 300K via 0.75 and 0.67 at intermediate temperatures. The temperature dependence of the MR at 10 kOe and 50 kOe for both configurations is plotted in Figure 5.11. At a given temperature and field the MR is higher in  $H_{||}$  configuration. It is known from the previous works that in transition metal doped lanthanum manganites MR peaks near  $T_C$  for good quality single crystals and epitaxial films <sup>[4-6, 10]</sup> whereas it shows a monotonic decrease with increase in temperature for polycrystalline films <sup>[40, 42]</sup>.

Table 5.1 Various fit parameters  $n$ ,  $\alpha$  and the goodness parameter,  $R^2$  for the best fits of the data using the equation  $MR = -\alpha(T)H^n$  for both (in-plane,  $H_{\parallel}$ ) and (out-of-plane,  $H_{\perp}$ ) configurations at various temperatures in the field range 2-50 kOe.

T(K)	n		$\alpha$		$R^2$	
	$\parallel$	$\perp$	$\parallel$	$\perp$	$\parallel$	$\perp$
5	0.42	0.44	0.25	0.18	0.99973	0.99996
10	0.52	0.53	0.09	0.07	0.99942	0.99978
25	0.48	0.52	0.14	0.08	0.99988	0.99993
50	0.51	0.53	0.10	0.08	0.99945	0.99993
100	0.64	0.68	0.03	0.01	0.99996	0.99992
200	-	0.76	-	0.01	-	0.99991
300	0.91	0.87	0.001	0.001	0.99988	0.99985
325	0.95	-	0.00059	-	0.99985	-
350	0.99	-	0.00039	-	0.99989	-

Here we found a peak in MR at low temperatures after which there is a monotonic decrease in MR with increase in temperature up to 350K. This peak temperature in MR is dependent on the applied field and also the measurement configuration. We speculate that this peak temperature might be related to the semiconductor to metal transition (or) valley temperature observed in the resistivity versus temperature curve. The highest MR obtained in this study is -32% at 50K and 50 kOe for  $H_{\parallel}$  configuration whereas the room temperature MR is -4% at 10 kOe and -17% at 50 kOe.

## 5.5 Conclusions:

We have successfully integrated bi-epitaxial  $\text{La}_{0.7}\text{Sr}_{0.3}\text{MnO}_3$  (110) thin films on Si (001) substrate with c-YSZ/STO buffer layers by pulsed laser deposition. The  $\text{La}_{0.7}\text{Sr}_{0.3}\text{MnO}_3$  and

STO thin films were grown with a single [110] out-of-plane orientation but with two in-plane domain variants, which is confirmed by detailed XRD and TEM studies. The bi-epitaxial growth of STO on c-YSZ involves larger misfit ( $> 10\%$ ) and can be explained by the paradigm of domain matching epitaxy. The epitaxial relationship between STO and c-YSZ can be written as  $[110] (001) \text{ c-YSZ} \parallel [\bar{1}\bar{1}\bar{1}] (110) \text{ STO}$  (or)  $[110] (001) \text{ c-YSZ} \parallel [\bar{1}\bar{1}\bar{2}] (110) \text{ STO}$ . The  $\text{La}_{0.7}\text{Sr}_{0.3}\text{MnO}_3$  thin films are ferromagnetic with Curie temperature 324K and showed metal to insulator transition at 285K. The resistivity of the  $\text{La}_{0.7}\text{Sr}_{0.3}\text{MnO}_3$  films is of the order of 10-20 m $\Omega$  cm, which is comparable to that of epitaxial thin films. The easy axis of the  $\text{La}_{0.7}\text{Sr}_{0.3}\text{MnO}_3$  thin films is in the (110) plane whereas the hard axis is along [110] out-of-plane. The  $\text{La}_{0.7}\text{Sr}_{0.3}\text{MnO}_3$  thin films showed unique hysteresis loops in magnetoresistance when low magnetic field is applied in both in-plane and out-of-plane directions. The in-plane MR showed cusp-like variation whereas out-of-plane MR reveals a smudged or rounded off nature. The highest MR obtained in this study is -32% at 50K and 50 kOe for  $H_{\parallel}$  configuration whereas the room temperature MR is -4% at 10 kOe and -17% at 50 kOe. The temperature dependent MR showed a peak in low temperature region followed by a monotonic decrease up to 350K. The hysteresis in MR and the controlled domain boundaries in case of bi-epitaxial  $\text{La}_{0.7}\text{Sr}_{0.3}\text{MnO}_3$  films integrated on Si (001) can offer considerable advantages over the polycrystalline counterparts in terms of improved functionality and reliability.

## 5.6 References:

1. G. H. Jonker and J. H. Van Santen, *Physica* 1950, 16, 337.
2. J. Volger, *Physica* 1954, 20, 49.
3. A. J. Millis, B. I. Shraiman and R. Mueller, *Phys. Rev. Lett.* 1996, 77, 175.
4. A. Urshibara, Y. Moritomo, T. Arima, A. Asamitsu, G. Kido and Y. Tokura, *Phys. Rev. B* 1995, 51, 14103.
5. S. Jin, T. H. Tiefel, M. McCormack, R. A. Fastnacht, R. Ramesh, and L. H. Chen, *Science* 1994, 264, 413.
6. R. von Helmholt, J. Wecker, B. Holzapfel, L. Schultz, K. Samwer, *Phys. Rev. Lett.* 1993, 71, 2331.
7. H. Y. Hwang, S-W. Cheong, N. P. Ong, and B. Batlogg, *Phys. Rev. Lett.* 1996, 77, 2041
8. L. E. Hueso, J. Rivas, F. Rivadulla, and M. A. López-Quintela, *J. Appl. Phys.* 1999, 86, 3881
9. A. Gupta, G. Q. Gong, G. Xiao, P. R. Duncombe, P. Lecouer, P. Trouilloud, Y. Y. Wang, V. P. Dravid, and J. Z. Sun, *Phys. Rev. B* 1996, 54, R15629
10. X. W. Li, A. Gupta, G. Xiao and G. Q. Gong, *Appl. Phys. Lett.* 1997, 71, 1124.
11. T. Walter, K. Dorr, K. H. Muller, B. Holzapfel, D. Eckert, M. Wolf, D. Schlafer, L. Schultz, and R. Grotzschel, *Appl. Phys. Lett.* 1999, 74, 2218.S

12. A Chen, Z. Bi, C-F. Tsai, J. Lee, Q. Su, X. Zhang, Q. Jia, J. L. MacManus –Driscoll, and H. Wang, *Adv. Funct. Mater.* 2011, 21, 2423.
13. M. Staruch, H. Gao, P-X Gao and M. Jain, *Adv. Funct. Mater.* 2012, 22, 3591.
14. S. J. Zhu , J. Yuan , B. Y. Zhu , F. C. Zhang , B. Xu , L. X. Cao , X. G. Qiu , B. R. Zhao, P. X. Zhang, *Appl. Phys. Lett.* 2007, 90, 112502.
15. S. A. Köster, V. Moshnyaga , K. Samwer , O. I. Lebedev , G. van Tendeloo ,O. Shapoval , A. Belenchuk, *Appl. Phys. Lett.* 2002, 81, 1648.
16. X. Ning , Z. Wang , and Z. Zhang, *Adv. Funct. Mater.* 2014, 24, 5393.
17. A. J. Millis, *Nature* 1998, 392, 147.
18. H. Roder, J. Zang, A. R. Bishop, *Phys. Rev. Lett.* 1996, 76, 1356.
19. S. L. Cheng and J. G. Lin, *J. Appl. Phys.* 2005, 98, 114318
20. J. Q. Xiao, J. S. Jiang, and C. L. Chien, *Phys. Rev. Lett.* 1992, 68, 3749.
21. J. Y. Gu, S. B. Ogale, M. Rajeswari, T. Venkatesan, R. Ramesh, V. Radmilovic, U. Dahmen, G. Thomas, and T. W. Noh, *Appl. Phys. Lett.* 1998, 72, 1113.
22. R. A. McKee, F. J. Walker, and M. F. Chisholm, *Phys. Rev. Lett.* 1998, 81, 3014.
23. Z. Yu, J. Ramdani, J. A. Curless, C. D. Overgaard, J. M. Finder, R. Droopad, K. W. Eisenbeiser, J. A. Hallmark, and W. J. Ooms, *Sci. Technol. B* 2000, 18, 1653.
24. X. Hu, H. Li, Y. Liang, Y. Wei, Z. Yu, D. Marshall, J. Edwards Jr., R. Droopad, J. Kulik, *Appl. Phys. Lett.* 2003, 82, 203.

25. J. Ramdani, R. Droopad, Z., J. A. Curless, C. D. Overgaard, J. Finder, K. Eisenbeiser, J. A. Hallmark, W. J. Ooms, V. Kaushik, P. Alluri, S. Pietambaram, *App. Surf. Sci.* 2000, 159–160, 127.
26. F. Sánchez, M. Varela, X. Queralt, R. Aguiar, and J. L. Morenza, *Appl. Phys. Lett.* 1992, 61, 2228.
27. J. H. Hao, J. Gao, Z. Wang, and D. P. Yu, *Appl. Phys. Lett.* 2005, 87, 131908.
28. S. Migita and S. Sakai, *J. Appl. Phys.* 2001, 89, 5421
29. T. Yamada, N. Wakiya, K. Shinozaki, and N. Mizutani, *Appl. Phys. Lett.* 2003, 83, 4815.
30. J. Narayan, and B. C. Larson, *J. Appl. Phys.* 2003, 93, 278.
31. S. Punugupati, J. Narayan, and F. Hunte, *Appl. Phys. Lett.* 2014, 105, 132401.
32. C. Kwon, M. C. Robson, K.-C. Kim, J. Y. Gu, S. E. Lofland, S. M. Bhagat, Z. Trajanovic, M. Rajeswari, T. Venkatesan, A.R. Kratz, R.D. Gomez, R. Ramesh, *J. Magn. Mater.* 1997, 172, 229.
33. A. Tiwari, A. Chug, C. Jin, D. Kumar, J. Narayan, *Solid State Communications*, 2002, 121, 679.
34. L. Méchin, C. Adamo, S. Wu, B. Guillet, S. Lebargy, C. Fur, J.-M. Routoure, S. Mercone, M. Belmeguenai, and D. G. Schlom, *Phys. Status Solidi A* 2012, 209, 1090.
35. D. Hunter, J. B. Dadson, K. Zhang, B. Lasley, K. Lord, T. M. Williams, R. R. Rakhimov, and A. K. Pradhan, J. Zhang and D. J. Sellmyer, *J. Appl. Phys.* 2006, 99, 08Q307.

36. A. Chen, W. Zhang, J. Jian, and H. Wang, C-F Tsai and Q. Su, Q. Jia, J. L. MacManus-Driscoll, *J. Mater. Res.* 2013, 28, 1707.
37. D. Yongsheng, Z. Xuefeng, Y. Dunbo, Y. Hui, *J. Rare Earths* 2006, 24, 560.
38. S. L. Cheng and J. G. Lin, *J. Appl. Phys.* 2005, 98, 114318.
39. S. M. Liu, X. B. Zhu, J. Yang, B. C. Zhoo, Z. G. Sheng, W. H. Song, J. M. Dai, Y. P. Sun, *Physica B* 2004, 353, 238.
40. M. Zhang, L. Lv, Z. Wei, X. S. Yang, X. Zhang, *J. Mod. Transport* 2014, 22, 50.
41. Yan Wu, Y. Suzuki, U. Rüdiger, J. Yu, A. D. Kent, T. K. Nath, and C. B. Eom, *Appl. Phys. Lett.* 1999, 75, 2295.
42. N. V. Dai, N. C. Thuan, L. V. Hong, N. X. Phuc and Y. P. Lee, *J. Korean Phys. Soc.* 2008, 53, 2727.
43. A. Fert, *Rev. Mod. Phys.* 2008, 80, 1517.
44. P.A. Lee and T. V. Ramakrishnan, *Rev. Mod. Phys.* 1985, 57, 287.
45. T. K. Nath, N. Sudhakar, E. J. McNiff, A. K. Majumdar, *Phys. Rev. B* 1997, 55, 12389.

# Chapter 6 Interface magnetism in epitaxial $\text{La}_{0.7}\text{Sr}_{0.3}\text{MnO}_{3-\delta}$ $/\text{Cr}_2\text{O}_3$ heterostructures integrated on Si (100)

## 6.1 Abstract:

$\text{Cr}_2\text{O}_3$  is a magnetoelectric and antiferromagnetic insulating material below its Néel temperature 307K. The ferromagnetic metallic  $\text{La}_{0.7}\text{Sr}_{0.3}\text{MnO}_{3-\delta}$  (LSMO) has a Curie temperature of ~350-370K. Study of interface magnetic properties of LSMO/ $\text{Cr}_2\text{O}_3$  is of scientific and technological interest, particularly, when it is integrated with CMOS-compatible silicon substrates. In this paper, we show the epitaxial growth of LSMO/ $\text{Cr}_2\text{O}_3$  heterostructures on c-YSZ-buffered Si (001) using pulsed laser deposition. The X-ray diffraction ( $2\theta$  and  $\Phi$ ) and TEM characterizations confirm that the films were grown epitaxially. The epitaxial relations can be written as  $[001]\text{Si} \parallel [001]\text{c-YSZ} \parallel [0001]\text{Cr}_2\text{O}_3 \parallel [111]\text{LSMO}$  and  $[100]\text{Si} \parallel [100]\text{YSZ} \parallel [10\bar{1}0]\text{Cr}_2\text{O}_3$  or  $[11\bar{2}0]\text{Cr}_2\text{O}_3 \parallel [10\bar{1}]\text{LSMO}$ . We have carried out a comprehensive study on this heterostructure as a function of LSMO thickness (66,264,528 nm). Interestingly, as the LSMO thickness increases from 66 to 528 nm, while keeping the  $\text{Cr}_2\text{O}_3$  thickness constant at 55 nm, the magnetic moment of the heterostructure increases by more than 2-fold and the magnetic nature has changed from ferromagnetic to super paramagnetic. In addition, LSMO/ $\text{Cr}_2\text{O}_3$  showed in-plane exchange bias with a maximum exchange bias field of 870e. From our experimental data, we believe the change in the magnetic anisotropy as a function of LSMO layer thickness could cause the change in magnetic moment and magnetic nature. The magnetic phase separation in oxygen

deficient LSMO layer could lead to in-plane exchange bias as  $\text{Cr}_2\text{O}_3$  is not expected to show in-plane exchange.

## 6.2 Introduction:

Magnetolectrics/multiferroic materials combine the unique combinations of electric and magnetic properties that simultaneously coexist<sup>123</sup>. These materials are viewed as potential building blocks in future data storage because their magnetism can be controlled by an electric field rather than an electric current, due to the reduction in power consumption. Hence, these materials have been under intense research investigation for potential applications in low power and non-volatile applications in the recent past. To realize the potential applications, researchers exploited the coupling among the ferroic order parameters such as electric-field switching of magnetization and vice versa. Single phase multiferroic materials show weak magnetoelectric coupling, not sufficient for potential applications. Several ferroelectric and ferromagnetic materials combinations such as  $\text{BiFeO}_3/\text{Permalloy}$ ,  $\text{BiFeO}_3/\text{CoFe}$ ,  $\text{BaTiO}_3/\text{La}_{0.7}\text{Sr}_{0.3}\text{MnO}_3$  have been chosen and studied for their multiferroic characteristics<sup>4 5 6</sup>. The above artificial two-phase multiferroic materials have limitations due to their low temperature operation. The switching of global magnetization has not been achieved in their bulk macroscopic magnetic hysteresis loops. At that point, the search for better multiferroic materials has begun.

Along that direction, it was realized that  $\text{Cr}_2\text{O}_3$  may be the material of choice to address the above issues as it was the first material to observe magnetoelectric effect<sup>7 8</sup>.  $\text{Cr}_2\text{O}_3$  is revived as a candidate for reversible electric control of magnetism at room temperature<sup>9 10</sup>.  $\text{Cr}_2\text{O}_3$  is magnetoelectric insulating antiferromagnetic oxide material.

Recently <sup>11,12</sup>, the electrically controlled exchange bias and magnetization has been achieved at room temperature in Cr<sub>2</sub>O<sub>3</sub> single crystals when it is interfaced with ferromagnetic Co/Pd, grown by molecular beam epitaxy. Following this breakthrough, the electric field control of magnetic anisotropy has been achieved <sup>13 14</sup> in epitaxial Cr<sub>2</sub>O<sub>3</sub> clusters, in which the authors have reported magnetoelectric coupling of more than three orders of magnitude higher than bulk.

La<sub>0.7</sub>Sr<sub>0.3</sub>MnO<sub>3</sub> (LSMO) is a highly spin polarized metallic ferromagnetic material <sup>15</sup>. These two materials exhibit these properties at operational temperatures. When these two thin film materials conjoined, they are expected to show novel properties such as superior magnetoelectric coupling and tunneling electro resistance due to their dissimilar magnetic and conducting nature, and, probably useful in interesting device applications such as non-volatile magnetic memories. To our knowledge, little or no work has been done in this direction <sup>16</sup>. Of particular interest, if they can be epitaxially integrated with CMOS compatible Si (100) substrates for applications in microelectronics. To date, there has been no in-detailed work reported on this heterostructure in integrating with Si (100) substrate and investigating the resulting magnetic properties, which forms the chief goal of the present work.

In our previous works <sup>17 18</sup>, we have epitaxially integrated Cr<sub>2</sub>O<sub>3</sub> layer with c-YSZ buffered Si(001) substrate and Al<sub>2</sub>O<sub>3</sub>(01-12) substrate. These films were found to exhibit ferromagnetic-like behavior up to 400K and reported to strongly reduce upon oxygen annealing. The oxygen annealed samples show bulk-like behavior. In the present work, we have used such bulk-like Cr<sub>2</sub>O<sub>3</sub>/c-YSZ buffered Si(001) substrates to deposit oxygen deficient epitaxial LSMO layers and study the magnetic properties as a function of LSMO

layer thickness by keeping the Cr<sub>2</sub>O<sub>3</sub> layer thickness constant at 55nm. The oxygen deficiency was resulted due to the usage of low oxygen partial pressure of  $1 \times 10^{-2}$  Torr during the deposition. This was the optimized partial pressure needed so as to prepare the LSMO(111) epitaxial layer, which is of our current interest. Therefore, the LSMO layers in the present heterostructures intrinsically contain oxygen deficiency.

### 6.3 Experimental Details:

The thin film heterostructures studied in this work were grown in a multi target PLD chamber that utilized KrF laser ( $\lambda=248$  nm and  $\tau=25$  ns). The target to substrate distance was maintained at 4 cm during the deposition and the base pressure of the chamber before the deposition was less than  $1 \times 10^{-6}$  Torr. The laser energy density was 2.8 J/cm<sup>2</sup> for c-YSZ, 3.2 J/cm<sup>2</sup> for Cr<sub>2</sub>O<sub>3</sub> and, 3.0 J/cm<sup>2</sup> for STO and LSMO. The laser repetition rate was 5 Hz for all the layers. The substrate was vapor cleaned in trichloro-ethylene at 200°C and subsequently cleaned in ultrasonic bath by immersing in acetone and methanol each for 5 min. Initially after heating the substrate to 675°C, the c-YSZ layer was deposited with 500 pulses under  $1 \times 10^{-5}$  Torr vacuum and the rest under  $8.5 \times 10^{-4}$  Torr O<sub>2</sub>, and then oxygen partial pressure was adjusted to  $5 \times 10^{-2}$  Torr for the deposition of Cr<sub>2</sub>O<sub>3</sub>. After Cr<sub>2</sub>O<sub>3</sub> deposition, the substrate was taken to 700°C and the LSMO was deposited under different oxygen partial pressures. Once the deposition was completed, the samples were cooled down to room temperature at 10°C/min under the same oxygen partial pressure used to deposit the LSMO layer. The phase structure of the films was determined by X-ray diffraction  $\theta$ -2 $\theta$  scans using Rigaku X-ray diffractometer with Cu K $\alpha$  (0.154 nm) radiation. The in-plane orientation of the films was determined by  $\Phi$  scans using Panalytical X'Pert PRO MRD HR X-Ray Diffraction System. The JEOL 2010F TEM was used for imaging and selected area electron diffraction (SAED)

patterns. The cross-sectional TEM specimen was wedge polished until 1  $\mu\text{m}$  thickness and then ion milled to electron transparency. The magnetic measurements were done using Quantum design Super-conducting Quantum Interference Device (SQUID). Transport measurements were performed on 5 mm  $\times$  5 mm thin films in Quantum Design, EverCool-II PPMS. Four indium dots were mechanically pressed on the corners of the sample to perform four probe resistance measurements in van der Pauw configuration.

#### 6.4 Results and Discussion:

Figure 6.1 displays the  $\theta$ - $2\theta$  XRD pattern acquired on the LSMO(66nm)/Cr<sub>2</sub>O<sub>3</sub>(55nm)/c-YSZ/Si(001) heterostructure. It shows the effect of oxygen partial pressure during the LSMO growth on the crystal orientation. In our previous publication<sup>17</sup> we have discussed the details of growth and characterization of epitaxial Cr<sub>2</sub>O<sub>3</sub>/c-YSZ/Si(001) heterostructures. In the present study, we tuned the deposition conditions to achieve epitaxial LSMO(111) on Cr<sub>2</sub>O<sub>3</sub>/c-YSZ/Si(001). As shown in Figure 6.1(b), at  $1 \times 10^{-1}$  Torr oxygen partial pressure, which is typically used<sup>1920</sup> to grow LSMO films, our films exhibit (110), (111) and (200) orientations, indicating polycrystalline nature of the LSMO film. As the oxygen partial pressure reduced to  $1 \times 10^{-2}$  Torr, the other orientations disappeared and only (111) orientation and its higher order are present, suggesting that LSMO is highly textured or epitaxial. The peak near  $2\theta = 40^\circ$  in Figure 6.1(b) corresponds to both (006)Cr<sub>2</sub>O<sub>3</sub> ( $2\theta = 39.749$ ) and (111)LSMO ( $2\theta = 39.942$ ) because of the close matching of their  $2\theta$  values.

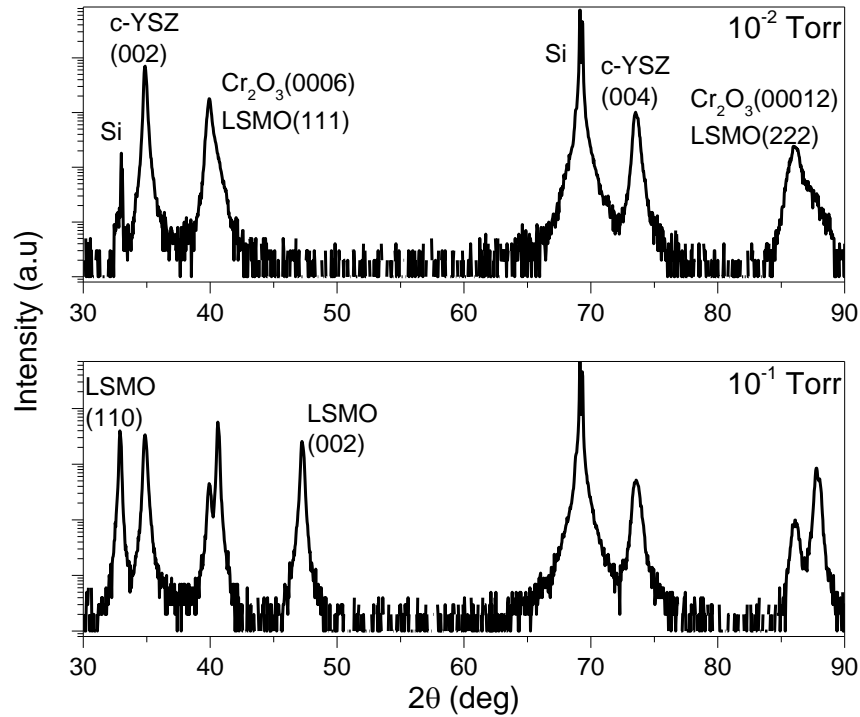


Figure 6.1: XRD  $\theta$ - $2\theta$  pattern acquired on the LSMO/Cr<sub>2</sub>O<sub>3</sub>/c-YSZ/Si(001) heterostructure showing the effect of O<sub>2</sub> partial pressure during LSMO growth.

In order to determine the epitaxial nature of the films, in particular of LSMO, we have performed XRD  $\Phi$ -scan on the thin film heterostructure grown at  $1 \times 10^{-2}$  Torr. Figure 6.2 displays the  $\Phi$ -scan data acquired on all the layers in the heterostructure for Si, c-YSZ, Cr<sub>2</sub>O<sub>3</sub> and LSMO, respectively. The growth of c-YSZ on Si occurs with cube-on-cube and the  $\Phi$ -scan data was collected on the {111} planes of c-YSZ and Si, which are inclined at  $54.73^\circ$  from the (001) plane. The  $\Phi$ -scan data collected on Cr<sub>2</sub>O<sub>3</sub> layer for  $\{10\bar{1}4\}$  reflections which are inclined at  $38.24^\circ$  from the (0006) plane shows twelve peaks, suggesting four different in-plane domain variants of Cr<sub>2</sub>O<sub>3</sub> with a single out-of-plane orientation. The growth of rhombohedral Cr<sub>2</sub>O<sub>3</sub> on c-YSZ occurs with four different in-plane domains which are rotated at  $30^\circ$  from each other<sup>17</sup>.

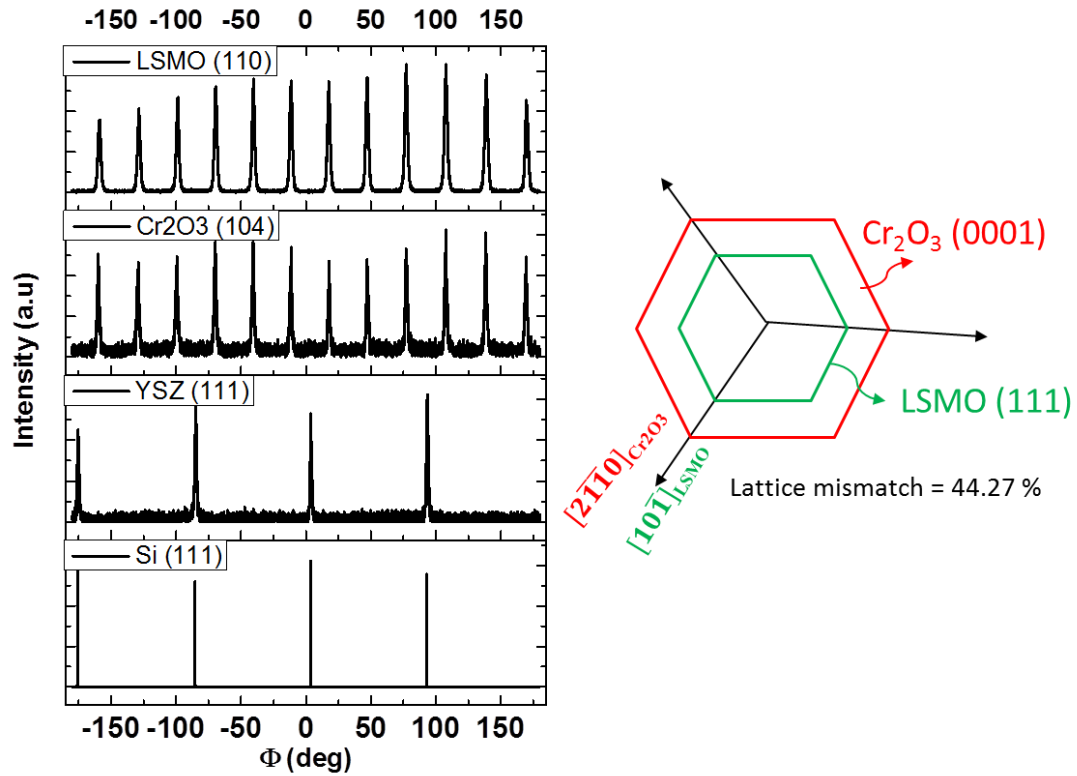


Figure 6.2. (a) XRD  $\phi$  scan of LSMO/Cr<sub>2</sub>O<sub>3</sub>/YSZ/Si(001) heterostructure. It was collected from (101), (10 $\bar{1}$ 4), (111) and (111) reflections of LSMO, Cr<sub>2</sub>O<sub>3</sub>, YSZ, and Si, respectively. (b) Schematic arrangement of the growth of LSMO(111) plane on Cr<sub>2</sub>O<sub>3</sub>(0001) plane.

The top panel in Figure 6.2 shows the  $\Phi$ -scan data collected on the LSMO layer for {110} planes which are inclined at 35.26° from the (111) plane. Similar to Cr<sub>2</sub>O<sub>3</sub>, the twelve peaks in LSMO indicate the formation of four different in-plane domain variants of LSMO with a single [111] out-of-plane orientation. The position of these peaks at the same  $\Phi$  angle to those of Cr<sub>2</sub>O<sub>3</sub> suggests that, the basal plane of LSMO(111) grows on Cr<sub>2</sub>O<sub>3</sub>(0001) without any in-plane rotation. The schematic in Figure 6.2(b) depicts the growth of LSMO(111) on Cr<sub>2</sub>O<sub>3</sub>(0001). The lattice misfit between  $d(10\bar{1})_{\text{LSMO}}$  and  $d(2\bar{1}\bar{1}0)_{\text{Cr}_2\text{O}_3}$  is 44.27% and thin film growth under large misfit systems can be explained by the domain epitaxy paradigm<sup>21</sup>.

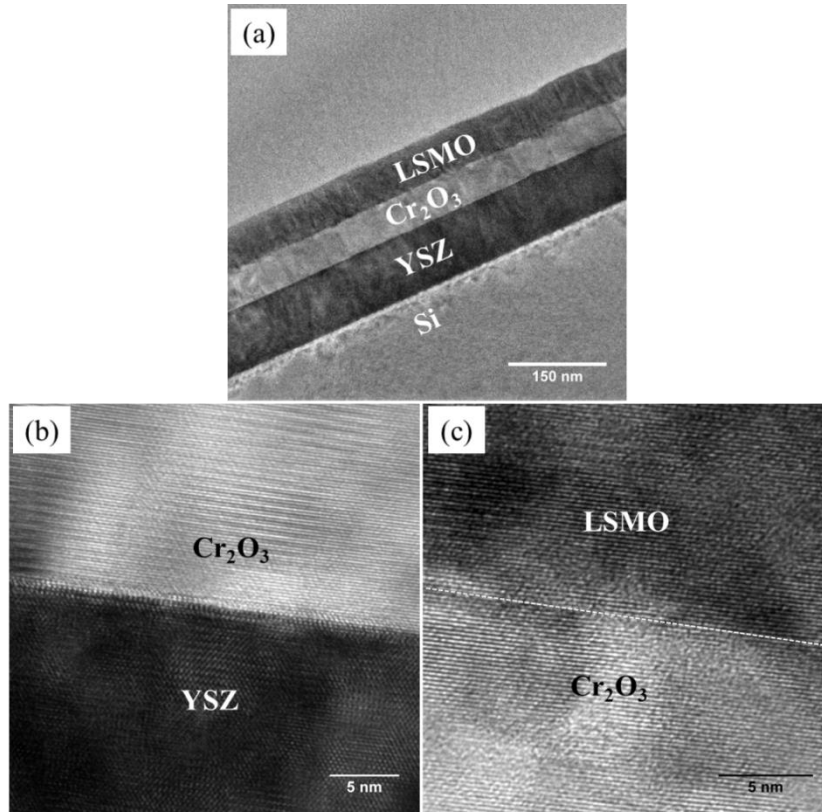


Figure 6.3: (a) low magnification cross-sectional TEM image of the LSMO/Cr<sub>2</sub>O<sub>3</sub>/c-YSZ/Si(001) heterostructure. (b) c-YSZ/Cr<sub>2</sub>O<sub>3</sub> interface. (c) Cr<sub>2</sub>O<sub>3</sub>/LSMO interface.

To determine the thicknesses of the various layers in the heterostructure and to know the interface microstructure, we performed cross-sectional TEM study on LSMO/Cr<sub>2</sub>O<sub>3</sub>/c-YSZ/Si(001). Figure 6.3(a) shows the low magnification image of the heterostructure. The growth rates of Cr<sub>2</sub>O<sub>3</sub> and LSMO are 0.4 Å<sup>0</sup> and 1.2 Å<sup>0</sup> per laser pulse, respectively. The TEM images captured near the c-YSZ/ Cr<sub>2</sub>O<sub>3</sub> and Cr<sub>2</sub>O<sub>3</sub>/LSMO are shown in Figure 6.3 (b) and (c), respectively. We did not observe any reaction or secondary phase formation at both the interfaces. Then, we have grown other heterostructures by varying the thickness of LSMO (66,264,528 nm) and keeping the Cr<sub>2</sub>O<sub>3</sub> thickness constant at 55nm to study the magnetic properties.

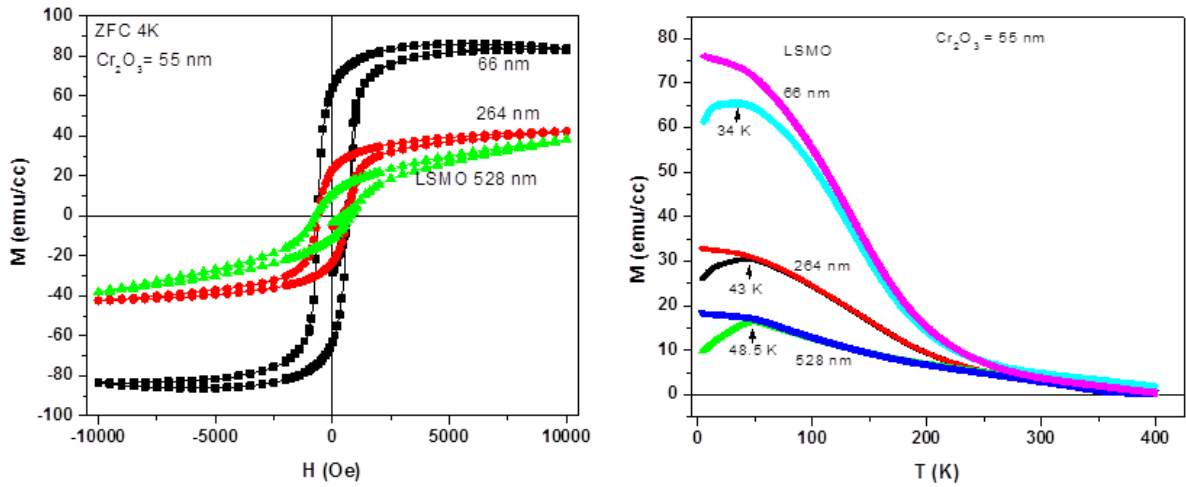


Figure 6.4: The isothermal magnetization (M-H) (a) and temperature dependent variation in magnetization (M-T) (b) of all three heterostructures, namely, LSMO (66 nm)/Cr<sub>2</sub>O<sub>3</sub> (55nm); LSMO (264 nm)/Cr<sub>2</sub>O<sub>3</sub> (55nm); LSMO (528 nm)/Cr<sub>2</sub>O<sub>3</sub> (55nm). As the LSMO thickness decreases and by keeping the Cr<sub>2</sub>O<sub>3</sub> layer thickness at 55nm, the magnetization increases. The temperature at which the ZFC and FC curves split is the ‘blocking temperature’ ( $T_b$ ).

The in-plane magnetic- and temperature-dependent magnetization measurements have been performed on the heterostructures consisting of LSMO (66,264,528 nm)/Cr<sub>2</sub>O<sub>3</sub> (55nm). In this work, the Cr<sub>2</sub>O<sub>3</sub> layer thickness is kept constant at 55 nm and found to exhibit antiferromagnetic properties. The data is presented in Figure 6.4(a,b). The magnetic field dependent magnetization variation collected at 4K is shown for all the three structures. Few remarkable observations can be noted: (a) the magnetization for LSMO (66nm)/ Cr<sub>2</sub>O<sub>3</sub> (55nm) is much higher than that of other two samples. This sample reveals typical ferromagnetic behavior, characterized by the saturation magnetization of 90emu/cc with the coercive field of 644Oe (b) as the LSMO layer thickness increases from 66 to 528 nm, the saturation magnetization decreases, and the nature of magnetic behavior changes from ferromagnetic to superparamagnetic. The latter behavior could be due to the change in magnetic anisotropy as a function of LSMO layer thickness. Such thickness dependent

magnetic anisotropy was observed in  $\text{La}_{0.7}\text{Ca}_{0.3}\text{MnO}_3$  (LCMO)<sup>22</sup> epitaxial thin films and in Fe/Co films<sup>23</sup>. The temperature dependence of zero-field (ZFC) and field cooled (FC) magnetization for all the three samples is plotted in the Figure 6.4 (b). The ferromagnetic Curie temperature of LSMO can be noticed at 300K, where the magnetization rises as the temperature decreases. In addition, the splitting between ZFC and FC curves is observed at around 35-50 K, called blocking temperature ( $T_b$ ). This observation has been observed and reproduced consistently over multiple times, thus ruling out the possible role of artifacts. The YSZ/Si (001) was shown to be diamagnetic and should not contribute the observed magnetic properties of the heterostructures presented in this study.

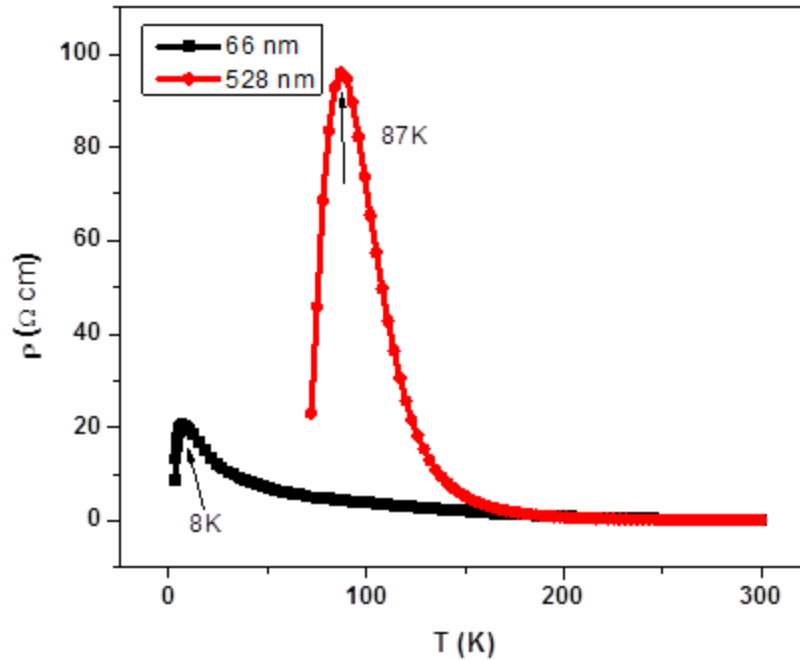


Figure 6.5: Temperature variation of resistivity of LSMO film of 66, 528 nm thicknesses as indicated. The metal to insulator transition in both the films is much reduced compared to bulk value.

We have performed transport measurements on the 66 and 528 nm thick LSMO films to find the reason for the change in their magnetic nature. Figure 6.5 shows the resistivity variation of temperature collected on these two samples. We found that the samples are highly resistive compared to typical LSMO samples since less oxygen partial pressure  $1 \times 10^{-2}$  Torr was used during the LSMO deposition. In LSMO, conduction occurs through hopping of electrons from  $Mn^{+3}$  to  $Mn^{+4}$  via oxygen atoms. Not only high resistivity, the metal to insulator transition ( $T_{MI}$ ) which usually occurs close to Curie temperature of 360K, is also reduced very much in our films. The 66 nm LSMO film showed much reduced  $T_{MI}$  of 8K compared to that of 528 nm LSMO film (87K).

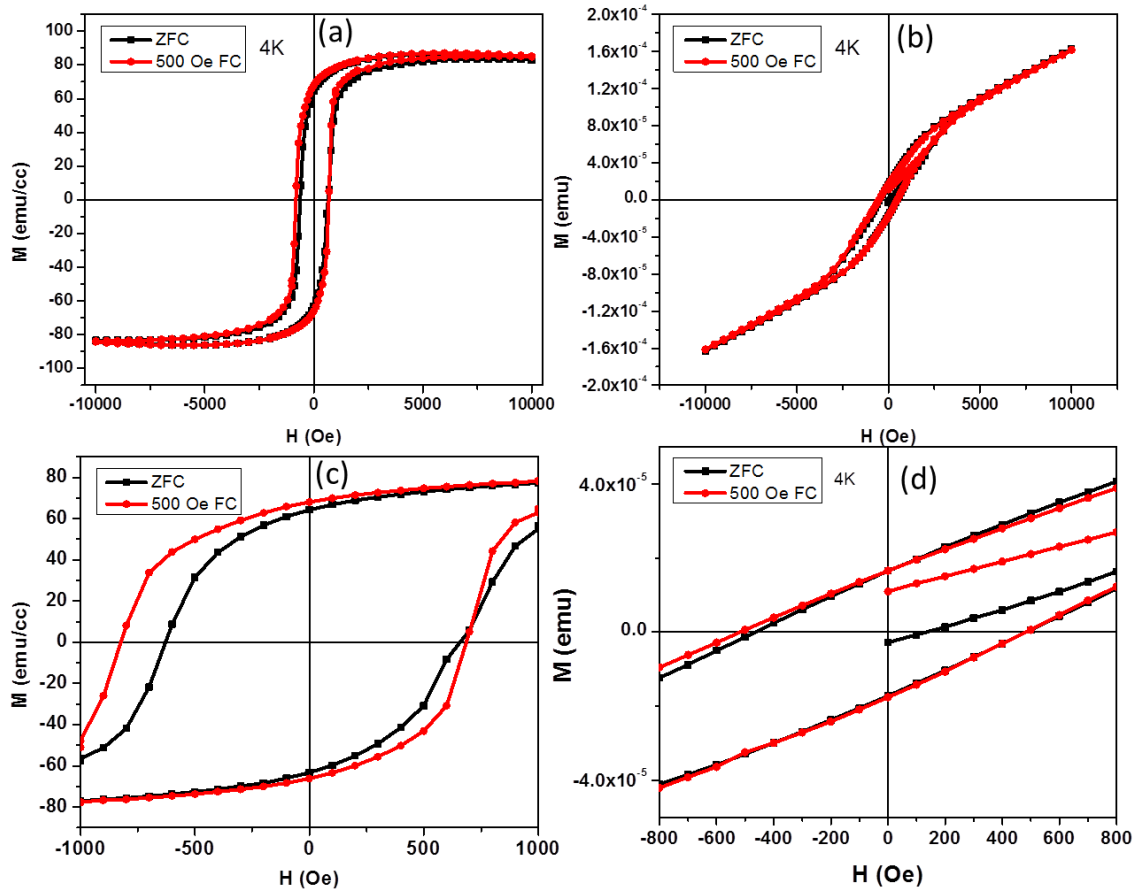


Figure 6.6: In-plane (a) and out of plan (b) M-H behavior of LSMO (66nm)/Cr<sub>2</sub>O<sub>3</sub> (55nm) collected at 4K under ZFC and 500 Oe FC conditions; The (c) and (d) shows the enlarged views of (a) and (b) respectively. Significant exchange bias is observed when the magnetic field is applied in-plane of the film, in comparison with that of out of plane.

As the LSMO (66nm)/Cr<sub>2</sub>O<sub>3</sub> (55nm) sample is showing interesting magnetic properties, we have chosen this sample for in-detail magnetization measurements. We have performed ZFC and FC (500 Oe) in-plane and out of plane M-H measurements on this sample. The data is plotted in Figure 6.6(a) and 6.6(b), respectively. The enlarged views of the same are plotted in Figure 6.6(c) and 6.6(d), respectively. As shown in Figure 6.6(c), we have observed an exchange bias of ~ 83Oe, when the magnetic field was applied in the plane of the film. In the out of plane orientation, the exchange bias is much less, ~ 28Oe. It can be clearly seen from

Figure 6.6(c, d). This is interesting because, one expect to see high exchange bias in perpendicular direction due to the alignment of spins in  $\text{Cr}_2\text{O}_3$  along the out-of-plane direction.

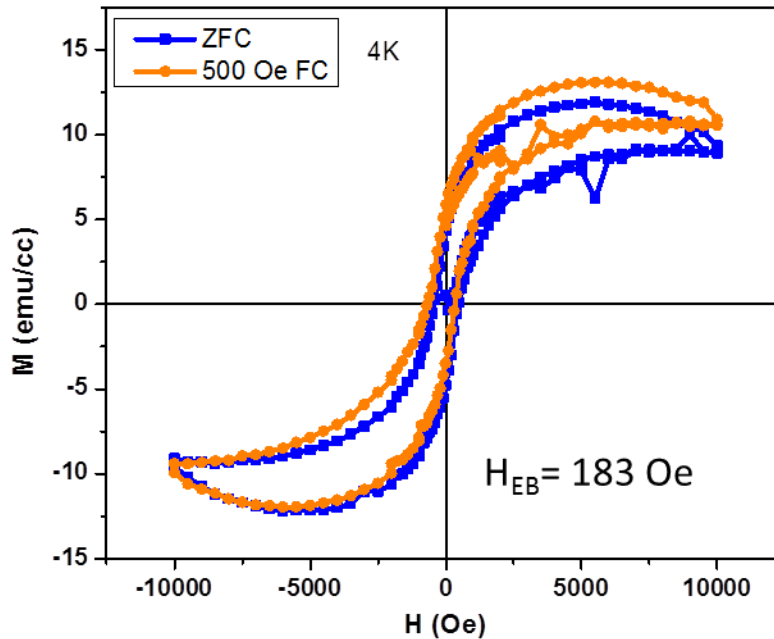


Figure 6.7: In-plane M-H behavior of LSMO (66nm)/STO(50 nm)/ $\text{Cr}_2\text{O}_3$  (55nm) collected at 4K under ZFC and 500 Oe FC conditions as denoted.

To probe the origin of exchange bias and to gain additional understanding on the variation in magnetic moment as a function of LSMO layer thickness, we have inserted a thin layer of epitaxial insulating non-magnetic  $\text{SrTiO}_3$  layer at LSMO (66nm)/  $\text{Cr}_2\text{O}_3$  (50nm) interface. The LSMO (66nm) layer preserves its pristine orientation even after inserting the STO layer in between. The in-plane M-H measurements have been performed at 4K on the resulting heterostructure. The data is presented in Figure 6.7, which shows the M-H behavior of LSMO(66nm)/STO(50 nm)/ $\text{Cr}_2\text{O}_3$  (55nm) under ZFC and FC (500 Oe) conditions. The

system still exhibited exchange bias as can be seen in the Figure 6.7 and the exchange bias field is found to increase to 1830e upon the STO insertion. This can be understood in a way that, LSMO layer is intrinsically oxygen deficient, resulting magnetic phase separation such as ferromagnetic and antiferromagnetic regions. This is due to the weaker double exchange interaction between  $Mn^{3+}$  and  $Mn^{4+}$  ions via oxygen. This clearly infers that the observed exchange bias does not arise from the interface exchange coupling between LSMO (66nm) and  $Cr_2O_3$  (55nm) layers, rather, appears from the LSMO (66nm) layer itself. This can also be evidenced from the splitting between ZFC and FC curves (see, Figure 6.4(b)). In addition, the ferromagnetic Curie temperature ( $T_C$ ) (~300K) and metal to insulator ( $T_{MI}$ ) transition of LSMO(111) are suppressed in all the heterostructures when compared to that of reported<sup>24 25</sup> value of 355K. More interestingly, upon STO layer insertion, the magnetization of the resulting heterostructure has been decreased by 9-times. Figure 6.8 compares the M-H behavior of three different structures ( $Cr_2O_3$ , LSMO (66nm) (on  $Cr_2O_3$ ), and LSMO (66nm) (on STO/ $Cr_2O_3$ ). This strongly confirms that the magnetization enhancement in LSMO (66nm)/  $Cr_2O_3$  (55nm) heterostructure is due to the magnetic super exchange interaction between LSMO (66nm) and  $Cr_2O_3$  (55nm) layers. Also, due to the fact that the observed magnetization is a strong function of LSMO thickness, the enhancement in magnetization is due to the interface magnetic exchange interaction. All these layers are grown relatively thick and lattice relaxed; there should not be any strain effect on the observed magnetic properties. There is no evidence for the noticeable charge transfer and doping as they confine to the interface.

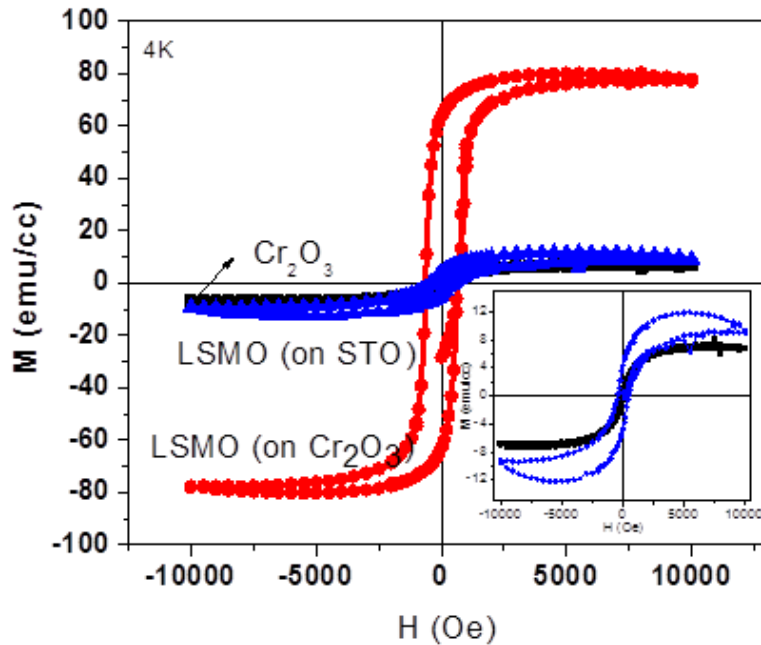


Figure 6.8: Comparison of all three M-H curves,  $\text{Cr}_2\text{O}_3(55\text{nm})$ ,  $\text{LSMO}(66\text{nm})$  on  $\text{STO}(50\text{nm})/\text{Cr}_2\text{O}_3(55\text{nm})$ , and  $\text{LSMO}(66\text{nm})$  on  $\text{Cr}_2\text{O}_3(55\text{nm})$ . The magnetization is suppressed when a 50nm thin non-magnetic insulating STO layer is inserted between  $\text{LSMO}(66\text{nm})$  and  $\text{Cr}_2\text{O}_3(55\text{nm})$  layers. This clearly shows the role of magnetic exchange interaction at the interface between  $\text{LSMO}(66\text{nm})$  and  $\text{Cr}_2\text{O}_3(55\text{nm})$  layers.

The temperature dependence of exchange bias and coercive field collected for  $\text{LSMO}(66\text{nm})/\text{Cr}_2\text{O}_3(50\text{nm})$  heterostructure is plotted in Figure 6.9 (a,b). Both of them decay exponentially as a function of increase in temperature pointing to the fact that their origin is the same. At the blocking temperature of 50K, there is no exchange bias and coercive field is constant, as expected for LSMO layer consisting of two magnetic phases, similar to the present case.

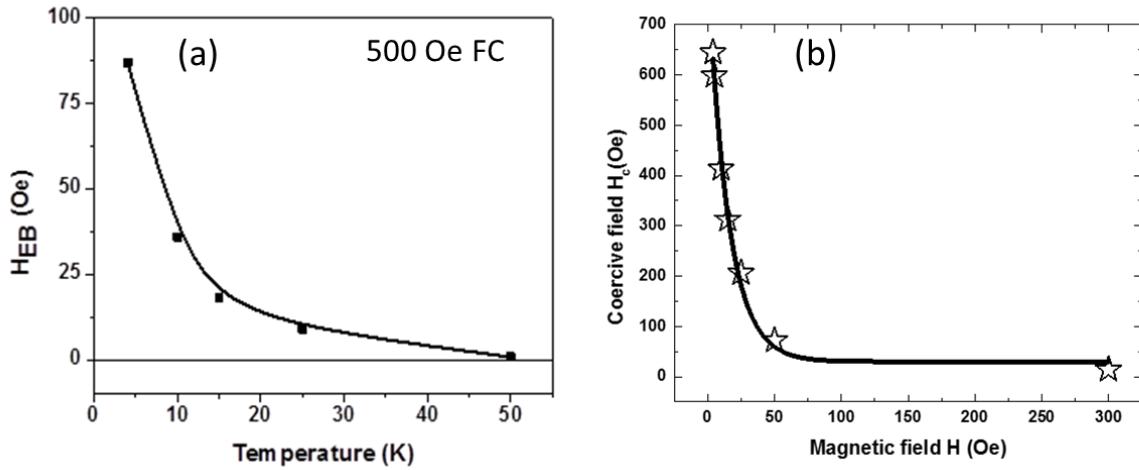


Figure 6.9: The temperature dependences of exchange bias ( $H_{EB}$ ) and coercive field ( $H_c$ ) for LSMO(66nm)/Cr<sub>2</sub>O<sub>3</sub>(55nm). The points show the experimental data and the solid curve guides the eye. The fact that the temperature dependence of  $H_{EB}$  and  $H_c$  shows similar nature, which is an exponential decay, their origin is mostly likely the same, which is the magnetic phase separation in LSMO layer.

## 6.5 Conclusions:

To conclude, we have presented the epitaxial growth of LSMO/Cr<sub>2</sub>O<sub>3</sub> heterostructures on c-YSZ-buffered Si (001) using pulsed laser deposition. The X-ray diffraction ( $2\theta$  and  $\Phi$ ) and TEM characterizations confirm that the films were grown epitaxially. The epitaxial relations can be written as  $[001]Si \parallel [001]c\text{-YSZ} \parallel [0001]Cr_2O_3 \parallel [111] LSMO$  and  $[100]Si \parallel [100]YSZ \parallel [10\bar{1}0]Cr_2O_3$  or  $[11\bar{2}0] Cr_2O_3 \parallel [10\bar{1}] LSMO$ . We have carried out a comprehensive study on this heterostructure as a function of LSMO thickness (66,264,528 nm). Interestingly, as the LSMO thickness increases from 66 to 528 nm, while keeping the Cr<sub>2</sub>O<sub>3</sub> thickness constant at 55 nm, the magnetic moment of the heterostructure increases by more than 2-fold and the magnetic nature has changed from ferromagnetic to super paramagnetic. In addition, LSMO/Cr<sub>2</sub>O<sub>3</sub> showed in-plane exchange

bias with a maximum exchange bias field of 870e. From our experimental data, we believe the change in the magnetic anisotropy as a function of LSMO layer thickness could cause the change in magnetic moment and magnetic nature. The magnetic phase separation in oxygen deficient LSMO layer could lead to in-plane exchange bias as  $\text{Cr}_2\text{O}_3$  is not expected to show in-plane exchange.

## 6.6 References:

1. R. Ramesh and N.A. Spaldin, *Nat. Mater.* **6**, 21 (2007).
2. W. Eerenstein, N.D. Mathur, and J.F. Scott, *Nature* **442**, 759 (2006).
3. M. Bibes and A. Barthélémy, *Nat. Mater.* **7**, 425 (2008).
4. P. Yu, J.-S. Lee, S. Okamoto, M.D. Rossell, M. Huijben, C.-H. Yang, Q. He, J.X. Zhang, S.Y. Yang, M.J. Lee, Q.M. Ramasse, R. Erni, Y.-H. Chu, D.A. Arena, C.-C. Kao, L.W. Martin, and R. Ramesh, *Phys. Rev. Lett.* **105**, 027201 (2010).
5. Y.-H. Chu, L.W. Martin, M.B. Holcomb, M. Gajek, S.-J. Han, Q. He, N. Balke, C.-H. Yang, D. Lee, W. Hu, Q. Zhan, P.-L. Yang, A. Fraile-Rodríguez, A. Scholl, S.X. Wang, and R. Ramesh, *Nat. Mater.* **7**, 478 (2008).
6. S. Valencia, A. Crassous, L. Bocher, V. Garcia, X. Moya, R.O. Cherifi, C. Deranlot, K. Bouzehouane, S. Fusil, A. Zobelli, A. Gloter, N.D. Mathur, A. Gaupp, R. Abrudan, F. Radu, A. Barthélémy, and M. Bibes, *Nat. Mater.* **10**, 753 (2011).
7. D.N. Astrov, *Sov. Phys. JETP* **13**, 729 (1961).
8. D.N. Astrov, L. a Drobyshev, and R.E. Measurements, *Sov. Phys. JETP* **28**, 1123 (1969).
9. A. Iyama and T. Kimura, *Phys. Rev. B* **87**, 180408 (2013).
10. A. Malashevich, S. Coh, I. Souza, and D. Vanderbilt, *Phys. Rev. B* **86**, 094430 (2012).
11. X. He, Y. Wang, N. Wu, A.N. Caruso, E. Vescovo, K.D. Belashchenko, P.A.

Dowben, and C. Binek, *Nat. Mater.* **9**, 579 (2010).

12. P. Borisov, A. Hochstrat, X. Chen, W. Kleemann, and C. Binek, *Phys. Rev. Lett.* **94**, 117203 (2005).

13. D. Halley, N. Najjari, H. Majjad, L. Joly, P. Ohresser, F. Scheurer, C. Ulhaq-Bouillet, S. Berciaud, B. Doudin, and Y. Henry, *Nat. Commun.* **5**, 3167 (2014).

14. D. Halley, N. Najjari, F. Godel, M. Hamieh, B. Doudin, and Y. Henry, *Phys. Rev. B* **91**, 214408 (2015).

15. J.-H. Park, E. Vescovo, H.-J. Kim, C. Kwon, R. Ramesh, and T. Venkatesan, **392**, 794 (1998).

16. T. YOKOTA, S. MURATA, S. KITO, and M. GOMI, *J. Ceram. Soc. Japan* **117**, 639 (2009).

17. S. Punugupati, J. Narayan, and F. Hunte, *Appl. Phys. Lett.* **105**, 132401 (2014).

18. S. Punugupati, J. Narayan, and F. Hunte, *J. Appl. Phys.* **117**, 193907 (2015).

19. H.-J. Kim, D.G. Yoo, and S.-I. Yoo, *Mater. Lett.* **123**, 23 (2014).

20. M. Haghiri-Gosnet, J. Wolfman, B. Mercey, C. Simon, P. Lecoeur, M. Korzenski, M. Hervieu, R. Desfeux, and G. Baldinozzi, *J. Appl. Phys.* **88**, 4257 (2000).

21. J. Narayan and B.C. Larson, *J. Appl. Phys.* **93**, 278 (2003).

22. N.M. Nemes, M. Garcia-Hernandez, Z. Szatmari, T. Feher, F. Simon, C. Visani, V. Pena, C. Miller, J. Garcia-Barriocanal, F. Bruno, Z. Sefrioui, C. Leon, and J. Santamaria, *IEEE Trans. Magn.* **44**, 2926 (2008).

23. J. Hong, Phys. Rev. B **74**, 172408 (2006).
24. E. Dagotto, T. Hotta, and A. Moreo, Phys. Rep. **344**, 1 (2001).
25. A. Urushibara, Y. Moritomo, T. Arima, A. Asamitsu, G. Kido, and Y. Tokura, Phys. Rev. B **51**, 14103 (1995).

# Chapter 7 Summary and Out look

## 7.1 Summary

In this dissertation we have developed buffer layer platforms to grow epitaxial  $\text{Cr}_2\text{O}_3$  and  $\text{La}_{0.7}\text{Sr}_{0.3}\text{MnO}_3$  thin films on Si(001) substrate and also studied their detailed structural and magnetic properties. In case of  $\text{La}_{0.7}\text{Sr}_{0.3}\text{MnO}_3$ , we have also studied transport and magnetotransport properties with the aim of understanding the structure-property relationship.

First, we have integrated epitaxial  $\text{Cr}_2\text{O}_3$  thin films on Si(001) substrate via c-YSZ buffer layer using pulsed laser deposition. The X-ray  $\Phi$ -scan and TEM results confirmed the epitaxial nature of the films. The growth of trigonal  $\text{Cr}_2\text{O}_3(0001)$  on cubic c-YSZ(001) occurs with different in-plane variations. There are four domains of  $\text{Cr}_2\text{O}_3$  with a single [0001] out-of-plane orientation and rotated  $30^\circ$  from each other in the in-plane. Two of the domains are twin equivalent to other two domains. The epitaxial relations can be written as  $(001)[100]\text{Si} \parallel (001)[100]\text{c-YSZ}$  and  $(001)[100]\text{YSZ} \parallel (0001)[10\bar{1}0]\text{Cr}_2\text{O}_3$  (or)  $(0001)[11\bar{2}0]\text{Cr}_2\text{O}_3$  (or)  $(0001)[01\bar{1}0]\text{Cr}_2\text{O}_3$  (or)  $(0001)[\bar{1}2\bar{1}0]\text{Cr}_2\text{O}_3$ . Though the easy axis of antiferromagnetic  $\text{Cr}_2\text{O}_3$  is along [0001], the in-plane magnetic measurements showed ferromagnetic behavior with high saturation magnetization and finite coercivity existing up to 400K. The magnetization was found to be a strong function of thickness. Higher saturation magnetization was found in films of less thickness, which had more residual strain. The oxygen annealing also had strong effect on the strain and magnetization. The thickness dependent magnetization together with oxygen annealing results suggest that the in-plane ferromagnetism in  $\text{Cr}_2\text{O}_3(0001)$  thin films is due to oxygen related defects whose

concentration is controlled by strain present in the films. The out-of-plane measurements performed on the films showed unsaturated component in the M-H loop indicating antiferromagnetic nature of the films. This ferromagnetism in addition to the intrinsic antiferromagnetic and magneto-electric properties of  $\text{Cr}_2\text{O}_3$  opens the door to relevant spintronics applications.

Second, in order to see whether strain can induce magnetic moment in  $\text{Cr}_2\text{O}_3$  thin films of other orientations, we tried to deposit epitaxial thin films on  $\text{Al}_2\text{O}_3(01\bar{1}2)$  substrates. The films were found to be epitaxial as confirmed from the XRD  $\Phi$ -scan and TEM results. The epitaxial relations between the substrate and film were established as  $[01\bar{1}2]\text{Cr}_2\text{O}_3 \parallel [01\bar{1}2]\text{Al}_2\text{O}_3$  (out-of-plane) and  $[\bar{1}\bar{1}20]\text{Cr}_2\text{O}_3 \parallel [\bar{1}\bar{1}20]\text{Al}_2\text{O}_3$  (in-plane). The in-plane SQUID measurements performed (5-400K) on the pristine samples revealed ferromagnetism (FM) with Curie temperature above 400K. The room temperature coercivity and saturation magnetization of the pristine samples were 25 Oe and 0.12 emu/g, respectively. After oxygen annealing, the FM is almost completely suppressed. The FM in the as deposited films is attributed to the strain present in the films as inferred from HR XRD and Raman spectroscopy measurements. The decrease of strain with oxygen annealing indicates that strain is due to point defects such as oxygen vacancies. This study of understanding the origin of FM in  $\text{Cr}_2\text{O}_3$  thin films can be useful to better design the spintronic devices.

Third, we have integrated bi-epitaxial  $\text{La}_{0.7}\text{Sr}_{0.3}\text{MnO}_3(110)$  thin films on  $\text{Si}(001)$  substrate with c-YSZ/STO buffer layers by pulsed laser deposition. We were interested in bi-epitaxial growth to study the effect of domain boundaries on the magneto-transport properties of colossal magnetoresistive  $\text{La}_{0.7}\text{Sr}_{0.3}\text{MnO}_3$ . In addition, for the (110) oriented growth, there

is no polar discontinuity at the STO– $\text{La}_{0.7}\text{Sr}_{0.3}\text{MnO}_3$  interface and hence no dead layer formation occurs. This improves ferromagnetic interaction in the  $\text{La}_{0.7}\text{Sr}_{0.3}\text{MnO}_3$ , making it highly attractive for spintronic applications. The growth conditions for STO were optimized to achieve (110) orientation on c-YSZ(001). The growth of rectangular STO(110) on cubic c-YSZ(001) occurs with two in-plane domain variation also called bi-epitaxial growth, which involves larger misfit ( $> 10\%$ ) and can be explained by the paradigm of domain matching epitaxy. Since  $\text{La}_{0.7}\text{Sr}_{0.3}\text{MnO}_3$  is lattice matched with STO, those films were also grown with a single [110] out-of-plane orientation but with two in-plane domain variants, which was confirmed by XRD and detailed TEM studies. The epitaxial relationship between STO and c-YSZ can be written as  $[110] (001) \text{ c-YSZ} \parallel [\bar{1}\bar{1}\bar{1}] (110) \text{ STO}$  (or)  $[110] (001) \text{ c-YSZ} \parallel [\bar{1}\bar{1}\bar{2}] (110) \text{ STO}$ . The  $\text{La}_{0.7}\text{Sr}_{0.3}\text{MnO}_3$  thin films were ferromagnetic with Curie temperature 324K and showed metal to insulator transition at 285K. The resistivity of the  $\text{La}_{0.7}\text{Sr}_{0.3}\text{MnO}_3$  films is of the order of 10-20  $\text{m}\Omega \text{ cm}$ , comparable to epitaxial thin films. The easy axis of the  $\text{La}_{0.7}\text{Sr}_{0.3}\text{MnO}_3$  thin films is in the (110) plane whereas the hard axis is along [110] out-of-plane. The  $\text{La}_{0.7}\text{Sr}_{0.3}\text{MnO}_3$  thin films showed unique hysteresis loops in magnetoresistance when low magnetic field is applied in both in-plane and out-of-plane directions. The in-plane MR showed cusp-like variation whereas out-of-plane MR reveals a smudged or rounded off nature. The highest MR obtained in this study is -32% at 50K and 50 kOe for  $H_{\parallel}$  configuration whereas the room temperature MR is -4% at 10 kOe and -17% at 50 kOe. The temperature dependent MR showed a peak in low temperature region followed by a monotonic decrease up to 350K. The magnitude of MR can be improved by different post growth techniques. The hysteresis in MR and the controlled domain boundaries in case of bi-

epitaxial  $\text{La}_{0.7}\text{Sr}_{0.3}\text{MnO}_3$  films integrated on Si(001) can offer considerable advantages over the polycrystalline counterparts in terms of improved functionality and reliability.

Finally, the epitaxial  $\text{La}_{0.7}\text{Sr}_{0.3}\text{MnO}_{3-\delta}$ (LSMO)/ $\text{Cr}_2\text{O}_3$  bilayer structure was integrated with Si(001) with the aim of combining a FM/AFM(ME) system with silicon and also study interface magnetic properties. The epitaxial growth of LSMO/ $\text{Cr}_2\text{O}_3$  heterostructures on c-YSZ buffered Si (001) was done using pulsed laser deposition. The X-ray diffraction ( $2\theta$  and  $\Phi$ ) and TEM characterizations confirm that the films were grown epitaxially. The epitaxial relations can be written as  $[001]\text{Si} \parallel [001]\text{c-YSZ} \parallel [0001]\text{Cr}_2\text{O}_3 \parallel [111]\text{LSMO}$  and  $[100]\text{Si} \parallel [100]\text{YSZ} \parallel [10\bar{1}0]\text{Cr}_2\text{O}_3$  or  $[11\bar{2}0]\text{Cr}_2\text{O}_3 \parallel [10\bar{1}]\text{LSMO}$ . We have carried out a comprehensive study on this heterostructure as a function of LSMO thickness (66, 264, 528 nm). Interestingly, as the LSMO thickness increased from 66 to 528 nm, while keeping the  $\text{Cr}_2\text{O}_3$  thickness constant at 55 nm, the magnetization the heterostructure increased by more than 2-fold and also the magnetic nature has changed from ferromagnetic to super paramagnetic. From our experimental data, we believe that the change in the magnetic anisotropy as a function of LSMO layer thickness could cause the change in magnetization and magnetic nature. In addition, LSMO/ $\text{Cr}_2\text{O}_3$  showed in-plane exchange bias with a maximum exchange bias field of 870e. To verify whether the exchange bias effect is arising from the LSMO/ $\text{Cr}_2\text{O}_3$  interface, we have inserted an STO layer in between and found that the system still exhibited exchange bias property. The electrical data showed high resistivity for LSMO thin films since they were grown under  $1 \times 10^{-2}$  Torr oxygen partial pressure. Since oxygen mediation plays important role for the double exchange mechanism between  $\text{Mn}^{+3}$  and  $\text{Mn}^{+4}$  in LSMO, the oxygen deficiency in LSMO resulted in magnetic phase separation (FM and AFM) and lead to in-plane exchange bias in LSMO/ $\text{Cr}_2\text{O}_3$  as  $\text{Cr}_2\text{O}_3$  is not expected

to show in-plane exchange. Though this system is not ideal in terms of expected properties of LSMO, this study can help understanding the effect of processing conditions on the property, which in turn can help better design novel thin film device structures.

## 7.2 Outlook

Based on the present work, some suggestions can be made for the future work. Basing on the experimental result (which is not presented in this dissertation but explored in the process) that  $\text{Cr}_2\text{O}_3$  can be grown epitaxially on  $\text{STO}(111)$ , two schemes are proposed.

- (1) To measure magnetoelectric properties of  $\text{Cr}_2\text{O}_3$  thin films:

$\text{Nb:STO}(111)/\text{Cr}_2\text{O}_3(0001)/\text{TE}$  ; TE refers to top electrode, which could be any metal.

Nb doped STO substrate can serve as bottom electrode.

- (2) To study interface magnetism and exchange bias in LSMO/ $\text{Cr}_2\text{O}_3$  all epitaxial system:

$\text{Al}_2\text{O}_3(0001)/\text{Cr}_2\text{O}_3(0001)/\text{STO}(111)/\text{LSMO}(111)/\text{Cr}_2\text{O}_3(0001)$

In this system, LSMO can be grown without any restriction on the  $\text{O}_2$  partial pressure for deposition. Alternately, it can be grown on  $\text{STO}(111)$  single crystal as well.